https://lib.uliege.be https://matheo.uliege.be

# Master thesis and internship[BR]- Master's thesis : Numerical investigation of a variable tandem outlet guide vane in a low pressure compressor cascade[BR]- Internshi

**Auteur :** Brach, Mathias
**Promoteur(s) :** Hillewaert, Koen
**Faculté :** Faculté des Sciences appliquées
**Diplôme :** Master en ingénieur civil en aérospatiale, à finalité spécialisée en "aerospace engineering"
**Année académique :** 2023-2024
**URI/URL :** http://hdl.handle.net/2268.2/20423

*Avertissement à l'attention des usagers :*

*Tous les documents placés en accès ouvert sur le site le site MatheO sont protégés par le droit d'auteur. Conformément aux principes énoncés par la "Budapest Open Access Initiative"(BOAI, 2002), l'utilisateur du site peut lire, télécharger, copier, transmettre, imprimer, chercher ou faire un lien vers le texte intégral de ces documents, les disséquer pour les indexer, s'en servir de données pour un logiciel, ou s'en servir à toute autre fin légale (ou prévue par la réglementation relative au droit d'auteur). Toute utilisation du document à des fins commerciales est strictement interdite.*

*Par ailleurs, l'utilisateur s'engage à respecter les droits moraux de l'auteur, principalement le droit à l'intégrité de l'oeuvre et le droit de paternité et ce dans toute utilisation que l'utilisateur entreprend. Ainsi, à titre d'exemple, lorsqu'il reproduira un document par extrait ou dans son intégralité, l'utilisateur citera de manière complète les sources telles que mentionnées ci-dessus. Toute utilisation non explicitement autorisée ci-avant (telle que par exemple, la modification du document ou son résumé) nécessite l'autorisation préalable et expresse des auteurs ou de leurs ayants droit.*

# Numerical investigation of a variable tandem outlet guide vane in a low pressure compressor cascade

---

Master thesis presented by
Mathias Brach
in partial fulfillment of the requirements for the degree of Master of Science in Aerospace Engineering

---

**Thesis supervisors**
Professor Koen Hillewaert
*University of Liège*

Doctor Andrea Rocca
*Cenaero*

**Jury members**
Prof. Koen Hillewaert, Dr. Andrea Rocca,
Prof. Vincent Terrapon, Rémy Principivalle

University of Liège - Faculty of Applied Sciences
Liège, Academic year 2023-2024

# Abstract

With a view to improving the performance of axial compressors, the present work investigates the possibilities of adapting the last compressor stage (OGV) to varying compressor operating conditions. In particular, when the inlet flow angle is modified to off-design values, this work proposes solutions that extend the range of incidence operations of the compressor stage. The strategy for boosting performance is to combine a technology already used for OGVs, tandem blades, with the principle of variable stator valves. Numerical simulations using a RANS model with SU2 software were first carried out on the unmodified tandem configuration around a reference flow angle of 50°, considered to be the design angle of the compressor, in order to show the influence of the flow angle on the overall performance of the tandem. It was shown that the nominal tandem configuration is highly dependent on the inlet angle, and that flow separation phenomena on either blade (sometimes both) introduce high losses that limit the OGV's compression capacities. In addition, flow turning was not ideal with this configuration. Indeed, the flow left the stage with a tangential component, whereas it is crucial to have an almost exclusively axial flow velocity. Because of these factors, the incidence range of this nominal configuration was 14.7°.

Following this, further simulations showed very good compressor stage performances when the tandem's front blade was rotated to match the upstream flow. Three strategies for rotating the blade were investigated: rotation around the trailing edge, rotation around the middle point of the central chord and rotation around a point outside the blade. Rotation of the front blade significantly reduced compressor stage losses and, in most cases, prevented the separation phenomena that occurred with the initial configuration, while achieving better compression ratios at each inlet flow angle. The third strategy only investigated high flow angles (above 50°), as geometry changes are limited. Although the first two strategies showed similar results at low inlet flow angles, rotation around the trailing edge performed better than the other two tuning strategies, particularly at high flow angles. Using the latter, the incidence range can be extended to 34.2°, more than double the initial range. The present work highlighted the interest to use such a configuration, especially if operating operations lead to high inlet flow angles.

Finally, simulations also showed that the optimum blade rotation angle was often close to that which minimizes the relative incidence of flow on the front blade leading edge for inlet flow angles around the reference angle (50°). However, for extreme angles (around -15 to +10° beyond this reference angle), the optimum angle of rotation is sometimes relatively different from this minimum angle of relative incidence, as more complex phenomena take on greater importance (gap dimensions, general shape of the tandem, etc.).

**Keywords:** LPC, OGV, RANS, Tandem blades, Variable Stator Vanes

# Acknowledgements

I would like to thank Professor Koen Hillewaert, my thesis supervisor, for his invaluable advice, his patience and his many theoretical insights, without which I would not have finished this work. I would also like to thank him for his useful proofreading work.

In particular, I would like to thank Andrea Rocca, from Cenaero, without whom this work would not have been possible, for his unfailing patience and his countless theoretical and practical suggestions and insights. His crucial help enabled me to find my way around Lucia's tortuous paths, as well as the various software packages used throughout this work. I would also like to thank him for his thorough proof-reading, in search of all possible errors and improvements.

I would also like to thank the whole Cenaero team, Michel Rasquin, Margaux Boxho and many others, for their warm welcome and for helping me to overcome my IT shortcomings, particularly in managing Lucia.

Computational resources have been provided by the Consortium des Équipements de Calcul Intensif (CÉCI), funded by the Fonds de la Recherche Scientifique de Belgique (F.R.S.-FNRS) under Grant No. 2.5020.11 and by the Walloon Region.

The present research benefited from computational resources made available on Lucia, the Tier-1 supercomputer of the Walloon Region, infrastructure funded by the Walloon Region under the grant agreement n°1910247.

I would also like to express my gratitude to my family and my friends from university and Le Moulin for their unconditional support over the past five years, during complicated times, exam sessions and especially during the lockdown.

Last but not least, I would like to thank my mother Anne Minguet, my girlfriend Sophia Donato and Maxime Borbouse for their patient and difficult review in search of the smallest mistakes and layout improvements.

# Contents

# List of Figures

# List of Tables

# Chapter 1

# Introduction

The aeronautics sector is constantly evolving to match low carbon requisites and improve efficiency, reliability and performances, in Belgium as in the rest of the world. In this context, numerous studies are carried out to optimize the performances of the various aircraft components. As one of the general priorities in aeronautics is to save propellant and materials, it is desirable to obtain the lightest possible and most energy-efficient aircraft. Numerous advances have been made in this direction for the majority of aircraft components. Among these, the engine alone has intrinsic characteristics that are the subject of in-depth studies in turbomachinery. In order to reduce its weight, the materials of which it is made and its dimensions must be optimized. However, to remain highly efficient, the engine's components must offer equal or even superior performance, while being smaller in size or fewer in number. Among these components, the axial compressor, composed of a series of successive stages, is an important subject of study. Indeed, a reduction in the number of successive stages while maintaining the necessary compression ratios and low losses would be highly beneficial.

To achieve the engine improvement consideration, the most obvious strategy would be to reduce the number of stages while increasing the pressure ratio across each stage. Unfortunately, such modifications often result in efficiency losses due to fluid mechanics phenomena such as flow separation, choking or surge limit. However, several technologies exist or are under development to overcome these problems. The present work will focus on developing one of these technologies, concentrating on a very specific part of the axial compressor: the outlet guide vane.

These technological developments have been accompanied by the development of the digital simulation sector. With regard to aircraft engines and turbomachinery in general, several specific fields of numerical simulation coexist to optimize engines. The best-known of these are finite element method (FEM) simulations of the strength and performances of the solid materials making up the engine and computational fluid dynamics (CFD) methods, of particular interest to us here. The latter makes it possible to bypass experiments that are sometimes very costly in terms of time, energy and materials, complex and not always accurate, without overcoming the need for crucial experimental or theoretical confirmation. These three aspects always go hand in hand, as they are all important and complementary. CFD aims to numerically solve the guiding equations of fluid mechanics. It is widely used in industry today. With the unbridled growth in computing power, more and more studies are being carried out using CFD, enabling ever larger and more complex simulations. For instance, Figure 1.1 shows the first 360-degrees Large-Eddy Simulation (LES) of a full engine (Project FULLEST, C. Pérez Arroyo with a joint collaboration between Cerfacs, Safran and Akira technologies [1]). However, it is important to keep in mind that CFD, like all numerical methods, is the result of a compromise between accuracy and computational cost. Indeed, the use of numerical tools inevitably leads to the appearance of numerical errors, the study and understanding of which is a crucial subject still under research.

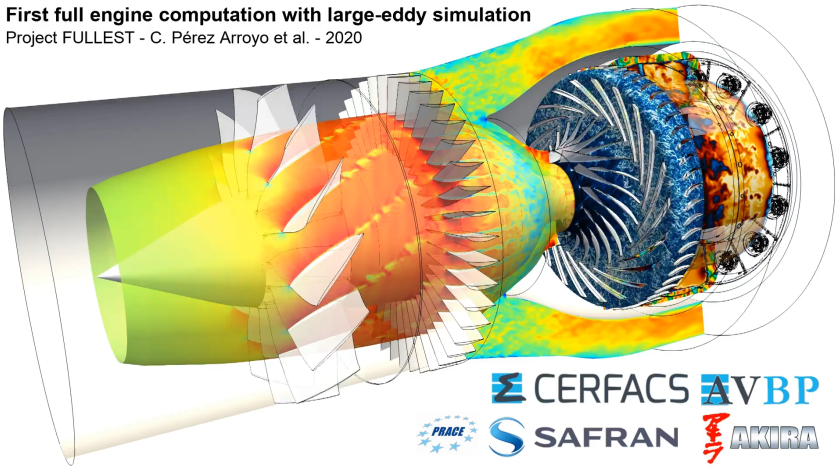

**Figure 1.1:** First full engine computation with Large-Eddy Simulation, C. Pérez Arroyo. Taken from [1].

This work is part of the WINGS (Walloon Innovations for Green Skies) project [2], launched in November 2020 and coordinated by Safran Aerobooster. This is a three-year partnership project between 19 companies with the aim of tackling the ecological crisis affecting the aeronautical sector. A budget is made available for R&D forces to actively contribute to the objectives of the European Green Deal and meet the low-carbon targets set out in the Paris Agreements. The three major companies in the Belgian aerospace sector (Safran Aerobooster, Sonaca and Thales Belgium) are working on a series of varied research topics in collaboration with research centers (Cenaero, Von Karman Institute, CRM, etc.) such as aerostructure, propulsion, communication systems, materials and processes, digitalization and digital simulation, and industry 4.0.

## 1.1 Motivations

The outlet guide vane (OGV) of an axial low pressure compressor is the last stage of the compressor first part (when followed by a high pressure compressor), statically fixed to the engine stator, forming a set of stationary blades. Its role, as the name suggests, is to guide the fluid at the compressor outlet to downstream components (in particular the HP compressor). Since a compressor is made up of a series of rotor-stator stages, the flow undergoes a series of reorientations that vary its velocity and angle. When it exits the last rotor stage, the flow has a high tangential velocity. The role of the outlet vane is to straighten the flow, so that it loses the tangential component of its velocity, and thus ensures a stable, purely axial flow downstream, which is necessary for high HP compressor performances. These valves are designed with a specific angle and profile to capture the partially tangential flow at the rotor outlet. However, it is very difficult to determine the exact angle of flow arriving at the vane in advance. What is more, this angle can vary according to engine operating conditions. For example, at start-up, when the engine's rotation speed is lower, the angle of incidence at the OGV inlet will be modified. To ensure a high pressure ratio via high turning, while minimizing losses through the compressor stage, a number of technologies have been developed to maximize the OGV's operating range. This work focuses on the investigation of a hybrid configuration combining two strategies already available in the industry: tandem blades and variable stator vanes. The first allows the boundary layer developing along the blade to be separated into two boundary layers, the sum of which presents lower losses. The second, mainly used in other compressor stages, enables the blade to be adjusted to the angle of incidence of the flow. In the end, the idea would be to obtain a variable-geometry tandem OGV to accommodate the flow at the rotor outlet, while guaranteeing a predominantly axial flow at the compressor outlet. Particular attention is directed towards high-incidence flows, as they are characterized by elevated pressure ratios, making them of significant interest in industrial applications.

## 1.2 Methodology

Firstly, the present study will investigate a static tandem configuration of the OGV. This initial configuration has been designed to match a flow with an inlet flow angle of around 50° from the rotor, minimizing the relative angle of incidence between the flow and the leading edge of the blade. Once an in-depth study of this configuration has been carried out to ensure the most accurate model possible, the flow input conditions will be modified. Since the interest here is in finding a configuration that increases the operating range of the angle of incidence, only the inlet flow will be modified, while maintaining a Mach number of 0.6 at the entrance to the domain. Having modeled and analyzed how the OGV behaves at different flow angles, and understood its limitations, the second part of the study will investigate the combination of the tandem configuration with a variable front blade. By means of several strategies for adjusting this blade by rotation, the aim will be to see whether or not it is possible to improve OGV performances by sweeping a range of flow angles, and, if so, for what reasons. Finally, these strategies will be compared with each other to determine their respective strengths and limitations, with a view to obtaining an ideal configuration which, via a dynamic accommodation system, would enable the stage geometry to be adjusted according to engine operating conditions in real time. The guidelines will be providing a high pressure ratio, while limiting flow losses and guaranteeing a flow outlet angle close to zero.

## Chapter 2

# Turbomachinery theory

In many cases, aircraft engines include turbomachinery, *i.e.* a combination of compressor, heat exchanger (combustion chambers) and turbine stages. The fundamental principle involves increasing the pressure of a fluid, applying heat to it, and subsequently recovering a portion of this energy to drive the compressor, with the remainder being used to generate the thrust required by the aircraft. Therefore, the purpose of the compressor is to compress incoming air through a succession of stator and rotor pairs known as stages. To enable high mass flow rates, most compressors are of the axial type, although radial compressors are also available. A cut through a typical aircraft turbofan engine is shown in Figure 2.1.

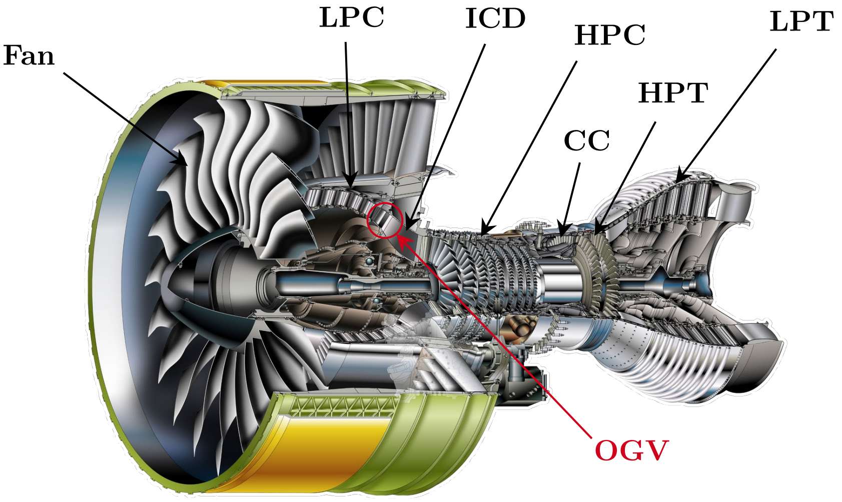

**Figure 2.1:** Cross-section of a typical aircraft turbofan (twoo spool GP 7000 Pratt & Whitney), taken from [3].

Most commercial aircraft use turbofan engines. In these large engines, a large proportion of the incoming air only passes through the fan, the first element on the diagram. Compression of this air by the fan provides most of the thrust generated by the engine and required by the aircraft. To drive the fan, the rest of the air passes through a succession of components: the low-pressure (LPC) and high-pressure (HPC) compressors, the combustion chamber (CC) and then the high-pressure (HPT) and low-pressure (LPT) turbines. Fan speed is limited by shock effects at the tip of the blade, so very high rotation speeds are not possible. However, to increase compressor performances, higher speeds are required the more the flow is compressed. To overcome this problem, the compressor and turbine are divided into two sub-components, connected to different rotating shafts, the fan being connected to the LPC and LPT. To limit problems at the blade tip, the radius of the HPC is smaller than that of the LPC. In this way, an area of the engine called the intermediate compressor duct (ICD) guides the flow to the HPC inlet vane. The OGV (in red on the diagram) of the low-pressure compressor is thus located just at the ICD inlet, or equivalently at the LPC outlet. As explained above, its role in rectifying and stabilizing the flow is crucial to the performance of the HPC, and therefore of the engine as a whole. Because of its particular location, the OGV is a complex element to set up, and for this reason, the adjustment systems discussed below must try to remain relatively simple to implement. As this work focuses on the axial compressor part, the following diagrams and equations will be adapted to this component.

## 2.1 Compressor theory

Axial compressors are distinguished by their axial flow path, where the fluid flows parallel to the axis of rotation. They are often made of several stages alternating stator and rotors blades through which the fluid is progressively compressed. Most of the time, the fluid is air. The main feature is to increase pressure while maintaining a relatively constant mass flow rate and conserving total energy of the flow. Axial compressors are generally composed of the following elements:

1. Rotor: The rotor consists of a series of airfoil-designed blades mounted on a rotating shaft.
2. Stator: The stator also consists of airfoil-designed blades mounted in alternance with rotor stages.
   Those two components are used to change flow direction and convert kinetic energy into pressure.
3. Inlet guide vanes: Located at the compressor inlet, these vanes guide the incoming flow into the first rotor stages at the desired angle.
4. Outlet guide vanes: Highly loaded vanes located at the compressor outlet, designed to impart most of the kinetic energy of the flow to static pressure by slowing down the airflow and guiding it to the next engine stage with the desired angle, often needed close to zero with regard to the axial direction.

The basic operating principle of an axial compressor is the air acceleration due to the rotor blades, increasing its velocity and thus its kinetic energy. This kinetic energy is then converted into pressure by passing through the stator stages where the flow is deviated. This process is repeated across multiple stages, with each stage adding to the overall pressure rise.

### 2.1.1 Main design considerations

Axial compressor performances depend on multiple factors: blade geometry, stage configuration, materials used and aerodynamic considerations. Blade geometry includes several parameters such as blade profile, blade twist or blade aspect ratio. Those parameters significantly impact efficiency and are carefully designed to maximize energy transfer and minimize losses across varying flow conditions. The number of compressor stages is chosen to reach the desired flow overall pressure ratio because single stage pressure ratio are rather small to avoid stall or high loads. Compressor material is also critical since the blades must be able to withstand high temperatures and stresses. Blades are typically made of high-strength materials such as titanium or nickel-based alloys. Sometimes, compressor blades are equipped with internal cooling systems to protect them from the high temperatures generated during compression. Finally, performances also depend on aerodynamic considerations such as tip clearance *i.e.* the gap between the blade tips and the casing. As it can be seen later in this paper, boundary layer plays also an important role in compressor performances. Some compressor are therefore equipped with boundary layer control systems such as airfoil contouring or boundary layer suction.

Generally, velocity profiles in between the blades are represented using velocity triangles, such as represented in Figure 2.2. Here, it can be seen that a change in inlet flow velocity has a high impact on the subsequent stage as the flow relative velocity with regard to the stage considered change significantly, here $\boldsymbol{w}_1'$ and $\boldsymbol{v}_2'$ do not match the blade leading edge angle anymore, which causes losses or even separation. Based on this schematic, we introduce the Euler equation for turbomachinery (here particularized for compressor rotor stage):

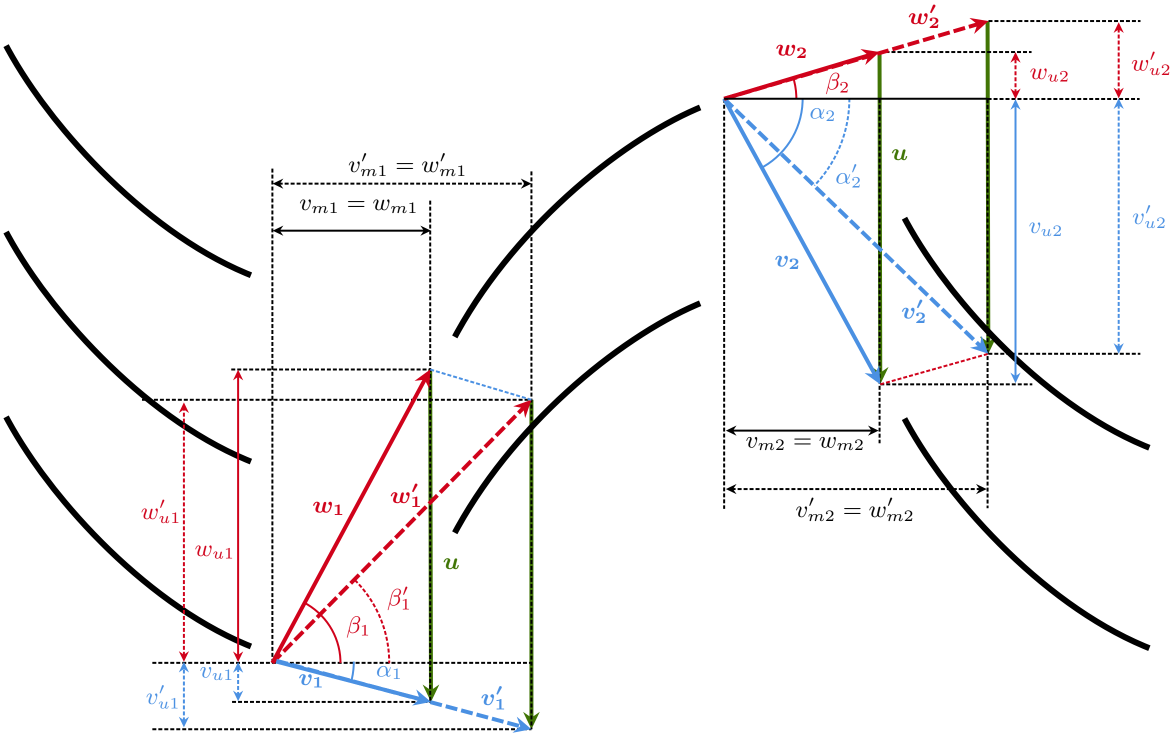

**FIGURE 2.2:** Impact of velocity change on velocity triangles for a compressor stage, reproduced from [4].

$$h_2^\circ - h_1^\circ = u(v_{u2} - v_{u1}), \tag{2.1}$$

assuming no radius change, where $h^\circ = h + \frac{1}{2}v^2$ is the total enthalpy. As this quantity is not conserved over the compressor stage, C. H. Wu [5] suggested a new quantity called *rothalpy* defined by

$$i^\circ = h + \frac{1}{2}w^2 - \frac{1}{2}u^2, \tag{2.2}$$

which is conserved over the stage along streamlines. Moreover, the static enthalpy rise over the stator is given by

$$h_3 - h_2 = \frac{1}{2}(v_2^2 - v_3^2), \tag{2.3}$$

index 3 referring to the stator outlet flow. A commonly accepted result in turbomachinery is that the boundary layer on the suction side of a blade, subject to an adverse pressure gradient, is largely responsible for the pressure rise limitations and flow turning on a compressor stage. Lieblein [6] linked fluid deceleration on the suction side to a dimensionless factor called the *diffusion factor*. This factor also refers to blade loading and relates the peak velocity on the suction surface of the blade to the velocity at the trailing edge. In 2D, diffusion factor reduces to

$$\mathrm{DF} = 1 - \frac{v_2}{v_1} + \frac{\Delta_{12} v_u}{2\sigma v_1} \tag{2.4}$$

where $u_1$ and $u_2$ are the average velocities into and out of the blade row in a frame of reference fixed to the blade, $\Delta v_u$ is the change in tangential velocity and $\sigma$ is the solidity (the ratio between blade chord and blade pitch). A second interesting parameter called *diffusion ratio* (not to be confused with the diffusion factor) is introduced as

$$\mathrm{DR} = \frac{u_{\max}}{u_2}, \tag{2.5}$$

where $u_{\max}$ refers to the peak velocity on the suction side. There appears to be no compelling reason to favor either the diffusion factor or the diffusion ratio; however, given that the diffusion factor is more commonly used, it will be adopted throughout this work. Lieblein showed that in the region of low losses, the wake thickness and the total pressure losses are mainly related to the diffusion of velocity on the suction side of the blade, therefore the boundary layer on this side and the velocity distribution become the main factors to influence total pressure losses. Low diffusion factors imply lower pressure gradients required for flow turning and thus lower diffusion. Hence, momentum thickness increases with DF and start to rise more steeply from DF = 0.6, as showed in Figure 2.3. Generally, diffusion factor above 0.6 is commonly accepted to indicate blade stall (which will be seen in details in the next section) and typical design values are around 0.45 [8][9]. Lieblein work also allowed to understand more correctly the solidity influence on the flow. He showed that an increase in solidity reduces the diffusion factor and delays the onset of stall on one side, but results in higher total losses on the other. As solidity decreases, losses follow. However, if the diffusion ratio approaches its limit, losses appear and the flow might detach. A compromise must therefore be made between low losses (low solidity) and high stability (high solidity) when designing compressors. Some slight variations of the diffusion factor have been introduced later, without modifying really the results explained before. Moreover, it must be noticed that the influence of the Mach number on diffusion factor is not negligible. Indeed, it seems that, at high Mach number (slightly supersonic), a solidity as high as possible is beneficial to avoid strong shock losses. Beside that, a few methods have been proposed to optimize the solidity choice which would provide low losses and acceptable stability. Since the pitch and chord are already fixed, these methods will not be presented in details here but the main results are the following: the higher the solidity, the lower the deviation and the better the guidance, but on the other hand, the higher the solidity, the higher the losses (and the lower the efficiency) [10].

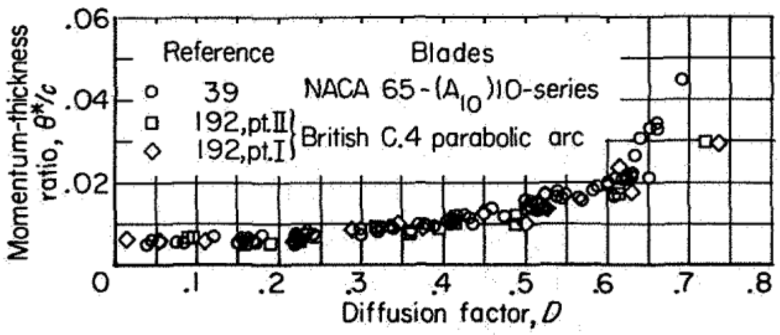

**FIGURE 2.3:** Wake momentum thickness versus overall diffusion factor for NACA-65 and C4 airfoils at minimum loss incidence, taken from [7].

Two important dimensional parameters are generally introduced in turbomachinery to characterize the performance of a compressor stage: the *flow* and *work coefficients*, respectively given by

$$\phi = \frac{v_{a1}}{u}, \qquad \psi = \frac{\Delta_{12} v_u}{u}. \tag{2.6}$$

In the scope of this work, the rotor velocity is not given explicitly, so these parameters will not be used as they are. However, since the incidence angle varies from low values to higher ones, it could be considered as a decrease of flow coefficient. Finally, a last parameter, called the *degree of reaction*, is introduced, enabling us to fully characterize the velocity triangle along with the work and flow coefficients. It is given by

$$R = \frac{h_1 - h_2}{h_1^\circ - h_3^\circ} \tag{2.7}$$

and represents the proportion of static enthalpy rise over the rotor to the total enthalpy rise over the entire stage [4]. At subsonic speed, the only mechanism to increase flow pressure is flow deviation. In supersonic speed, however, this can also be achieved by shock velocity reduction. The first mechanism is therefore the most important one in view to transfer work from the rotor to the flow but, since the velocity $u$ increases with the blade radii, the second mechanism becomes more important in the upper part of the blade.

To characterize the operating range of a compressor, operating maps are used, as shown in Figure 2.4. These give the pressure ratio and efficiency of a compressor as a function of mass flow and motor rotation speed. The line on the left represents the *surge limit*. Beyond this limit, the compressor experiences unstable conditions and is subject to stall. Note also that, as speed increases, the difference in mass flow rate between the surge limit on the left and stall on the right decreases. Indeed, axial compressors can work under variable conditions but the operating range decreases as the Mach number increases. At high Mach number, the difference between mass flow for choke and surge is reduced. Surge occurs at low mass flow when the fluid can no longer stick to blade surface. This will be discussed further in next sections.

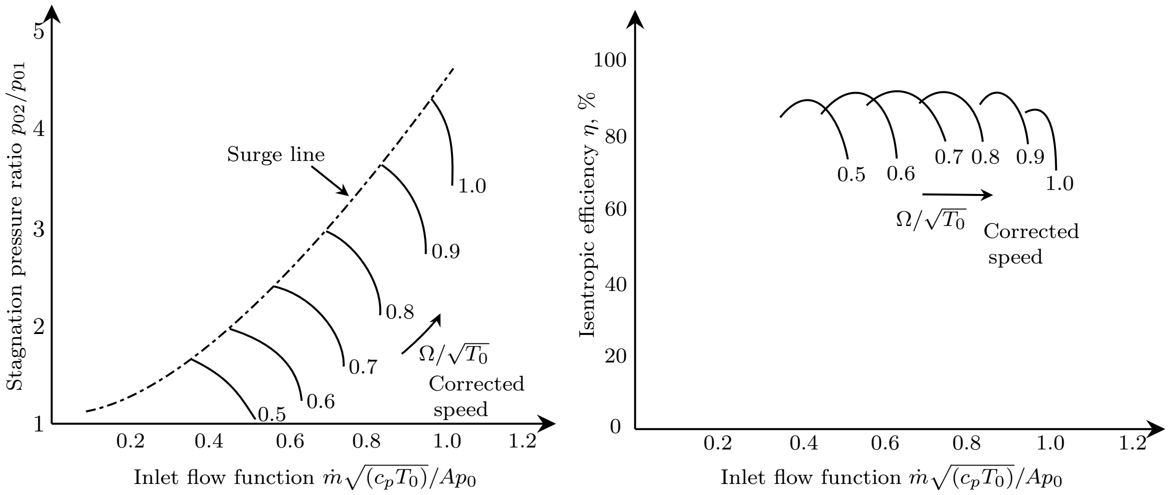

**FIGURE 2.4:** Compressor characteristic maps, adapted from [8] and [4].

### Design parameters

A good practice in turbomachinery is to express the isentropic Mach number along the blade, derived from the pressure distribution, which represents the velocity distribution outside of the boundary layer. Isentropic Mach number is defined as

$$M_{\text{is}} = \sqrt{\frac{2}{\gamma - 1}\left[\left(\frac{p_{0,\text{in}}}{p}\right)^{\frac{\gamma-1}{\gamma}} - 1\right]}, \tag{2.8}$$

where $p$ is the static pressure measured on the blade. The pressure coefficient

$$\pi = \frac{p}{p_{\text{in}}} \tag{2.9}$$

provides an estimation of the efficiency of the compressor stage. Similarly, the loss coefficient is used to characterize the inefficiency of the stage. It measures the drop in total pressure over the entire stage and is given by

$$\omega = \frac{p_{0,\text{in}} - p_0}{p_{0,\text{in}} - p_{\text{in}}}. \tag{2.10}$$

The goal of the compressor stage is to achieve the highest pressure rise and therefore to maximize $\pi$ and minimize the pressure loss $\omega$. Generally, the higher $\pi$, the lower the $\omega$, so the compressor tandem stage is more efficient, all other conditions remaining unchanged. Note that for incompressible or low Mach number flows, the denominator $p_{01} - p_1$ rewrites as $\frac{1}{2}\rho v_1^2$. Finally, two widely industrial parameters to characterize the stage efficiency are the lift and drag coefficients, defined as follows

$$C_{\text{L}} = \frac{L}{\frac{1}{2}\rho v_m^2 c}, \qquad C_{\text{D}} = \frac{D}{\frac{1}{2}\rho v_m^2 c}, \tag{2.11}$$

where $v_m$ is defined as the mean velocity by

$$v_m = v_a \sec \alpha_m, \tag{2.12}$$

$$\tan \alpha_m = \frac{1}{2}(\tan \alpha_1 + \tan \alpha_2). \tag{2.13}$$

Following N. A. Cumpsty [8], it is possible to express these coefficients in terms of velocity angles as

$$C_{\text{D}} = \frac{\omega}{\sigma}\frac{\cos^3 \alpha_m}{\cos^2 \alpha_1}, \tag{2.14}$$

$$C_{\text{L}} = \frac{2}{\sigma}[\tan \alpha_1 - \tan \alpha_2] \cos \alpha_m - C_{\text{D}} \tan \alpha_m. \tag{2.15}$$

For every design and performance parameter, the chord $c$ is considered to be the axial dimension of the tandem $c_{\text{ax}}$ (see Figure 2.8), except for $\text{DF}_i$ where the specific blade chord is used.

### Incidence operating range

The operating range of an axial compressor depends on the flow incidence angle, the blade geometry and the inlet Mach number. In the present study, the inlet Mach number and the blade shapes being fixed, only the incidence angle influence will be discussed in depth in parallel with the modification of the tandem configuration. By definition, the operating range of the compressor is the range of flow incidence angle for which the losses are less than the double of the minimum loss. The reference incidence angle will also be defined as the angle situated in the middle of the incidence range. Figure 2.5 represents the incidence range and the reference inlet flow angle.

## 2.2 Compressor stall and surge limit

In compressors, reducing the mass flow rate increases the pressure rise. However, beyond a certain point where the pressure rise is maximal, a further reduction in mass flow leads to lower pressure rise and change in flow behavior and the compressor enters into either a stall or a surge. Although there has been some confusion between these two phenomena, they do not refer to the same thing. Stall characterizes machine instabilities, linked to local phenomena and dependent on the compressor's intrinsic geometry. It generally affects only one or more

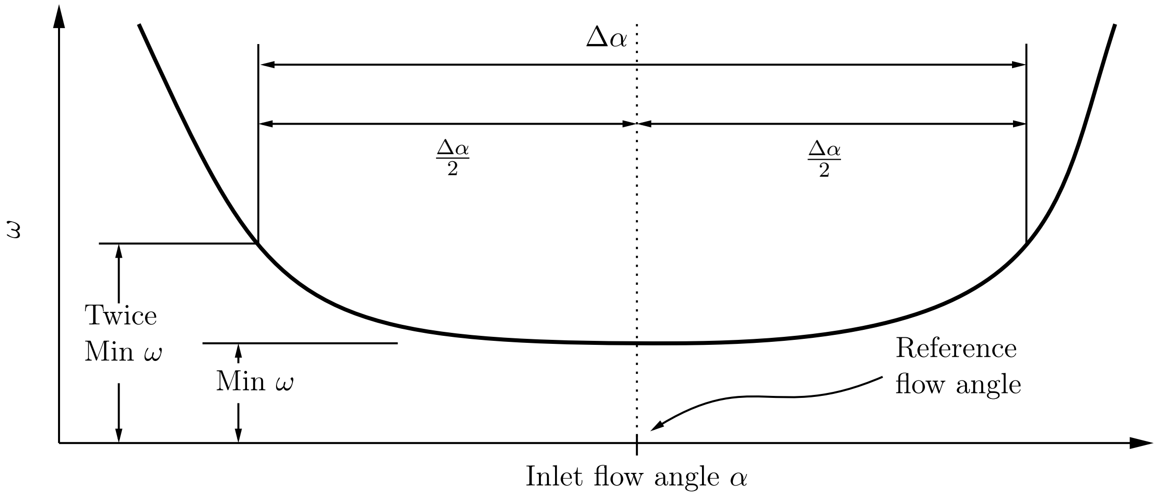

**FIGURE 2.5:** Operating range and reference inlet flow angle, adapted from [8].

blades at a time, creating a loss of lift on the blade. This is generally linked to flow separation on one or more blades, due to an excessively high angle of incidence. In this case, only part of the flow is modified, rather than the whole compressor. Although this leads to losses and sometimes vibrations, the compressor can continue to operate. Stall can also occur as a result of flow distortion at the compressor inlet. There are a number of solutions to this problem, such as variable stator vanes, which will be presented later, or bleeding vanes. Conversely, surge refers to more severe conditions where a complete flow breakdown occurs, leading to a potential reverse flow. This can lead to violent oscillations, loud noises and relatively serious mechanical problems. It is characterized by a significant drop in compressor outlet pressure, affecting compressor efficiency. Surge occurs when the compressor is operating beyond its stable operating range, at low mass flow rates and high compression ratios, or during rapid changes in throttle settings. To remedy the situation, compressor characteristic maps (see Figure 2.4) are used to provide a surge safety margin, or inlet guide vane to stabilize the flow. In aircraft engines, the compressor is followed by the combustion chamber, so if overheating conditions occur, this can lead to a reverse flow of combustion gases, which can be very dangerous since the compressor blades are not designed to withstand such high temperatures.

### 2.2.1 Stall

The stall is a phenomenon whereby the flow detaches from the blade due to adverse pressure gradients, creating a more or less wide zone of separation that generates a low-flow region downstream of the blades. This phenomenon leads to loss and blade stress increases. Stall can occur as a result of various mechanisms, and can be of several types depending on how it is distributed and how it evolves in the compressor. First of all, let's take a look at the mechanisms that cause a blade to stall.

#### Stall mechanisms

There are several reasons why one or more blades may stall. Firstly, classic stall occurs when the thick boundary layer on the suction side of the blade separates due to excessively high incidence or an insufficient mass flow rate. This can happen at any point on the blade, but is more likely to occur on its upper part, where the flow coefficient is lower. The appearance of this kind of stall is linked to the diffusion factor, defined previously. It is commonly admitted that, when the diffusion factor exceeds a typical value of 0.6, the blade is more likely to suffer from stall.

Stall may also occur due to nonuniform inlet flow conditions, which is referred as flow distortion. The reasons of such inlet distortion may be cross-wind conditions. Indeed, if the flow entering the compressor is not uniform, the difference in flow pressure (static or total), flow temperature or velocity may lead to regions of stall in the compressor annulus, which are called *spoiled sector*. Reid [11] showed that the level of loss due to inlet distortion spoiled sector angle increases until 90°, after which performances do not decrease any further. It also seems that several small regions lead to less severe damages on compressor stability than one large region of equivalent area.

An other type of stall can occur in the area close to the casing/hub called endwall stall. The main source of endwall losses comes from secondary flows *i.e.* regions where the flow behaves in an unwanted way from a perfect compressor point of view. According to Sitaram et al. [12], the endwall boundary layer interaction with the mainstream produces complex flow and lead to important losses. Flow interaction with the near-wall region can sometimes generate vortices whose interactions with the flow boundary layer on the blade suction side can lead to stall [13][14].

In addition, in turbomachinery, spaces between the rotating and stationary parts of the compressor are necessary to avoid physical contact and mechanical damages of the structure. These spaces can not be as thin as wanted since the blades may be subject to elongation due to centrifugal effect. They are known as *tip clearance*, and are also a source of potential stall[15][16]. Indeed, given the relatively large pressure difference between the pressure side and the suction side, part of the flow can potentially pass through this gap and interact with the boundary layer, once again creating stall conditions. This effect is known as *tip leakage*. Moreover, the flow part that goes through the clearance is undeflected and therefore is not available for doing work. Both effects directly depend on the thickness of the tip clearance. There are a number of strategies for solving this problem, such as casing treatments to try and delay stall.

### Stall types

There are multiple kinds of stall: rotating or propagating stall, individual blade stall and stall flutter [7]. Although the first one is by far the most prevalent type of stall, individual blade stall is particularly important in the scope of this work. These phenomena will be briefly discussed in this section.

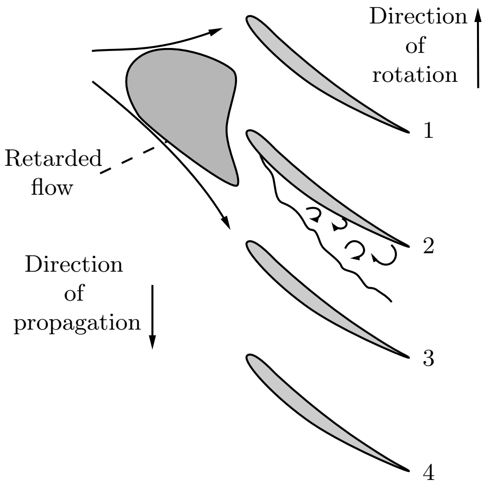

**FIGURE 2.6:** Propagating stall in cascade, adapted from [7].

The first stall mechanism is called *propagating stall* and characterizes the propagation of stall zones in a rotating direction. This phenomenon is illustrated in Figure 2.6. Propagation stall is often caused by tip leakage stall mechanism. When a single blade suffers from stall, say blade two on the schematic, due to an unknown flow perturbation, the airflow no longer sticks to its surface on suction side and the mass flow rate is no longer preserved. Indeed, the incoming flow "sees" a deformed blade shape that restrains the flow to a thinner region. Therefore, the incoming flow is deviated, this is called the *retarded flow* region [7]. This retarded flow region deviates the incoming airflow towards the adjacent blades, increasing the angle of attack on blade three and decreasing it on blade two. Therefore, the third blade is more likely to reach stall conditions and so on. Thus, the stall propagates downward relative to the blade rotation, stalling the blade below and unstalling the one above. However, the stall zone may include several blades. As the stall propagation speed is lower than absolute rotor rotation speed, the stall seems to move in the rotor rotation direction from an absolute frame of reference. Moreover, in multistage compressors, the stall zones appear to extend axially through the compressor [7]. It has been showed that deteriorating operating conditions of axial compressors could be directly linked to the occurrence of rotating stall, leading to either smooth performances decrease or abrupt discontinuous drop of performances depending on the kind of rotating stall behavior (see [7]). For a multistage compressor, the overall pressure coefficient may drop up to 50 percent. This limitation have to be taken into account to determine the operating range of the compressor. The stall pattern typically comprises one or more stall zones, with the number of these zones increasing as the flow coefficient decreases

The second blade mechanism is called *individual blade stall* and is characterized by the development of severe separated-flow zones or zones of low-flow in the wake of each blade. In this case, all the blades around the compressor annulus stall simultaneously, without the need of stall propagation mechanism such as rotating stall. In fact, it appears that individual blade stall is an exception case of propagating stall.

Finally, the last stall mechanism is called *stall flutter* and refers to a self-excited blade oscillation. It should be distinguished from classical flutter which occurs at high flow velocities when a particular velocity couples to the blade design characteristic to induce vibration. Flutter stall is the mechanism by which the flow can transfer energy to the blades and produce oscillations at high blade angle of attack. It is an aeroelastic effect which is beyond the scope of this work.

It is very important to note that, in this work, only one blade is studied. Thus, the potential stall phenomena that would characterize it could only be extended to the whole compressor in the form of individual blade stall, under the assumption that each blade stalls simultaneously. However, this assumption does not take into account the mechanisms of stall progression. As a result, the characteristics and performances to be discussed below are based on an assumption that allows for greater resistance to stall phenomena than it is actually the case and this must be kept in mind for all further analysis.

## 2.3 Tandem Blades

As briefly mentioned earlier, a general objective in turbomachinery has been to achieve improved efficiency with reduced weight in modern compressor designs [17]. Therefore, the obvious solution would be to reduce the number of compressor stages while increasing the load on each stage. However, such high loads are more likely to stall because the flow-turning and the work done by the blade has to be important. Indeed, more work per blade induces greater suction-surface velocity deceleration, which produces more rapid growth of boundary layer and this creates unique flow reverse pressure gradient on the blade suction surface or endwalls (3D effects presented previously). Hence, in recent years, different methods have been studied to overcome this problem such as tandem blades, vortex generator and splitter blades [18]. However, among all the different solutions, tandem blades have the advantage of being a passive method which induces low losses and leads to high turning-flows. Figure 2.7 presents a general tandem blades geometry.

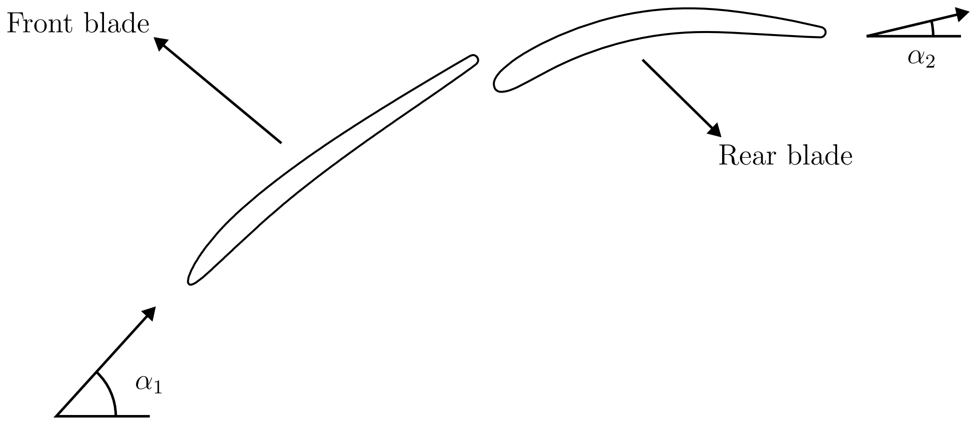

**FIGURE 2.7:** General representation of tandem blades.

The tandem blades geometry allows the load to be distributed on two blades and a fresh boundary layer to begin on the second blade thanks to the gap. Geometric parameters such as camber, chord or orientation of the blades with respect to each other can be modified depending on the application. However, this advantage may become a drawback as there is a wide range of possible configurations possible. Previous studies showed that tandem blades enable wider range of angle of attack while keeping reasonable losses [19].

The 3D effects, ignored here, are yet quiet important, especially near the hub and the casing. The losses in these locations are rather severe. In the center of the blade, the effects of the side walls are negligible.
The 3D effects seem to depend on the local diffusion factor, defined by [20]

$$\mathrm{DF}_i = 1 - \frac{\cos\alpha_{i1}}{\cos\alpha_{i2}} + \frac{\cos\alpha_{i1}}{2\sigma_i}\left(\tan\alpha_{i1} - \tan\alpha_{i2}\right), \tag{2.16}$$

where $\sigma$ is the solidity factor $\sigma = c_i/s$. This is nothing but a simplification of the formula seen previously for the general diffusion factor (see (2.4)). It gives a quantitative measure of aerodynamic limits, especially on the diffusion of suction surface. The experiences showed that tandem blades were beneficial only at large overall loading, DF $> 0.62$ [21]. To differentiate the work of the first and the second blade, a new parameter is introduced, called *load split*. The load split represents the proportion of load distributed on each blade. It is given by

$$\mathrm{LS} = \frac{\mathrm{DF}_1}{\mathrm{DF}_1 + \mathrm{DF}_2}, \tag{2.17}$$

where $\mathrm{DF}_1$ refers to the front blade and $\mathrm{DF}_2$ to the rear one. Hence, a load split below 0.5 indicates that the first blade produces more work than the second and conversely. From previous studies, a few points stand out [18]:

- Equal load distribution on FB and RB is more beneficial;
- The pitch must be rather high;
- The axial overlap AO should be as low as possible;
- Tandem blades are better than a single blade for high airflow turning ($\Delta\alpha > 45°$);
- Interactions between front and rear blade have a high relevance.

### 2.3.1 Specific design parameters

All the geometrical parameters are represented in Figure 2.8. The relative incidence angle is the angle between the flow and the first blade,

$$i = \alpha_{11} - \kappa_{11}. \tag{2.18}$$

The axial overlap is a measure of the gap between the two blades. It expresses as

$$\mathrm{AO} = \frac{\Delta x}{c_{\mathrm{ax}}} \tag{2.19}$$

where $c_{\mathrm{ax}}$ is the length of the stage, measured from the leading edge of the front blade to the trailing edge of the rear blade. Finally, the percent pitch is defined by

$$\mathrm{PP} = \frac{t}{s}. \tag{2.20}$$

Table 2.1 gives a overview of the order of magnitude of the geometrical parameters of the baseline configuration used. Length are given with respect to a unitary tandem chord $c_{\mathrm{ax}} = 1$. Other values are given as intervals framing the actual value.

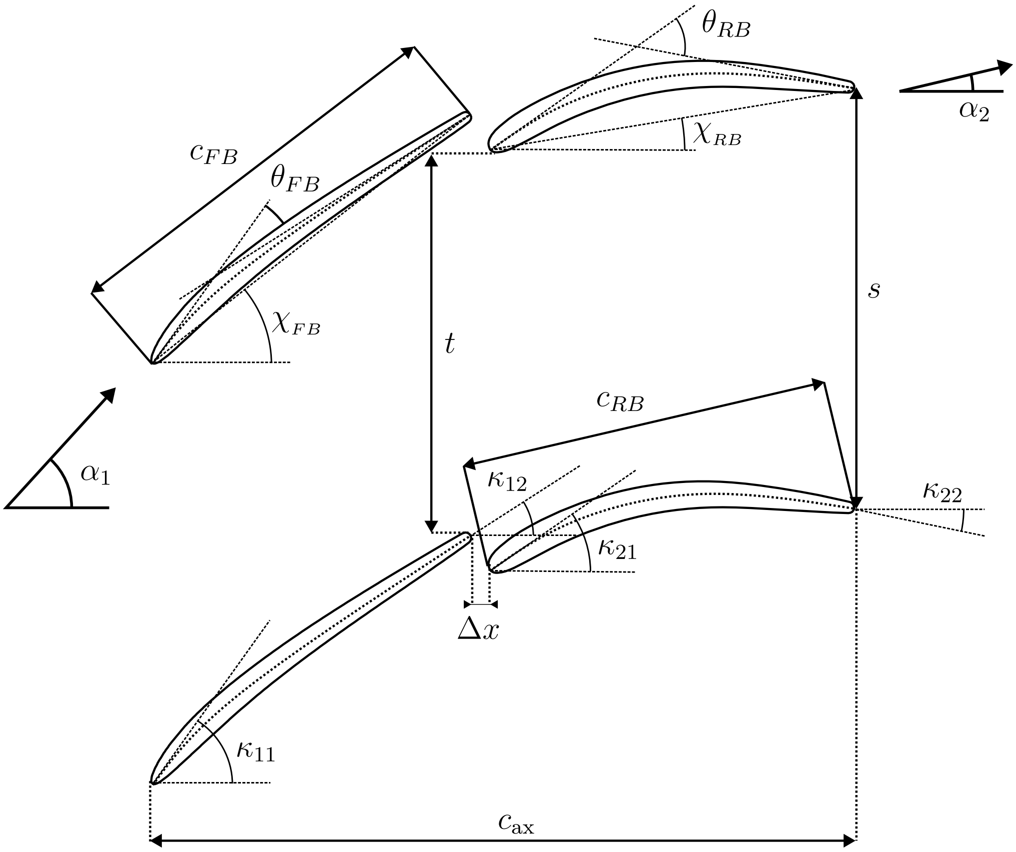

**Figure 2.8:** Geometrical parameters of the tandem blades configuration.

## 2.4 Variable Stator Vanes

Gas axial compressor engines include the use of multiple stator and rotor stages, following each other alternatively. The stator vanes serve to guide the flow towards the next rotor stage so that it takes the appropriate flow angle and speed. In order to improve this under off-design

**Table 2.1:** Geometric parameters of the initial tandem configuration, with respect to $c_{\text{ax}} = 1$. Other values are given as intervals framing the actual value.

| **General** | | **Front blade** | | **Rear blade** | |
|---|---|---|---|---|---|
| Name | Value | Name | Value | Name | Value |
| $c_{\text{ax}}$ | 1 | $c_{FB}$ | $0.53 \cdot c_{\text{ax}}$ | $c_{RB}$ | $0.49 \cdot c_{\text{ax}}$ |
| $t$ | $0.49 \cdot c_{\text{ax}}$ | $\chi_{FB}$ | 35-40° | $\chi_{RB}$ | 5-10° |
| $s$ | $0.54 \cdot c_{\text{ax}}$ | $\kappa_{11}$ | 50-55° | $\kappa_{21}$ | 35-40° |
| $\sigma$ | 1.85 | $\kappa_{12}$ | 30-35° | $\kappa_{22}$ | -10- -5° |
| AO | 2.5% | $\theta_{FB}$ | 15-20° | $\theta_{RB}$ | 40-45° |
| PP | 90.5% | | | | |

conditions to avoid entering in unstable working state and eventually to full breakdown of the flow *i.e.* surge conditions, and remain under acceptable performances, stator vanes that are said to be variable stator vanes (VSVs) are often used. This kind of vanes are able to rotate around an axis to adjust better their angle of attack. Indeed, the instabilities in the flow are most of time due to high incidence flow and stalling of stages. The problem at low speed is that front stages suffer from stall while the rear ones may choke. On the other hand, at high speed, the inverse phenomenon happens: front stages operate close to choked conditions and rear stages are likely to stall and cause surge conditions [22]. This bad matches can even lead to structural damages due to flow oscillations. The way to adjust the stator blade angle of attack, which is the angle between the airflow and the leading edge of the stator vane, is therefore an active field of engineering research, including experimental and simulation methods. However, simulation methods allow to determine good stator vanes adjustment scheme in a short time, while saving power and materials. Moreover, nowadays, compressors become more and more complex, making experimental methods very difficult and expensive. VSV are also widely used in marine gas turbine and ground power generation.

VSV can improve stage matching and Figure 2.9 represents a simplified example of its use through velocity triangles. In this example, taken from [4], a change in mass flow rate leads to a change in velocity $\boldsymbol{v_1}$ to $\boldsymbol{v_1'}$ and therefore to their axial components. If the stator angle remains unchanged, the flow angle does not change so that $\alpha_1 = \alpha_1''$. The rotor velocity remaining unchanged, the flow angle seen from the rotor blade point of view $\beta_1$ is modified to $\beta_1''$, inducing a bad matching of flow angle and blade angle. Moreover, the tangential component of the velocity being more important at the inlet ($v_{u1}'' < v_{u1}$) and conversely at the outlet, the work produced by the stage is reduced since the flow is less deviated. In order to correct this, the stator blade angle is modified from $\chi$ to $\chi'$ which allows the flow to reorientate after the stator and therefore the flow seen from the rotor point of view re-matches with the blade so that $\beta_1' = \beta_1$. Moreover, since $v_{u1}' < v_{u1}''$, the flow deviation is more important and therefore so is the work. Stagger angles of each stator blade can be adjusted, modifying the flow incidence angle ($i$) on the rotor blades. Previous studies have indicated that the adjusted blade angle should be decreased progressively further downstream [23].

Roh and Daley [23] and Sun and Elder [22] showed that VSVs were actually beneficial to improve the stages matching and improve compressor performances. Moreover, Yang et al. [24] showed that multistage stator re-stagger optimization could increase efficiency up to 7% and the surge margin to 19%, although the advantages between optimizing the input vane stall angle with the first two stator stages and optimizing the stall angle on all compressor stages are negligible.

The VSV mechanism need to adjust the angle of the stator blades all around the casing circum-

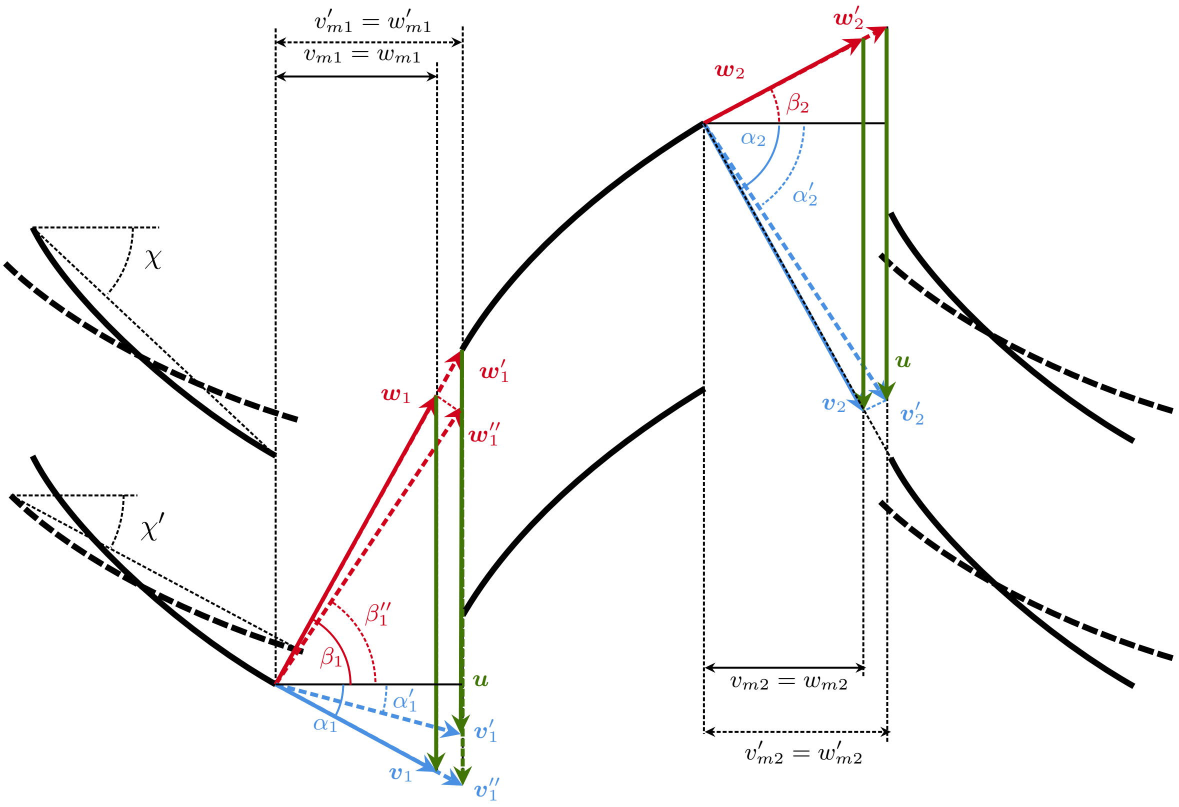

**Figure 2.9:** Adjusting variable stator vane triangles for an increase in mass flow, reproduced from [4]. Values ($\boldsymbol{v'_1}, \alpha'_1, ..$) refers to modified geometry while values ($\boldsymbol{v''_1}, \alpha''_1, ..$) represent the one if the stator angles remain unchanged.

ference at the same time. In order to do that, manufacturer use linkage ring structure and a complete circle of rocker arms. There exist many variants of this system and other adjusting mechanisms, and they are all very complex, nonlinear and time-varying dynamic system [25]. A typical used type of adjustment mechanism is represented in Figure 2.10. They are generally made of metal (for example titanium) or composite materials occasionally [26].

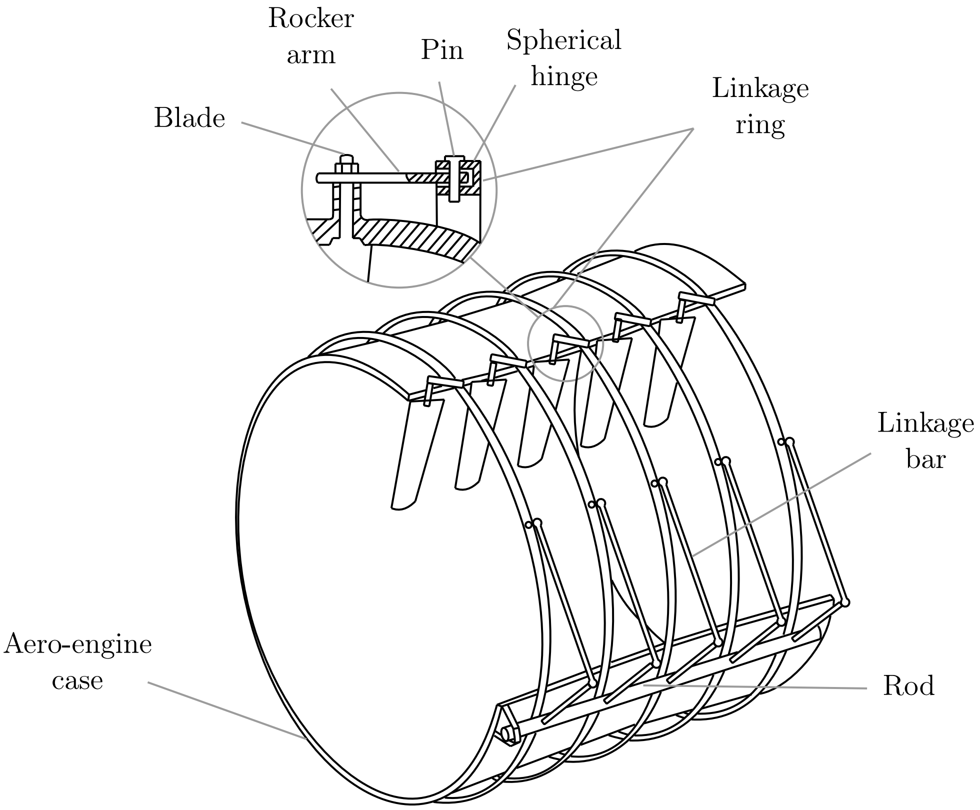

**FIGURE 2.10:** Typical variable stator vanes mechanism, reproduced from [25].

## 2.5 Variable tandem guide vane

Based on the two strategies presented above, a new hybrid configuration will be studied in this work. In order to benefit from the advantages of a turning strategy in addition to a tandem configuration, a geometry comprising two separate vanes, the first of which would be a sort of variable stator vane, appears to be an interesting compromise. In fact, the main effects sought for the outlet vane are high turning with an outlet angle close to zero, so as not to disturb the downstream flow with a radial flow component that could generate unstable or swirling effects. Figure 2.11 shows an example of the application of such a configuration where the flow arriving at the outlet vane has undergone a change in velocity compared with the design conditions due to off-design conditions. For this example, if the mass flow is reduced, the tangential component of the rotor outlet velocity $w'_{m1}$ is reduced. Note that the angle $\beta'_1$ is not necessarily modified, although it is represented as such on the diagram for clarity. Because of this, $v_{u1}$ is increased and becomes $v'_{u1} > v_{u1}$. In the absence of a rotating front blade, blade-induced turning is too weak and relative incidence too high, and the flow may enter in stall conditions, leading to a non-zero $v''_{u2}$ component. As a result, blade work is reduced. When the angle of the front blade is changed from $\chi$ to $\chi'$, the relative incidence is lower in absolute value and there is better matching between the flow and the blade, which eliminates the tangential component of the flow at the outlet and increases work, since $\Delta_{12}v_u$ is greater.

Although this configuration offers significant improvements, it is important to note that such an adjustment system would be complex to implement, given the size of the front blade and the aerodynamic forces involved. Moreover, as suggested above, a tandem configuration is only of interest for high blade loads, *i.e.* potential high loads on the front blade.

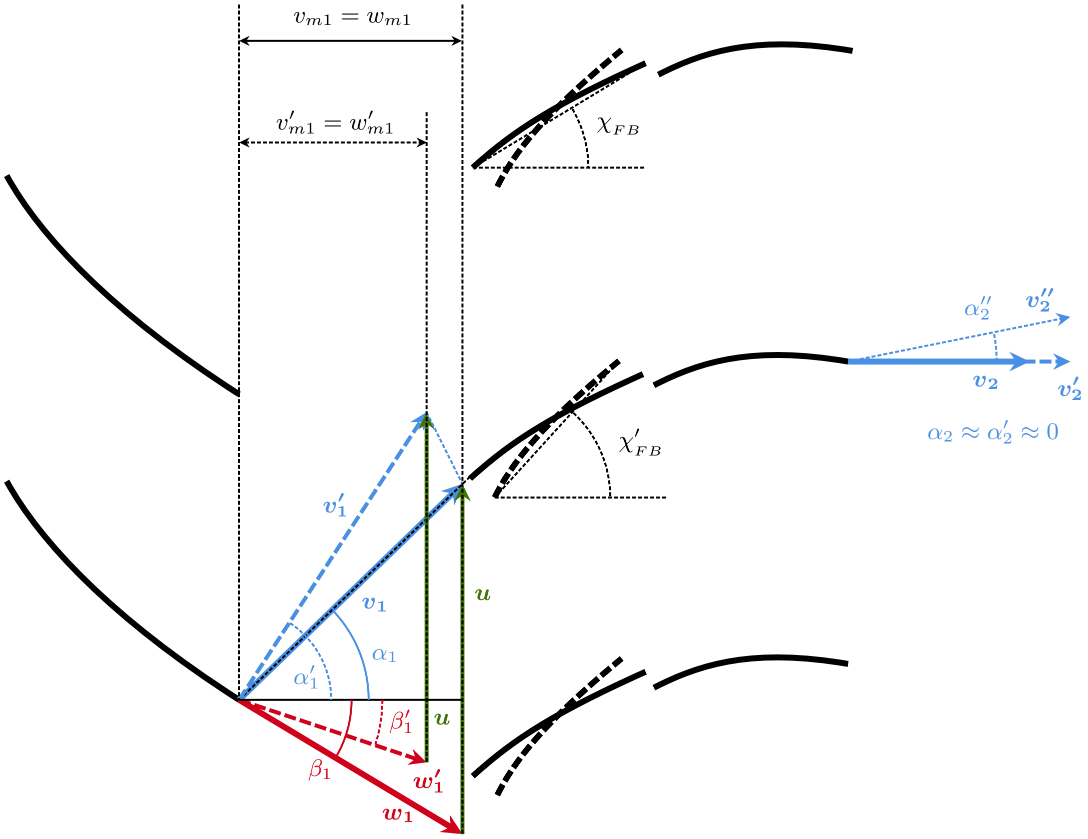

**Figure 2.11:** Adjustment of variable tandem outlet guide vane for an increase of incoming flow angle. Values $\boldsymbol{v''_2}$ and $\alpha''_2$ represent the flow if the front blade angle $\chi_{FB}$ remains unchanged.

# Chapter 3

# Flow physics

The studied flow is subject to turbulence, which is very difficult to model. According to Davidson [27], *"incompressible fluid turbulence is a spatially complex distribution of vorticity which advects itself in a chaotic manner in accordance with*

$$\frac{\mathrm{D}\boldsymbol{\omega}}{\mathrm{D}t} = (\boldsymbol{\omega} \cdot \nabla)\boldsymbol{u} + \nu \nabla^2 \boldsymbol{\omega}. \tag{3.1}$$

*The vorticity field is random in both space and time, and exhibits a wide and continuous distribution of length and time scales."*

## 3.1 RANS model

The idea of this model is to approach the Navier-Stokes equations from a statistical perspective by averaging these equations, decomposing the quantities into their mean value plus a fluctuation. For example, the velocity $u$ becomes

$$\boldsymbol{u}(\boldsymbol{x}, t) = \bar{\boldsymbol{u}}(\boldsymbol{x}) + \boldsymbol{u'}(\boldsymbol{x}, t) \tag{3.2}$$

where $\bar{u}$ is the mean velocity and $u'$ the fluctuation. The Navier-Stokes equation then rewrites as

$$\rho(\bar{\boldsymbol{u}} \cdot \nabla)\bar{u}_i = -\frac{\partial \bar{p}}{\partial x_i} + \frac{\partial}{\partial x_j}\left[\bar{\tau}_{ij} - \rho\overline{u'_i u'_j}\right] \tag{3.3}$$

where $-\rho\overline{u'_i u'_j}$ is the Reynolds stress tensor. This tensor couples the mean flow with turbulence and represents the additional stress experienced by the fluid. However, it primarily characterizes the mean momentum fluxes induced by turbulence. According to (3.3), it is clear that if we want to predict the behavior of the flow, we need to find a way to model these Reynolds stresses. The obvious way would be to directly derive the exact equation for $\overline{u'_i u'_j}$ but it appears that the problem get worse: a further moment $\overline{u'_i u'_j u'_k}$ arises but also a velocity-pressure gradient correlation. And this get worse and worse as we try to derive new exact equations for the new terms. Hence, as the temporal evolution of this tensor is not directly solvable, the RANS equations require a closure model. Paradoxically, while the aim of the statistical description was to simplify the resolution of the Navier-Stokes equations, it actually complicates the resolution process. Indeed, this transition leads from a fully determined problem to an unclosed system of equations. However, the quantities evaluated are now non-random and reproducible as long as we can provide a closure model.

### 3.1.1 Eddy viscosity theory

The first attempt to describe the Reynolds tensor was made by Boussinesq. He proposed a shear/stress relationship of the form

$$\bar{\tau}_{xy} + \tau_{xy}^R = \rho(\nu + \nu_t)\frac{\partial \bar{u}_x}{\partial y} \tag{3.4}$$

where $\nu_t$ is the *eddy viscosity.* This means that the role of turbulence is to virtually add some viscosity to $\nu$. Hence, the problem now is to find what is this eddy viscosity. Prandlt made a proposition based on the kinetic theory of gases where the viscosity is defined as

$$\nu = \frac{1}{3}lV, \tag{3.5}$$

where $l$ is the mean free path of the molecules and $V$ their root mean square velocity. Suggesting a similarity of this process with turbulence, he proposed from a dimensional point of view that the eddy viscosity would be of the form

$$\nu_t = \ell_m V_T, \tag{3.6}$$

where $\ell_m$ is called the mixing length and $V_T$ is a measure of $|\boldsymbol{u}'|$. This of course does not really help to solve the problem as we now need to give the expression of these two new quantities. After few transformations, he came to the following equation, which is called the Prandlt mixing length model,

$$\nu_T = \ell_m^2 \left|\frac{\partial \bar{u}_x}{\partial y}\right|. \tag{3.7}$$

Recal that, as $\overline{u'v'} \approx -\nu_T \partial_y U$, it only depends on the value of $\ell_m$. That is, if we can determine $\ell_m$, say by experiment, then we can find $\tau_{xy}^R$ and thus solve the RANS equations. For free shear layers, $\ell_m$ behaves as $c\delta$, where $\delta$ is the local thickness of the layer, and $c$ is a constant depending on the type of shear layer. In boundary layers, the value of $\ell_m$ near the wall is equals to $\kappa y$ where $\kappa \approx 0.4$ is the Von Karman's constant. This simple model works surprisingly well but still shows some limitations. To improve the model, other eddy viscosity descriptions have been used and two of them are used in this project. The next section describes these two methods.

## 3.2 Turbulence models

In order to close the RANS equations, it has been shown that a model for the Reynolds stress tensor needs to be computed. Two models have been used in the present study: Spalart-Allmaras (SA) and Shear Stress Tensor (SST). These two models are closure models using scalar variables as the mixing length theory discussed in the former section. All the models presented here need empirical constants because the equations used are not directly derived. The models then become methods to correctly use data measured in more simple flows to solve more complex flows.

### 3.2.1 $k-\varepsilon$ model

The $k-\varepsilon$ model is the most general and common model for turbulence. There are several variations of this model but we will focus on the "standard" one developed by Jones and Launder since it is still a basis for a wide range of applications. Furthermore, the popularity of this model can be attributed to the fact that it was the first model employed in computational fluid dynamics [28]. As a reminder, the purpose is to give an expression of the eddy viscosity $\nu_T$. The hypothesis is made that, at high Reynolds, the production rate and the dissipation rate are of the same order of magnitude such that $\varepsilon \approx \mathcal{P}$. Hence, we obtain

$$\nu_T \varepsilon \approx \nu_T \mathcal{P} = \nu_T \left( -\overline{u_i' u_j'} \frac{\partial U}{\partial y} \right) = \left( \overline{u_i' u_j'} \right)^2 \approx 0.09 k^2, \tag{3.8}$$

knowing that $-\overline{u_i' u_j'} = \nu_T \partial_y U$. Experimental observations lead to estimation of the stress-intensity ratio $\overline{u_i' u_j'}/k \approx 0.3$. The equation (3.8) rewrites as

$$\nu_T = C_\mu k^2 \varepsilon, \tag{3.9}$$

where the standard value of $C_\mu$ is 0.09.

The mean flow is now calculated based on the scalar eddy-viscosity and the constitutive relation

$$-\overline{u_i' u_j'} = 2 \nu_T S_{ij} - \frac{2}{3} k \delta_{ij}, \tag{3.10}$$

where $S_{ij}$ is the mean rate-of-strain tensor [28]. This linear stress-strain relation assumes an equilibrium between Reynolds stress and the mean rate of strain. This hypothesis might be incorrect in some particular flows such as turbulent flows strongly anisotropic or subject to rapid irrotational straining but still works surprisingly well for a wide range of applications. The equation (3.9) reduces the whole problem of eddy viscosity modeling to a spatial and time distribution of $k$ and $\varepsilon$. Hence, the closed evolution of $k$ is given by

$$\mathrm{D}_t k = \mathcal{P} - \varepsilon + \partial_j ((\nu + \nu_T / \sigma_k) \partial_j k), \tag{3.11}$$

where $\sigma_k = 1$. Similarly, the evolution of $\varepsilon$ is given by

$$\mathrm{D}_t \varepsilon = \frac{C_{\varepsilon 1} \mathcal{P} - C_{\varepsilon 2} \varepsilon}{T} + \partial_j \left( \left( \nu + \nu_T / \sigma_\varepsilon \right) \partial_j \varepsilon \right), \tag{3.12}$$

where $T = k/\varepsilon$ for dimensional consistency. The standard values of $C_{\varepsilon 1}$, $C_{\varepsilon 2}$ and $\sigma_\varepsilon$ are respectively 1.44, 1.92 and 1.3.

Substituting the equations (3.9), (3.11) and (3.12) into equation (3.3) closes the model as long as boundary conditions can be provided, which is an other problem.

### Boundary conditions and near-wall modifications

Although the boundary conditions of the $k - \varepsilon$ model are quite natural, the near-wall behavior is not. This is problematic as the near-wall region is often important in the flow study. Indeed, in theory, turbulent mixing vanishes in this region, causing great reduction of transport across the boundary layer. The model does not represent this effect which leads to bad predictions of skin-friction and heat transfer. The wall conditions impose

$$k = 0, \qquad \partial_y k = 0, \tag{3.13}$$

$y$ considered as the wall-normal direction. It follows that equation (3.11) reduces as

$$\varepsilon_w = \lim_{y \to 0} \frac{2 \nu k}{y^2}, \tag{3.14}$$

which, in practice can be evaluated at the first computational node. An other issue comes from the correlation time scale $T = k/\varepsilon$ which should not vanish at the wall. Thus, $k - \varepsilon$ requires modification, called *low Reynolds number correction.*

Another method to avoid the wrong prediction of the $k-\varepsilon$ model in the near-wall region is to switch from the $k-\varepsilon$ equations to specific wall equations. These equations are used within the law-of-the-wall region and the $k-\varepsilon$ otherwise. Let $y_p$ be the distance from the wall at which the patching is done. Boundary conditions need to be set at $y_p$ in the logarithmic region while skin friction is obtained from logarithmic drag law applied at $y_p$ [29]. These wall functions are widely used is practice, and many variants exist. However, these equations are sometimes inadequate for highly perturbed flows and the mesh cannot be generated *a priori*, which necessitates to iterate with the simulations to find $y^+$, the non-dimensional wall distance (see subsection 3.3.1).

### 3.2.2 $k-\omega$ model

The equations (3.11) and (3.12) being similar and knowing the time-scale $T = k/\varepsilon$, one might use an equation of the evolution of $T$ instead, combined with the $k$ equation. In fact, this would be exactly equivalent for homogeneous turbulence. In non-homogeneous flows, however, a diffusion term must be added, which differentiates the two methods. Nevertheless, in steady-state, the diffusion term becomes negative, which is mathematically ill-posed and computationally unstable. Therefore, $\omega$, which is just the inverse of $T$ is preferred, as it requires a positive diffusion coefficient. Wilcox [30] defined the $k-\omega$ model by replacing the $\varepsilon$ equation and posing $\omega = \varepsilon/C_\mu k$ so that

$$\mathrm{D}_t k = 2\nu_T|S|^2 - C_\mu k\omega + \partial_j\left(\left(\nu + \frac{\nu_T}{\sigma_k}\right)\partial_j k\right), \tag{3.15}$$

$$\mathrm{D}_t \omega = 2C_{\omega 1}|S|^2 - C_{\omega 2}\omega^2 + \partial_j\left(\left(\nu + \frac{\nu_T}{\sigma_\omega}\right)\partial_j \omega\right), \tag{3.16}$$

$$\nu_T = k/\omega, \tag{3.17}$$

where the standard constants are $C_{\omega 1} = 5/9$, $C_{\omega 2} = 3/40$ and $\sigma_\omega = \sigma_k = 2$ [28]. Near a no-slip surface, the model is dominated by the terms

$$\partial^2_{y^+} k_+ = C_\mu k_+ \omega_+ \qquad \partial^2_{y^+}\omega_+ = C_{\omega 2}\omega_+^2 \tag{3.18}$$

in non-dimensional units, showing that $\omega$ is singular at no-slip boundaries and $k$ does not behaves as $y^2$ anymore [28]. One of the advantages of this model is that it does not need wall functions, or wall dumping near boundaries due to the extra dissipation produced near the walls. Indeed, the dissipation equation of $k$ is given by $\varepsilon$, which equation is given by (3.12) but with an additional term $S_\omega$ in the right-hand side:

$$S_\omega = \frac{2}{T}\left(\nu + \frac{\nu_T}{\sigma_\omega}\right)\left[\frac{|\nabla k|^2}{k} - \frac{\nabla k \cdot \nabla \varepsilon}{\varepsilon}\right]. \tag{3.19}$$

This term is the main difference between the $k-\varepsilon$ and $k-\omega$ models and is a source of dissipation. Although the behavior of the $k-\omega$ model underestimates $k$ and overestimates $\varepsilon$, these errors actually combine to provide a better prediction of $\nu_T$. Nevertheless, the model overpredicts the level of shear stress in adverse pressure-gradient boundary layers and is too sensitive to spurious free-stream conditions. These two drawbacks led Menter [31] to propose a variant of the $k-\omega$ model: the shear-stress transport model.

#### Shear-stress transport (SST) model

The SST model solves the two problems described above by limiting the eddy viscosity in boundary layer region and switching to the $k-\varepsilon$ model in the region out far from the wall.

In order to limit the estimation of shear stress, a bound is imposed on the stress-intensity ratio $a_1 \equiv \overline{u'v'}/k$. Hence, the bound is

$$\nu_T = \min\left[\frac{k}{\omega}, \frac{\sqrt{C_\mu}k}{F_2|2\boldsymbol{\Omega}|}\right]. \tag{3.20}$$

This bound improves prediction of adverse pressure gradient and separated flow. The term $F_2$ is introduced to ensure that the limiter is confined to boundary layer, his value tending to zero in the free stream.

The second modification is to multiply $S_\omega$, which appears in the evolution equation of $\varepsilon$ in the $k-\omega$ model, by $F_1$ which is near unity in inner half of boundary layer and rapidly tends to zero inside the boundary layer. The constants $C_{\varepsilon 1}$ and $C_{\varepsilon 2}$ also change to adapt to this modification.

### 3.2.3 Eddy viscosity transport models - Spalart-Allmaras

The idea of this model was to avoid using two equations to provide the time and spatial evolution of viscosity by using only one. The assumption is firstly made that the effective viscosity $\tilde{\nu}$ satisfies a general transport equation of the type

$$\mathrm{D}_t\tilde{\nu} = \mathcal{P}_\nu - \varepsilon_\nu + \frac{1}{\sigma_\nu}\left[\nabla((\nu+\tilde{\nu})\nabla\tilde{\nu} + c_{b2}|\nabla\tilde{\nu}|^2\right]. \tag{3.21}$$

With one difference, the term multiplied by $c_{b2}$, this equation is similar to those of $\varepsilon$, $\omega$ and $k$, with a right-hand side including production, dissipation and transport terms. The additional term controls the evolution of free-shear layers. The method uses linear distance $d$ which simplifies numerics near the wall instead of $y$. Production is given by

$$\mathcal{P}_\nu = c_{b1}S\tilde{\nu}. \tag{3.22}$$

Finally, the dissipation is given by

$$\varepsilon_\nu = c_{w1}f_w\left(\frac{\tilde{\nu}}{y}\right)^2. \tag{3.23}$$

The constant $c_{b1}$ and $c_{b2}$ are calibrated using spreading and velocity profiles and are respectively 0.1355 and 0.622, while $c_{w1}$ comes from the logarithmic layer solution and $f_w$ from the skin friction of a flat plate and $S$ is chosen to be the magnitude of the mean vorticity [29]. From this, the actual eddy viscosity is defined by

$$\nu_T = \tilde{\nu}f_\nu(\tilde{\nu}/\nu), \tag{3.24}$$

where $f_\nu$ is the transformation function, given by

$$f_\nu(\tilde{\nu}/\nu) = \frac{(\tilde{\nu}/\nu)^3}{(\tilde{\nu}/\nu)^3 + 7.1^3}. \tag{3.25}$$

In general, performances of this model are rather good, especially for attached flows and mild-separation, while providing acceptable results for wakes and mixing layers [29].

## 3.3 Boundary layer

This section is based on the reference work by H. Schlichting and K. Gersten on boundary layers [32]. In the study of the aerodynamic behavior of a compressor stage, one of the key element is the boundary layer developing along the blades. This boundary layer indeed produces friction and some energy losses in the flow. The best would be to keep the flow laminar because the associated boundary layer produces less friction and thus less losses. However, it is rarely the case, especially when increasing the Mach number. Hence, the goal would be to keep a laminar boundary layer as far as possible towards the trailing edge. Separation could also occur, increasing drastically the losses.

Given a specific viscosity, every fluid adheres to the wall in order to fulfill the non-slip condition. The thin region of transition between the value of the mean flow velocity and the zero value directly against the wall is called the *boundary layer*. The higher the Reynolds number, the thinner the boundary layer, tending to zero for a flow with infinite Reynolds number (inviscid fluid). The viscosity in this region plays therefore a key role. The behavior of the BL varies depending on the nature of the flow *i.e.* whether it is laminar or turbulent. Indeed, laminar boundary layers exhibit smooth and regular streamlines, whereas turbulent boundary layers feature chaotic, random, and irregular streamlines, with significant mixing and a wide range of eddy scales. Turbulent BL are also thicker.

The simplest case is a boundary layer on a flat plate at zero incidence angle. This case is represented in Figure 3.1. Even if this very simple case is not often encounter in real world, it allows to highlight the main characteristics of the BL. The dashed line represents the thickness $\delta(x)$ of the boundary layer, which increases monotonically along the plate. However, as this thickness represents the distance at which the flow velocity is equal to the bulk velocity, it is more common to defined the thickness to be the height at which the velocity of the fluid is 99% of the mean flow velocity. Generally, the boundary layer starts in laminar and transition occurs towards the trailing edge of the body and leads to a turbulent BL. The evolution of the thickness is different in a regime or in the other, as such as the drag and the velocity gradient. Turbulent BL generate more drag and are thicker but are more resistant to separation than laminar boundary layers due to higher mixing. The mathematical description of the boundary layer is based on three parameters in addition to the thickness. Here, the parameters are defined for an uncompressible flow, although the flow present compressible effects in the present study. The first one is the skin friction coefficient, defined as follows

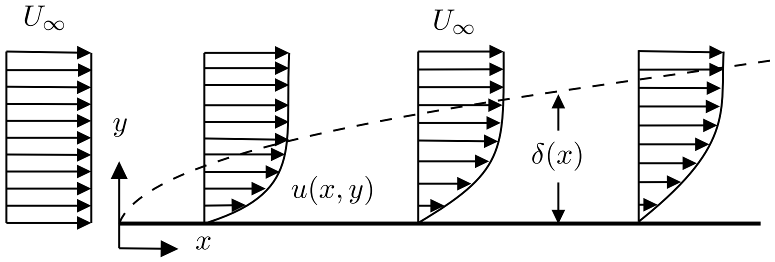

**Figure 3.1:** Boundary layer at a flat plate at zero incidence, reproduced from [33].

$$c_f = \frac{\tau_w}{\frac{1}{2}\rho U^2}, \tag{3.26}$$

where $\tau_w$ is the wall shear stress

$$\tau_w = \mu \left.\frac{\partial u}{\partial y}\right|_{y=0}. \tag{3.27}$$

The occurrence of $\tau_w$ and consequently $c_f$ reaching zero and subsequently changing sign indicates the moment when flow separates from the blade

The second one is the displacement thickness, which represents the change of displacement of the streamlines created by the presence of the BL. It is given by the following integral

$$\delta^*(x) = \int_0^\infty \left(1 - \frac{u}{U_e}\right) \mathrm{d}y, \tag{3.28}$$

where $U_e$ is the tangential velocity at the body surface from the inviscid solution [33]. Finally, the momentum thickness, related to the drag on the body, is

$$\theta(x) = \int_0^\infty \frac{u}{U_e} \left(1 - \frac{u}{U_e}\right) \mathrm{d}y. \tag{3.29}$$

The last two are combined to give the shape factor $H = \delta^*/\theta$, which gives a measure of the stability of the boundary layer, or its tendency to separation. The higher the value of $H$, the stronger the adverse pressure gradient and thus the more likely the flow separation. Those three parameters are linked in the von Kármán equation

$$\frac{\mathrm{d}\theta}{\mathrm{d}x} + \frac{\theta}{U_e}(H+2)\frac{\mathrm{d}U_e}{\mathrm{d}x} = \frac{1}{2}c_f. \tag{3.30}$$

To resolve this equation, a velocity profile is often assumed, and the different parameters are computed based on this profile. This method has led to remarkable results such as Polhausen, Thwaites's or Blasius methods, each of them giving evolution of the parameters along $x$. The boundary layers on both side of a blade (or any body inside a flow) join behind the trailing edge to form the wake, which will be discussed more in details.

### 3.3.1 Wall units

The flow inside the BL is characterized by special units called *wall units*. Indeed, in this region, viscosity and wall shear stress play a significant role and the flow is therefore characterized by those parameters rather than by the traditional ones. Those specific units are called the *viscous scale*.
Firstly, the velocity at the viscous scale is defined as the friction velocity

$$u^* = \sqrt{\frac{\tau_w}{\rho}}. \tag{3.31}$$

The distance to the wall is non-dimensionalized, with $y$ being the perpendicular direction,

$$y^+ = \frac{u^* y}{\nu}. \tag{3.32}$$

This is the characteristic wall coordinate distance and it is particularly used in computational fluid dynamic and in mesh generation as it measures the relative importance of viscosity and turbulence.

These wall units characterize the boundary layer and are used in similarity laws. Indeed, boundary layers obey universal laws of self-similarity when scaled appropriately $(u^+, y^+)$. This means that, in the absence of a pressure gradient and at equivalent Reynolds numbers, all boundary layers have the same shape. This scaling makes use of this skin friction velocity, which also explains why the first cell of the mesh must be placed at $y^+ \approx 1$, where $y^+$ can be interpreted as a local Reynolds number. Thus, the boundary layer is divided into three regions obeying different self-similarity equations: the wall law, the overlap region log-law and the law of wake.

The first and last layers are characterized by their respective scales, the *inner* and *outer layers*, while the zone between these two layers is called the *overlap region.* The inner layer is directly tangent to the body surface and the velocity inside it does not depend on mean flow scales. On the other hand, the outer layer connects the BL to the mean flow, which has a direct influence on the outer layer velocity profile. Without going into the details of the calculations, the three regions obey the following laws.

$$\begin{aligned}
&\text{Inner-viscous sublayer:} && u^+ = y^+, && 0 \leq y^+ < 5,\\
&\text{Log-law overlap region:} && u^+ = \tfrac{1}{\kappa}\ln y^+ + C^+, && 70 < y^+,\\
&\text{Outer law-of-wake region:} && u^+ = \tfrac{1}{\kappa}\ln(y^+) + C^+ + 2\tfrac{\Pi}{\kappa}\sin^2(\pi y/2\delta_{99}), && y \leq \delta(x),
\end{aligned} \tag{3.33}$$

with $C^+ \approx 5$, $\kappa = 0.41$ and $\Pi$, the wake parameter depending on the pressure gradient imposed in the fluid. The wake parameter is given by the emperical correlation

$$\Pi = 0.8(\beta + 0.5)^{3/4} \quad \text{with} \quad \beta = \frac{\delta^*}{\tau_w}\frac{\mathrm{d}P}{\mathrm{d}x}. \tag{3.34}$$

### 3.3.2 Boundary layer separation

Sometimes, in presence of high adverse pressure gradient, the flow separates of the body surface. Indeed, the flow reverses its direction and goes backward, causing the streamline to detach. The velocity gradient at this particular place vanishes and therefore the wall skin friction changes sign. A schematic of a separation on an airfoil is presented in the Figure 3.2. This separation is critical as it creates a large increase in pressure drag because the upstream flow "sees" a new body shape much larger than the original due to the streamlines deviation. Even if the separation also decreases the friction drag, the overall effect is a massive increase of the total drag coupled with a drop of lift on compressor blades. Moreover, in the separation region, the thin boundary layer assumptions no longer work. Laminar separation is also combined with turbulence transition, which can sometimes reattach to the surface, due to the higher resistance to separation of turbulent BL. When this occurs, it creates a "separation bubble" on the body surface.

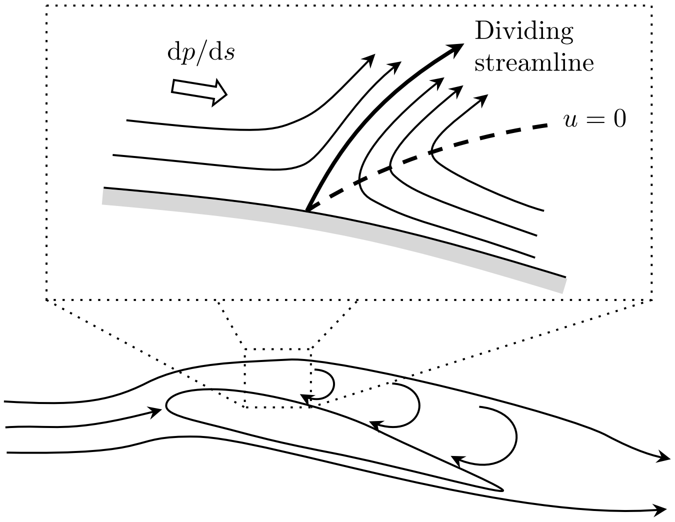

**FIGURE 3.2:** Flow separation on an airfoil extrados, reproduced from [33].

## 3.4 Wake

In free shear flows, wakes are regions of space behind a body in which the flow is affected by the presence of the latter. A planar wake behind an airfoil is represented in Figure 3.3. In this region, the flow is characterized by higher horizontal velocity than vertical velocity and lower gradient in the flow direction. That is, the mean flow is such that $\bar{u}_x \gg \bar{u}_y$ and $\partial_x \ll \partial_y$. Wake boundaries make the transition between a turbulent vorticity field inside the wake to an irrotational external motion. This space boundary varies in time, making the fluid in its vicinity to vary from turbulent to irrotational motion over time.

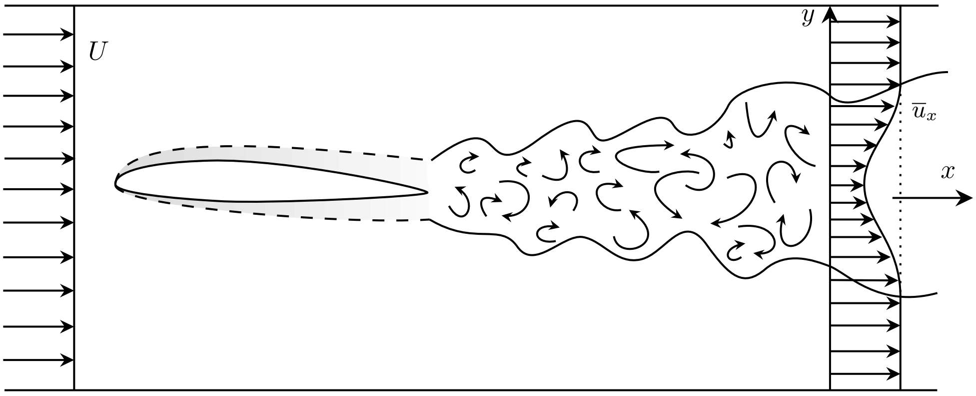

**Figure 3.3:** Wake behind an airfoil, adapted from [27].

Three main features are observed in wakes [33]:

- Reynolds stresses axial gradients are negligible with regard to transverse gradients *i.e.* $\partial_x \tau_{ij}^R \ll \partial_y \tau_{ij}^R$;
- laminar stresses can be neglected in front of Reynolds stresses;
- the main inertia term is mainly in the axial direction.

Using these simplifications, NSE lead to

$$\bar{p} + \rho \overline{\left(u_y'\right)^2} = \bar{p}_\infty(x) \tag{3.35}$$

with $\bar{p}_\infty(x)$, the pressure far away from the wake. That says, if $\left(u_y'\right)^2$ depends on $x$, the mean pressure inside the wake is function of $x$. Moreover, the above simplifications lead to simplified 2D momentum equation, expressed conveniently as follows for wakes,

$$\partial_x \left[\rho \bar{u}_x (U - \bar{u}_x)\right] + \partial_y \left[\rho \bar{u}_y (U - \bar{u}_x)\right] = -\partial_y \tau_{xy}^R, \tag{3.36}$$

where $U$ is the external flow velocity. The quantity $U - \bar{u}_x$ is known as *velocity deficit* [27] and represents the part of kinetic energy transferred to turbulence. Since this speed deficit tends towards zero as you move away from the wake's centerline, the *momentum deficit* is given by integration from $-\infty$ to $\infty$

$$D = \int_{-\infty}^{\infty} \rho \bar{u}_x (U - \bar{u}_x) \mathrm{d}y = \text{constant}. \tag{3.37}$$

In other words, the momentum deficit is constant along the axial direction. Moreover, let $\bar{u}_d$ be the velocity deficit, $\bar{u}_{d0} = \bar{u}_d(y = 0)$ and $\delta(x)$ be the local wake width, it can be demonstrated that $\bar{u}_{d0}$ and $\delta$ respectively scale as $x^{1/2}$ and $x^{-1/2}$. Finally, the deficit velocity profile is self-preserved, which means that $\bar{u}_d(x) = \bar{u}_{d0}(x) f(y/\delta(x))$.

# Chapter 4

# Numerical settings

This section presents the software tools and numerical methods used for this work. The various software packages will be briefly presented, followed by a description of the parameters used during submissions. Finally, the mesh used for all simulations will be presented, along with the process used to generate it.

## 4.1 Supercomputer Lucia and SU2

The simulations for this project have been performed on a supercomputer called *Lucia*. The building of this supercomputer was financed by the Walloon Region, it was manufactured by Hewlett Packard Enterprise (HPE) and is located in the AK6 ecosystem in Charleroi. Its operation is based on HPE Apollo systems from Axians, a subsidiary of VINCI Energies. This device is managed by Cenaero. It is composed of a CPU partition with 300 nodes, providing a computational performance of 1.1 Pflops, a GPU partition with 50 nodes, delivering 2.72 Pflops, and an additional partition comprising 2 GPU nodes dedicated to artificial intelligence tasks, which delivers 0.19 Pflops [34][35]. Lucia's overall maximum performance, combining both CPU and GPU partitions, reaches approximately 4 Pflops *i.e.* $4 \times 10^{15}$ floating operations per second. In a nutshell, we could say that Lucia's power is equivalent to more than 5,000 laptops combined with 6,000 game consoles [35]. The HPC (High Performance Computing) device has 121 TBytes of aggregate storage and a storage volume of 3 PBytes of disk space and 4 PBytes of archive space. It is also connected with high debit to the Belgian research network *Belnet*, and through it, to the European research network *GEANT*. A photo of Lucia HPC is shown in Figure 4.1.

The connection to Lucia is made through a Secure Shell (SSH) connection to login nodes. Access to this resource is restricted to internal Cenaero users, while external users can access it through CÉCI, "Consortium des Équipements de Calcul Intensif" [36]. CÉCI is a consortium of high-performance computing centers of UCLouvain, ULB, ULiège, UMons, and UNamur. The CÉCI is supported by the F.R.S-FNRS and the Walloon Region. It allows university members to connect to six different clusters in Belgium, one for each university plus Lucia, using a SSH gateway and the university VPN. Connection is via a unique key provided by CÉCI, enabling you to bypass the password step and the connection gateway and connect directly to Lucia's frontal nodes. Lucia has two different login nodes, and you are randomly connected to one of those two nodes.

**Figure 4.1:** Photo of Lucia Tier-1 HPC, taken from [34].

The HPC submission system comprises 10 different partitions, the main ones of which are listed with their characteristics in Table 4.1. For the present work, the *batch* partition was mainly used as it allows to fill one node with several small jobs using "Job arrays" and offers sufficient space and maximal computation time. In fact, RANS simulations are quite fast, rarely taking more than 15 min. Sometimes, when a small single simulation was needed, the *shared* partition was used to avoid using one entire node for such a little task.

**Table 4.1:** Lucia main partition characteristics [34].

| **Partition** | **Job type** | **N. of nodes** | **CPUs/node** | **Mem./node** [GB] |
|---|---|---|---|---|
| batch | MPI/SMP | 260 | 128 | 240 |
| medium | MPI/SMP | 30 | 128 | 492 |
| large | SMP | 7 | 64 | 20 000 |
| shared | Serial/SMP | 10 | 128 | 492 |
| gpu | GPU | 50 | 32 | 240 |
| debug | Debugging (CPU) | 10 | 128 | 240 |

### Job submission

Jobs are submitted using a *slurm* file, in which the required resources are declared. Slurm is an open-source cluster management and job scheduling system [37]. Slurm has three key functions: to allocate resources to users for a certain period of time; to provide a framework for starting, executing and monitoring jobs within allocated nodes; and to resolve existing conflicts when managing pending jobs. Thus, the number of nodes, the number of jobs per node, the way nodes are associated per partition, the simulation time required and the modules required for compilations must be declared. Simulations are then launched by compiling this slurm file. Following this, Lucia's queuing system allocates a slot according to the resources requested, which can take some time given the large but limited number of nodes available on the machine.

### 4.1.1 SU2

The SU2 suite is an open-source collection of C++ based software tools for performing Partial Differential Equation (PDE) analysis and solving PDE-constrained optimization problems [38][39]. Developed primarily by researchers and engineers at Stanfrod University, SU2 provides a comprehensive set of tools to solve computational fluid dynamic (CFD) equations and also aerodynamic optimization using unstructured mesh topologies although the core of the suite is a Reynolds-averaged Navier–Stokes (RANS) solver capable of simulating the compressible, turbulent flows that are representative of many problems in aerospace and mechanical engineering. It may also be used to solve other sets of governing equations such as potential flow, elasticity, electrodynamics, chemically-reacting flows, and many others. This software is still actively under development around the world on GitHub to further improve accuracy and capabilities.
One of the key features of SU2 is its ability to handle multiphysics simulations, coupling different physic phenomena such as fluid flow, heat transfer, and structural mechanics. The software also offers built-in modules to model turbulence, acoustics, heat transfers and other complex multiphyics problems, allowing users to analyze complex systems. The software relies solely on widely available open-source software including Message Passing Interface standard (MPI) implementations, mesh partitioning packages, and popular scripting languages. It can either be run serially or in parallel using a mesh partitioning approach, which will be used in the present work.

SU2 is also well documented, allowing to understand easily how to modify the working variables and functionalities to fit all specific needs. The software is written in a modular and object-oriented fashion, making it easy to integrate new solvers, algorithms, and user-defined features into the framework. SU2 uses both finite volume method (FVM) and finite element method (FEM). The compressible flows can either be solved with central or upwind spatial schemes and with either explicit or implicit time integration methods. The solver also includes many features to increase convergence and robustness, including residue smoothing and preconditioners for slower resolutions.

#### ParaView

ParaView is an open-source GUI (graphical user interface) software [40] used to do post-processing. It contains many features allowing to visualize and manipulate large datasets. For the present work, ParaView v.5.12.0 has been used for all the post-processing computations and the version v.5.11.1 has been used directly on Lucia inside the mesh searching process to provide the inlet Mach number at each iteration. ParaView is also executable in *batch* mode, allowing the user to jump the GUI step and get directly the desired data/figures/... needed by executing a python script, which can be generated directly on ParaView using the `trace` tool. All the following flow visualizations and most of data analysis has been performed thanks to ParaView.

## 4.2 Computational fluid dynamic settings

The turbulence modeling has been tested for two different cases: Spalart-Allmaras (SA) and the Shear-stress transport (SST). Those two models have been discussed in the previous chapter.

For the present study, the central scheme has been chosen and in particular the Jameson-Schmidt-Turkel (JST) scheme as it offers a good compromise between accuracy and robustness. For the turbulence equations, the only scheme available is the scalar upwind one. Both first and second order options are available but for this work, the default first order one is used. The upwind first order scheme is a good compromise between stability and precision. It leads to higher diffusion, by introducing numerical diffusion into the solution (artificial viscosity). This may lead to smooth out gradients and attenuate turbulent structures, particularly at fine scales and high wavenumbers, making the scheme relatively stable but less accurate. Indeed, by attenuating oscillations in the flow, it prevents the growth of numerical instabilities and divergence. Finally, first-order schemes are less dependent on mesh quality, being less sensitive due to their diffusive nature [41]. Time discretization is Euler-Implicit so that the scheme is unconditionally stable. The linear solver used is GMRES (Generalized minimal residual) method. This method approximates the solution by a vector of the Krylov subspace with minimal residual.

### 4.2.1 Jameson-Schmidt-Turkel scheme

The Jameson-Schmidt-Turkel scheme, named after its creators, is an implicit, upwind, finite volume method used for compressible flows simulations. It has been designed to capture shock waves and resolve steep gradients in high-velocity flows. The JST scheme has been made to satisfy some design principles [42]:

1. the conservative form must be satisfied to ensure correct shock jump conditions, according to Lax and Wendroff theorem;
2. second order accuracy in smooth region of the flow;
3. no overshoot or oscillation in steady state around shock waves capture;
4. steady state independent of time step;
5. ensure stability when using variable local time steps at fixed CFL number in order to accelerate convergence;
6. ensure constant stagnation enthalpy for discrete steady state solutions.

The JST scheme also offers good behavior for unstructured meshes which made him a prime candidate for CFD software such as SU2. For the present work, the second an fourth order dissipation coefficients were set to 0.5 and 0.02 respectively.

### 4.2.2 Boundary conditions

Inlet conditions have been chosen to describe total conditions. Hence, the total temperature, the total pressure and the flow direction are set at the inlet. At the outlet, only the static pressure is fixed. The lateral sides conditions are periodic, the solution on the suction side must coincident with the one on the pressure side of the domain. The total temperature is fixed to 303.33 K for all simulations. The inlet total pressure and the outlet pressure are modified, and more precisely their ratio, depending on the studied scenario to obtain a Mach number of 0.6 at the inlet. One of the main complications lies in the choice of this ratio, since the Mach number can only be found as output after the model has been solved, requiring an iterative process for each change in geometry or inlet flow angle. Indeed, it is not possible *a priori* to predict the input Mach number for a given configuration.

### 4.2.3 Automatic inlet Mach number search process

The first approach to solve the problem described here above was to test outlet conditions, launch a simulation, then retrieve the corresponding results to local and if the inlet Mach number value was not sufficiently close to 0.6, try again with an other outlet pressure and so on. This was extremely time-consuming, since it required to wait for the jobs to be submitted, for the simulation to finish, and then send back and analyze the results, doing one simulation at a time, and this process should have been done for all the different simulations and configurations, since a change in geometry entails a change in pressure ratio and therefore in inlet Mach number. To overcome this problem and avoid to edit manually the outlet pressure conditions each time, a more automatic approach has been used for the present work. The main idea was to use the Mach number at the inlet at the iteration $n$ to modify if needed the outlet static pressure in the ".cfg" file and relaunch a simulation, doing all this on Lucia. This iterative method is based on the secant method [43]. Hence, the outlet pressure at iteration $n+1$ is given by

$$p^{(n+1)} = p^{(n)} - \frac{p^{(n)} - p^{(n-1)}}{M_{\text{res}}^{(n)} - M_{\text{res}}^{(n-1)}} M_{\text{res}}^{(n)}, \tag{4.1}$$

where $M_{\text{res}}$ is the inlet Mach number residual ($M_{\text{in}} - 0.6$). To obtain the inlet Mach number value at iteration $n$, a small paraview python script is used to calculate the mean inlet Mach number based on the solution at iteration $n$. Looking at equation (4.1), it appears that the pressure at iterations 0 and 1 need to be known to find $p^{(2)}$. Hence, the iterative method necessitates two first guesses to start iterating on itself. Theoretically, the first guesses could be randomly chosen, and the iterative method would do the rest. However, this method is based on calculating the slope of the straight line passing through the points of iterations $n$ and $n-1$. Because of this, if the slope is very low, due to bad first guesses for example, it can lead to outliers in output pressure, such as negative values or values that are too high. Negative values induces Mach numbers that are far too high, in which case shocks appear in the solutions, or they never converge. Conversely, pressure values that are too high can force the fluid to move in the opposite direction. These solutions should be avoided at all costs, as they can quickly lead to compilation errors. Therefore, the two first guesses must be chosen carefully, the best is to have values on both sides of the desired value.

Nevertheless, since the values change over the iterations, extreme values may still occurs. To mitigate this, a relaxation factor is introduced in the formula (4.1) to limit the pressure ratio inside an acceptable range, reducing by half the interval between the new value and the old one if the pressure values at iteration $n$ and $n+1$ stand on the same side of the goal value. While this approach may not be the most efficient method for implementing secant relaxation, it successfully worked for all simulations and thus has remained unchanged. Apart from that, the secant method offers very good convergence, of order 1.618; this convergence is known as superlinear. The iterative process stops when the inlet Mach number enters the tolerance range, fixed here to be $0.6 \pm 0.05$. At each iteration, the process also check if the compilation exited successfully and if the solution converged.

## 4.3 Mesh

The meshing part of the numerical simulation is critical. Indeed, computational fluid dynamic highly depends on the mesh generation, especially in the regions of large gradients such as the boundary layers or the wake. As explained before, along the blades, the first cells must satisfy $y^+ = 1$ to capture the information inside the boundary layer. Indeed, when $y^+$ is close to 1, this means that the size of the first boundary layer cell is of the order of the fluid viscosity. This makes it possible to accurately capture viscous transport phenomena near the wall, such as energy dissipation and fluid velocity variation. A value of $y^+$ close to 1 ensures that the mesh is fine enough to correctly represent the boundary layer, while avoiding over-resolution that would lead to an unnecessary increase in the number of cells in the domain. Having a value of $y^+$ close to 1 at fluid-solid interfaces is therefore important for accurate simulation results, especially in regions where viscous transport phenomena dominate, such as flow resistance or heat exchange near solid walls. It also ensures that numerical solutions converge well. In the rest of the flow, however, the cells size can be relatively large, with regard to the ones in the complex region because not much changes occur.

The mesh generation has been made using `GMSH` [44], an open-source three-dimensional finite volume and finite element grid generator software. A special treatment has been made inside the boundary layer and in the wake region. To verify the $y+$ condition, the solution is required, so that the meshing process is iterative. Indeed, to obtain $y^+ \approx 1$ along the blades, a first coarse design is used, and the solution is used to compute $y^+$. Afterwards, the mesh is refined if necessary to meet this requirement.

### 4.3.1 Methodology

To achieve an optimal mesh, a mesh study is conducted. Initially, a coarse mesh comprising approximately 4000 cells is generated. A simulation is conducted using this initial mesh, denoted as $M_0$, with its corresponding cell count $N_0$. Subsequently, a second mesh $M_1$ is created, with $N_1 \approx 2N_0$. The results corresponding to this mesh are compared with the initial ones. This can be done by checking one value, say the pressure on a line at the location $x = x_0$. If the root mean square difference between those two results is greater than 1%, a new mesh is made with $N_2 = 2N_1$ and so on. When the difference between two results using two consecutive meshes $M_{n-1}$ and $M_n$ is lower than 1%, it means than the mesh at the step $n-1$ is refined enough, and thus, the mesh $M_{n-1}$ is conserved as final mesh. Note that a special attention is given to the values of $y^+$ all over the blades. Indeed, although the results has converged, if the $y^+$ condition is not satisfied, the boundary layer region will need to be refined.

The root mean square error between two consecutive results is computed with the following formula

$$\varepsilon_{rms} = \sqrt{\frac{1}{n}\sum_{i}^{n}\left(\frac{x_i^{(n-1)} - x_i^{(n)}}{x_i^{(n-1)}}\right)^2}. \tag{4.2}$$

As the mesh versions increase, the number of cells also increases, leading to a larger dataset. Consequently, the root mean square (RMS) error is calculated based on the data from $M_{n-1}$. Only the cells that correspond to coordinates closer to those of the cells in $M_{n-1}$ are used for this calculation. The location $x = 1.51$ m is selected as it is the one that will be used later for the results.

### 4.3.2 Mesh iteration

The first mesh has been made voluntary coarse, composed of about 4000 cells. This mesh is highly bad, the cells areas vary abruptly in some regions and important regions are not refined properly, such as boundary layers and wakes. It is a safe bet that the results related to this mesh will be poor. Figure 4.2 partially shows the initial mesh. As it can be seen on the figure, the gap, for example, clearly needs to be refined. This has to be done for each new mesh, so the number of mesh cells is more or less doubled but with a special consideration for zones of

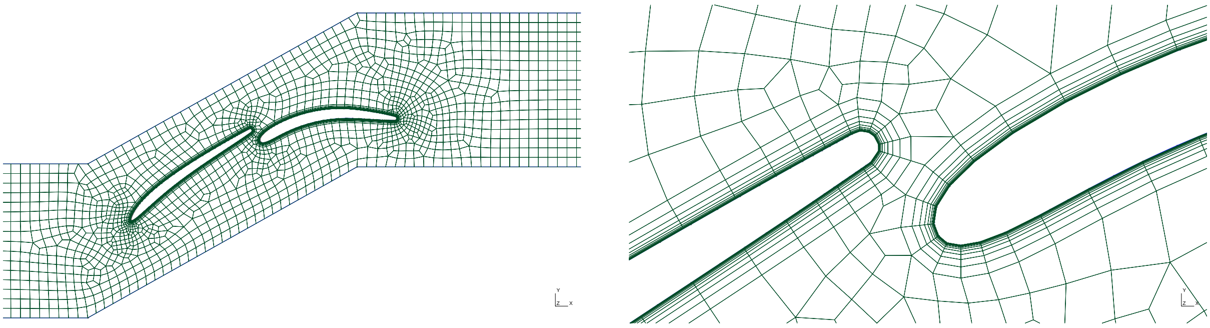
**(a)** General overview.
**(b)** Initial mesh zoom in the gap.

**Figure 4.2:** Initial mesh.

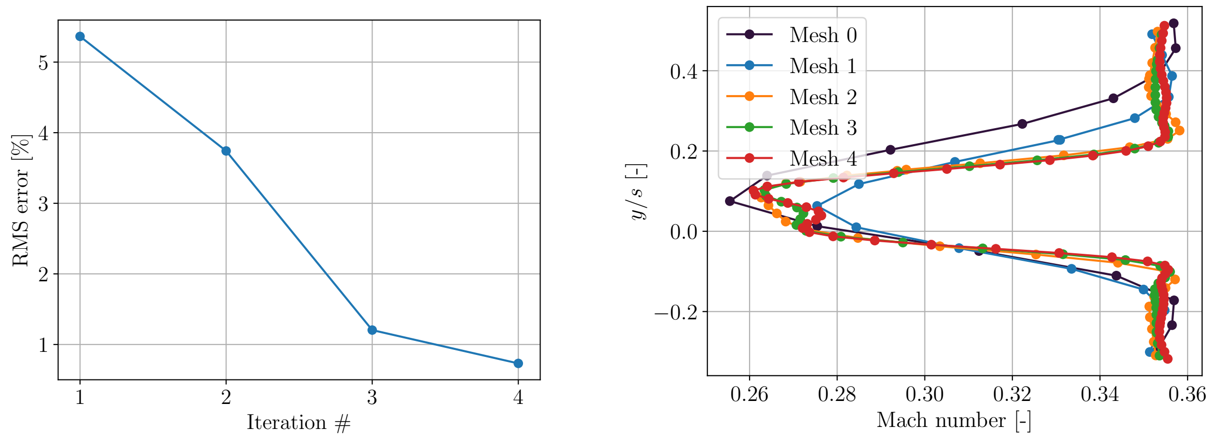

**(a)** RMS error, using Mach number values measured at $x = 1.51$.

**(b)** Mach number values measured at $x = 1.51$ for each different mesh.

**Figure 4.3:** Mesh study: iterations and comparison.

interest.

Figure 4.3a represents the evolution of the RMS error between two consecutive meshes. It can be seen that the error is relatively high for the two first iteration, which reflects large differences between the meshes. However, from the third iteration, the error becomes small and reaches the error tolerance for iteration four ($< 1\%$). This means that the differences between the mesh 3 and 4 are sufficiently small and thus, the mesh 4 is not needed since the mesh 3 offers lower complexity and computational time and equally good results. Indeed, in Figure 4.3b, it can be seen than the meshes 3 and 4 give very similar solutions. Figure 4.3b also shows a convergence in the solutions, which is always a necessary condition for mesh studies. The mesh iterations are given in Table 4.2.

**Table 4.2:** Mesh study iterations.

| Mesh number | Number of cells | RMS error $\varepsilon_{RMS}$ [%] |
|---|---|---|
| 0 | 4250 | - |
| 1 | 8419 | 5.52 |
| 2 | 17 469 | 3.93 |
| 3 | 35 053 | 1.21 |
| 4 | 69 878 | 0.72 |

### 4.3.3 Final mesh

The final mesh is represented in Figure 4.4. Recall that the mesh must satisfy $y^+ \approx 1$ all around the blades surfaces. Figure 4.5 represents the values of $y^+$ along the blades. A large majority of values of $y^+$ are under one and all of them satisfy the condition, the maximum value is found to be 2.5. Thus, all the cells at the wall are still located in the viscous sublayer ($y^+ < 5$). As explained previously and as it can be seen on the zoom made on the mesh in Figure 4.4, leading edge, trailing edge and gap regions has been particularly refined to ensure smooth transition between the boundary layer regions and the rest of the mesh. Moreover, the two wakes, behind each of the blades, have been refined to capture the complex fluid motion developing in these regions, increasing gradually cell size as it moves away from the trailing edge. The boundary layer parameters on GMSH have been setup in order to satisfy $y^+$ condition for the first cell against the surface, increasing progressively cell dimension perpendicularly to the wall to reach almost square shaped cells at the transition between the BL and the bulk mesh. High curvature region, such as blades extremities, need more refinement than the rest of the BL to keep approximately the same cell aspect ratio at the transition.

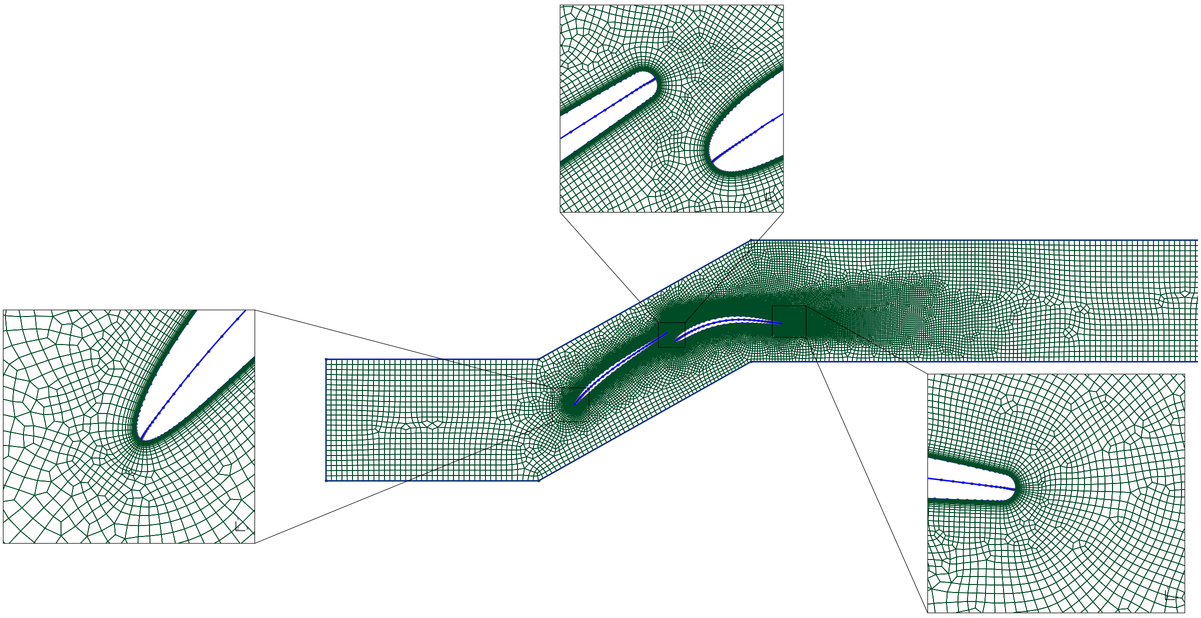

**Figure 4.4:** Final mesh.

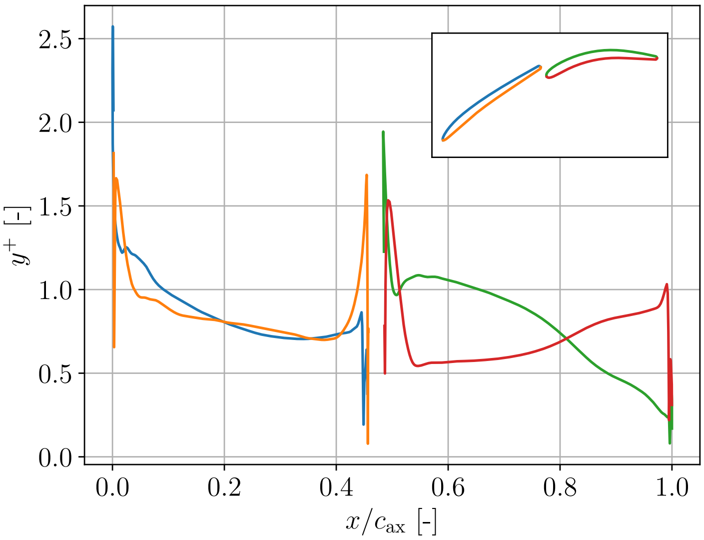

**Figure 4.5:** $y^+$ values at the blades surfaces at $\text{Mach}_{\text{in}} = 0.6$, with SST turbulence model.

### 4.3.4 Mesh quality

Although there is no absolute standard of metric to assess the mesh quality, there are a certain number of good practice rules that should be respected as much as possible. The most common mesh metrics (among many others) to check are [41][45]:

- Orthogonality,
- Skewness,
- Aspect ratio,
- Smoothness,
- Mesh element type.

Those metrics can only be measured after the mesh generation so it is only possible to generate meshes and check them afterwards. Mesh orthogonality measures the deviation between the vector connecting two cell centers and the vector normal to the cell surface. It affects the gradients at the cell centers and adds numerical diffusion to the solution as it affects diffusive terms. The orthogonality should be as low as possible. The skewness determines how close to the ideal shape a cell is. Hence, a value close to zero indicates an equilateral cell and a value close to one, a degenerate cell. Skewness affects the interpolation of the cells centered quantities to the face center. It adds numerical diffusion and wiggles the solution by affecting both convective and diffusive terms. A good mesh should keep the skewness between 0 and 0.5. The aspect ratio is the ratio between the longest edge length to the shortest edge length. It affects gradients but large aspect ratios are acceptable if the gradients along the largest direction are small. For example, the boundary layer elements present large aspect ratio but gradient are rather small in the wall tangential direction. For hexahedral elements, the cell aspect ratios should be close to 1. Smoothness characterizes the cell size transition between contiguous cells. Large transition adds diffusion in the solution and a good mesh practice is to keep this transition ratio under 20%. Finally, mesh element type also play a role in the mesh quality: triangular and tetrahedral elements are more subject to larger truncation error than hexahedral elements. In other words, for a same cell number, hexahedral meshes will provide more accurate solutions.

The mesh is composed of 34997 quadrangles and only 2 triangles, which satisfy the element type quality condition. The mesh aspect ratio is shown in Figure 4.6 and the skewness in Figure 4.7, using paraview `Mesh Quality` filter. The aspect ratio is between 1 and 1.5 for the vast majority of the mesh, except in the boundary layer region. However, as explained above, this area allows for high aspect ratios. Particular attention is paid to the high-gradient wakes behind each blade. Here we can see aspect ratios close to 1, which ensures a good mesh quality from the AR point of view. As a reminder, the skewness should be as low as possible. Here, it is largely situated under 0.5 except for a few elements. In particular, the skewness is close to zero in the boundary layer region and situated between 0 and 0.2 for most of the wake zones. Here again, skewness mesh quality is acceptable. The smoothness, albeit not measured directly for the entire domain has been chosen carefully in the mesh generation, particularly in complex regions such as boundary layer and wake, to ensure a maximal cell dimension difference below 20% when possible, and 30% otherwise. Finally, SU2 does not measure the orthogonality condition. Thus, the only way to ensure good mesh quality for this parameter is through careful mesh generation, for example by imposing a particular mesh in the boundary layer zone, whose cells are aligned with the surface and parallel to each other. In this way, the orthogonality condition is satisfied qualitatively, since it cannot be investigated more precisely.

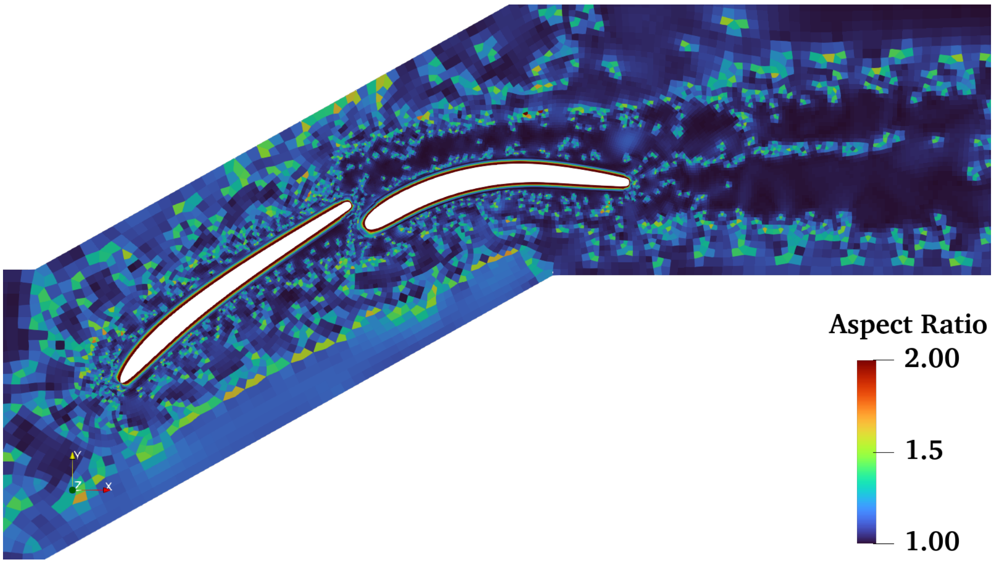

**Figure 4.6:** Mesh quality: aspect ratio.

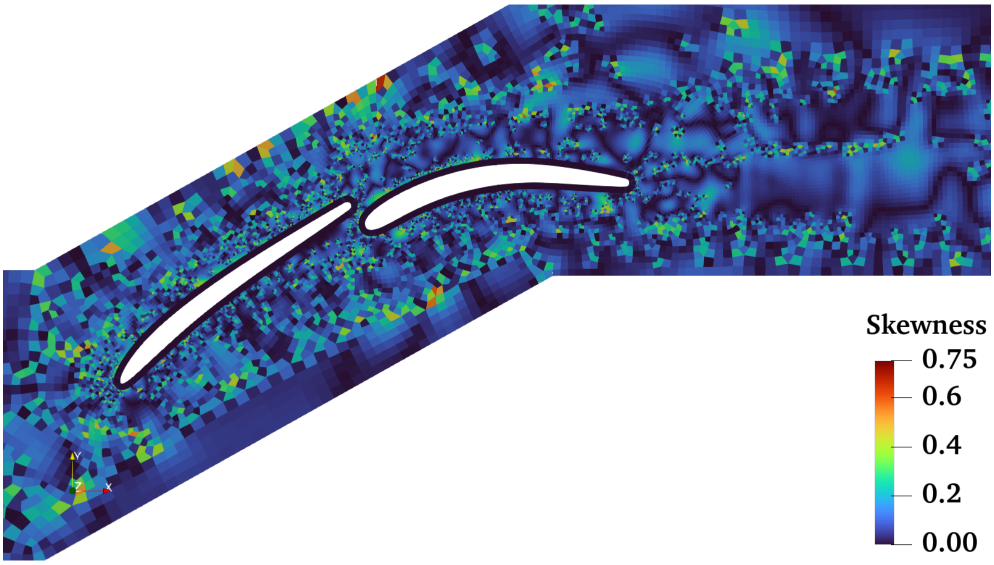

**Figure 4.7:** Mesh quality: skewness.

# Chapter 5

# Results

The results of simulations carried out for different outlet guide vane strategies are presented here. First, the initial configuration is presented, *i.e.* the tandem configuration with no change in the front blade angle. Subsequent cases are compared with this initial configuration. Thus, the front blade angle $\chi_{FB}$ will often be referred to as the angle of rotation with respect to this initial configuration, to avoid using absolute values that are not very meaningful. Finally, the different strategies will be compared to determine which is/are the best one(s).

Note that all the results presented below are often based on flow in and flow out. The required quantities were measured at the same respective locations, to ensure uniformity of results. Thus, when we refer to the quantities upstream of the flow (the quantities $\boldsymbol{v_1}, \alpha_1$,... in Figure 2.11), they are measured at the entrance of the domain ($x = 1.43$ m in absolute value). The outlet values of the flow ($\boldsymbol{v_2}, \alpha_2$) are measured at location $x = 1.51$ m, *i.e.* 8 cm after the domain entrance and 1.55 cm downstream of the trailing edge of the rear blade. This location was chosen because it offers a good compromise between being close enough to the blades to capture important complex phenomena and being far enough away to allow the main phenomena such as wake to have had time to develop and stabilize. What is more, as we saw earlier, even if the shape of the wake varies according to $x$, the moment deficit is preserved and the results would not be altered (see section 3.4).

## 5.1 Baseline tandem configuration

In order to correctly understand the flow physic for modified geometries, this section firstly investigates the main flow characteristics for the initial configuration *i.e.* unchanged geometry, inlet Mach number of 0.6 and inlet flow angle of 50° with $\text{Re} \approx 6.5 \times 10^5$.

### 5.1.1 Comparison between turbulence models

The differences between the two turbulence models available in SU2 are investigated in order to find out if they are significant or not. In this case, further investigations will be mandatory to select the model that best describes the flow. The difference is computed using the RMS error, equation (4.2).

It turns out that the RMS difference between the two models for Mach number values at $x = 1.51$ m is about 1.5% and 0.5% for pressure coefficient on the blades. The two results are represented in Figure 5.2. It appears that SA model is less dissipative than SST model. As the two models are relatively close, and the RMS differences are low, the SST model is chosen for all further computations as it is more widely used in industry.

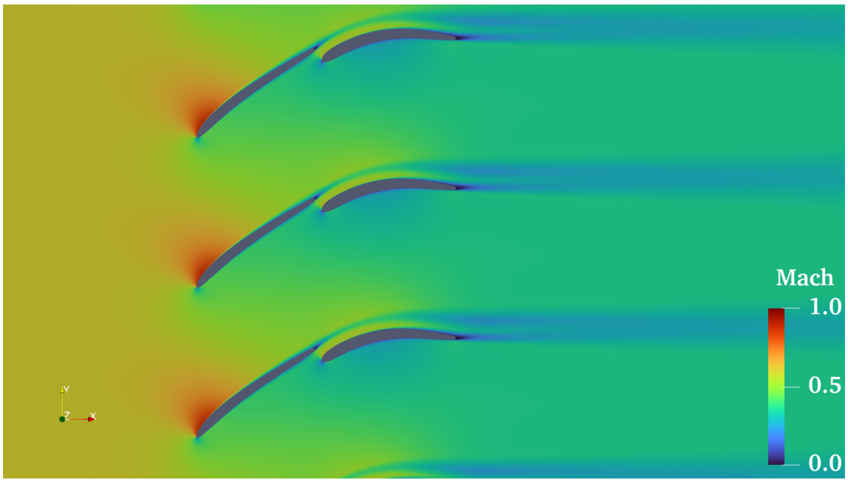

**Figure 5.1:** Mach number for initial configuration, for inlet Mach number of 0.6, using SST turbulence model.

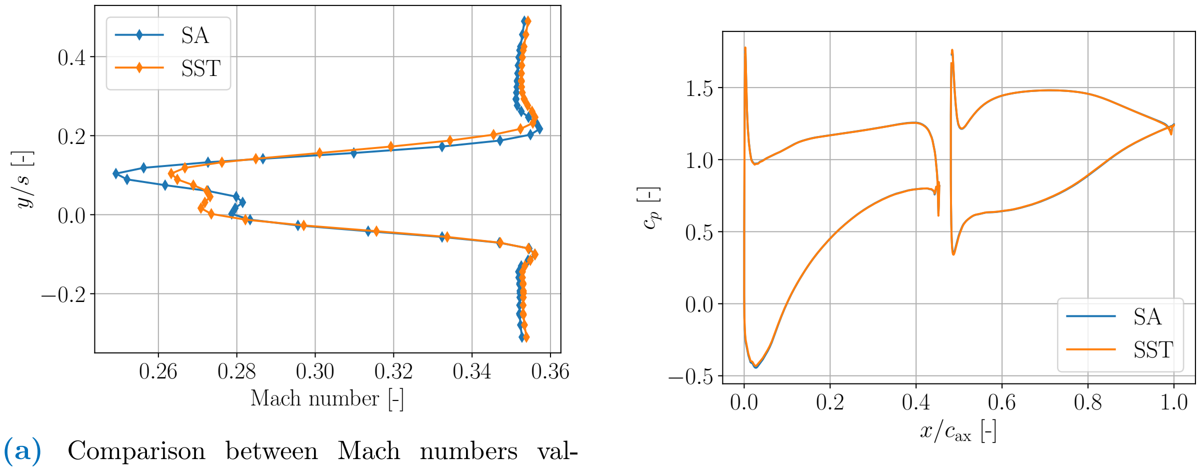

**(a)** Comparison between Mach numbers values with SA and SST turbulence models at $x = 1.51$ m.

**(b)** Comparison between $c_p$ values with SA and SST turbulence models on blade surfaces.

**Figure 5.2:** Comparison between turbulence models, in the flow and on the blades.

### 5.1.2 Flow characteristics

To characterize the flow in the direct vicinity of the blades, the isentropic mach numbers and the skin friction coefficients are computed around the blades and are respectively represented in Figure 5.3a and 5.3b. The isentropic Mach number on the blades indicates a high loading on the leading edge of the front blade and this load rapidly decreases towards the trailing edge. The isentropic Mach curve for the first blade is very close to the *optimal* one, which is most of time desired in design operation, called *Prescribed velocity distribution*. The second blade is less loaded but still undergoes a load peak on the very first part of the pressure side trailing edge. The skin friction coefficient remains positive all around the blades, meaning that flow separation does not occur. However, the friction is much higher on the leading edge of both blades and then decreases towards the trailing edge. This is because the boundary layer is almost fully developed, so velocity gradients in the perpendicular wall direction $\partial u/\partial y$ at the wall in these regions are weaker.

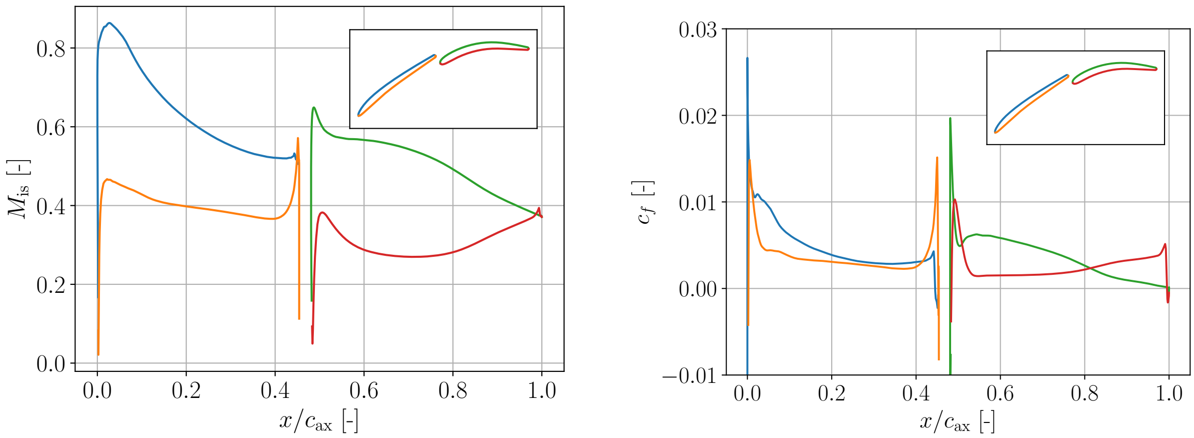

**(a)** Isentropic Mach number around the blades. **(b)** Skin friction coefficient around the blades.

**Figure 5.3:** Flow characteristics around the blades.

### 5.1.3 Incidence angle influence

Various inlet flow angles have been studied around the initial configuration. The simulations were performed for angles from 36 to 60 degrees because more extreme values lead to unsteady solutions, which are beyond the scope of this work. The loss and pressure coefficient discrete integrations use mass flow averages. This is, the values used are the sum of the cells averages multiplied by the normalized flow passing through the cell, using the following formula

$$\tilde{X} = \frac{\sum_i X_i \times A_i v_i \rho_i}{\sum_i A_i v_i \rho_i}, \tag{5.1}$$

where $i$ is the index of the cell on the considered line (here $x = 1.51$ m), $X_i$ is the value to be integrated, $A_i$ the cell area, $v_i$ the velocity and $\rho_i$ the density.

Figure 5.4a shows the integrated loss coefficients for a large range of flow angles and Figure 5.4b shows the pressure ratio evolution. Without any modification of the first blade orientation, the relative incidence will be negative for inlet flow angle below 50° and conversely above 50°. We can ideally divide the flow angle range into two areas: the central region around 47° where losses are low and the pressure rise is relatively high, and the side regions where performances decrease dramatically, with loss coefficient almost multiplied by a factor of eight and pretty low pressure rises (almost tend to zero for low incidence angles). As the purpose of compressors is to achieve high compression ratios, and tandem configurations are particularly interesting for high loadings, high work coefficients and low flow coefficients (see (2.6)) near surge limit, particular interest is paid to the right-hand side of the graph. Indeed, it appears that it could be possible to reach static pressure ratio of almost 1.2 for incidence angle such as 55°. From the definition introduced before, the incidence angle operating range is found to be 14.7° with a minimal loss of 1.2% and the reference angle is 46.8°. The remaining question would therefore be: is it possible to find a better tandem configuration that allows to diminish the losses while preserving this pressure ratio, and in the end being able to extend the operating range?

The performance parameters of the baseline configuration are listed in Table 5.1 with comparison to extreme cases at 36° and 60° of incidence. At 50° of inlet flow angle, the diffusion factor is already very high, indicating high blade loading and would present risks of separation on a single regular blade. Moreover, the load split is close to 0.5 and therefore, the tandem blade seems to do the trick and would probably reduce overall losses with comparison to a single blade as Leiblein suggested [6]. Finally, the lift to drag ratio is close to 70, which is a sign

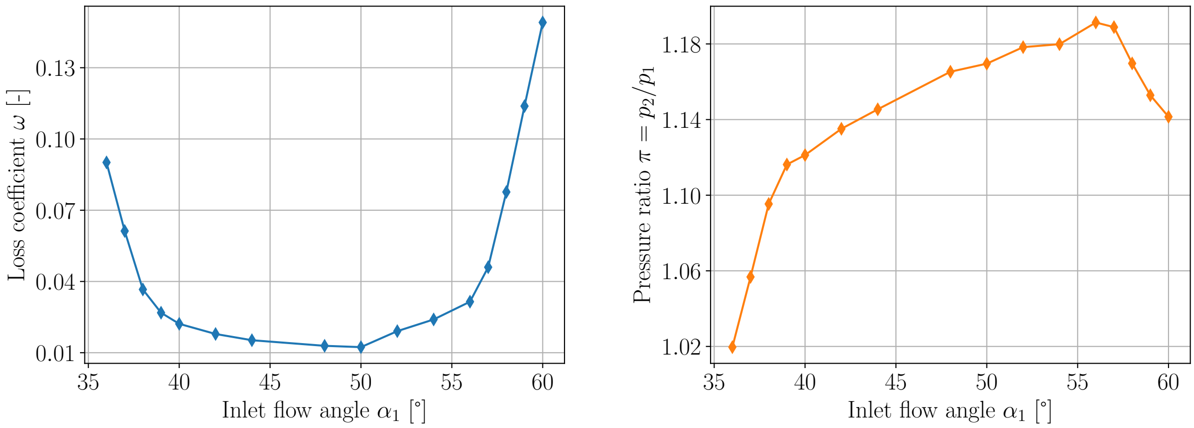

**(a)** Loss coefficient evolution with inlet flow angle for baseline configuration.

**(b)** Static pressure ratio evolution with inlet flow angle for baseline configuration

**Figure 5.4:** Loss and static pressure ratio results around baseline configuration.

**Table 5.1:** Baseline performances parameters.

| Inlet flow angle | $\omega$[%] | $\pi$ | DF | LS | $C_L$ | $C_D$ |
|---|---|---|---|---|---|---|
| 50 | 1.20 | 1.17 | 0.64 | 0.56 | 0.68 | 0.01 |
| 36 | 9.01 | 1.02 | 0.24 | / | 0.18 | 0.06 |
| 60 | 14.91 | 1.14 | 0.69 | 0.48 | 0.93 | 0.15 |

of particularly good stage performances. For negative relative incidence, the diffusion factor is low and the pressure rise rather small. The load split is not given because the diffusion factor on blade one is negative and therefore non physical but the lift to drag ratio is only 3, which indicates bad blade performances. At high inlet flow angle, the diffusion factor is very high and thus, tandem configuration makes sense and the load is almost equally split between front and rear blades. However, losses are very high and lift to drag ratio only around 6.2.

### 5.1.4 Flow visualizations

In order to better understand the evolution of the performances depending on the flow incidence angle, different quantities are represented here above for the extreme off-design inlet flow angles (36 and 60 degrees) and the basic flow conditions (50 degrees). The evolution of pressure and flow angle along the center streamline passing in the midchanel is represented in the Figure 5.5, with the corresponding streamlines represented above. It can be seen that the orange curve, corresponding to the lowest incidence angle absolute value, unsurprisingly behaves best. For low inlet flow angle (blue curve), the pressure drops drastically in the first part of the front blade but increases towards the trailing edge, although the pressure hardly reaches the inlet pressure level when leaving the second blade trailing edge due to a second pressure drop. Inspecting its corresponding streamline on the second figure, it is clearly visible that the outlet flow angle does not reach zero after the blade passage. This results in bad performances since the remaining vertical velocity represent a part of energy which has not been converted in pressure and therefore low work coefficient. High inlet flow angle, however, seems to behave similarly to the reference case, although the pressure decreases slightly towards the second blade trailing edge. However, the turning being more important, especially on the first blade, as can be seen on the second figure, the pressure rise could be higher, in absence of loss. For each case, a small increase in flow angle occurs just before the front blade leading edge, corresponding to a mild drop of pressure. In order to understand what phenomenon causes the bad performance of extreme flow

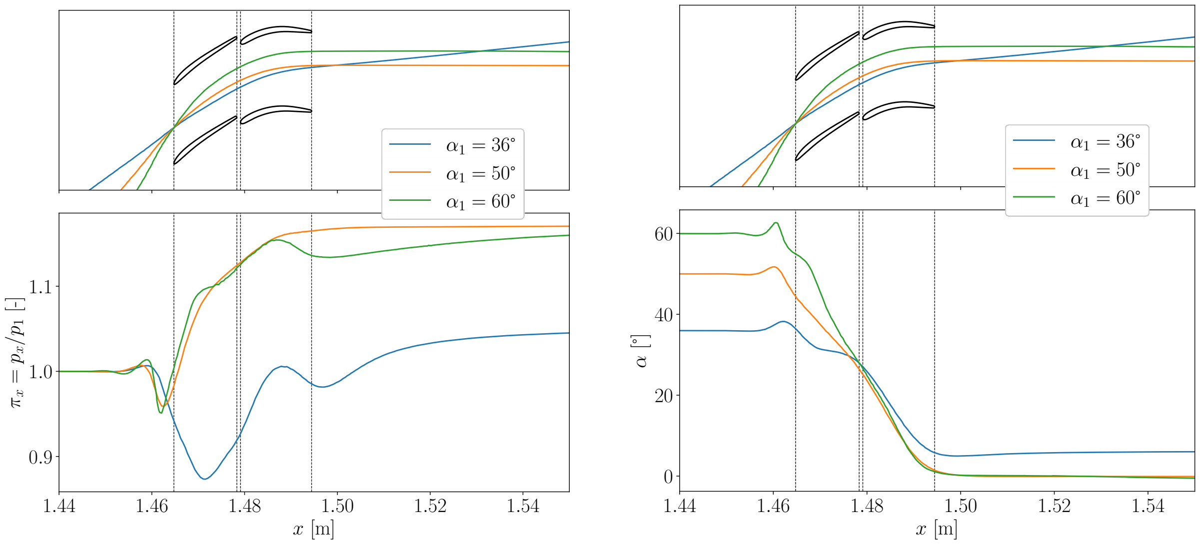

**(a)** Pressure evolution.

**(b)** Stream angle evolution.

**Figure 5.5:** Streamline quantities evolution.

angles, flow quantities have been inspected here below more closely for the three cases. For all the comparison figures, the same scale have been used for the three cases to facilitate the understanding and the comparison.

### Mach number and velocity

Figure 5.6 shows the Mach number for each inlet flow angle, (velocity is shown in Appendix A.1 in Figure A.1). For low flow angles, the flow accelerates in the front blade region, leading to the pressure drops observed here above. It should be noted that such conditions inducing high Mach values could lead to chocking if the inlet Mach number is slightly increased. Indeed, at this very low incidence angle, the flow sees the tandem blades as an obstacle to its passage and the flow area is therefore virtually reduced. As the mass flow remains constant, the flow accelerates, decreasing the pressure. Hence, as described by Dixon et al. [9], the inlet flow angle at which chocking occurs is given by the simplified equation

$$\cos\alpha_1 = f(M_1)\frac{A^*}{H_1 s} \tag{5.2}$$

where $H_1 = \rho_1 v_{u1}$ and $A^*$ is the minimal flow area. Therefore, as the inlet flow angle is reduced, $v_{u1}$ increases and the flow is more likely to experiment chocking. Once the flow starts to turn, this effect weakens and the pressure rises again. Moreover, while the wake is expending in the axial direction for 50 and 60 degrees angles, it is clearly also expending in the transverse direction for 36 degrees of incidence. For positive incidence angles, a large zone with low velocity magnitude is observed on the first blade pressure side. This region corresponds to flow separation. For negative incidence angle, separation occurs on the second blade because the first blade is not able to change the flow direction enough so that the flow can not follow the second blade surface. This separation corresponds to the second pressure drop observed in the Figure 5.5a. Finally, the mild drop of pressure observed before the front blade leading edge can be relied to the rapid acceleration of the fluid around the leading edge, especially for 50 and 60 degrees of inlet flow angles.

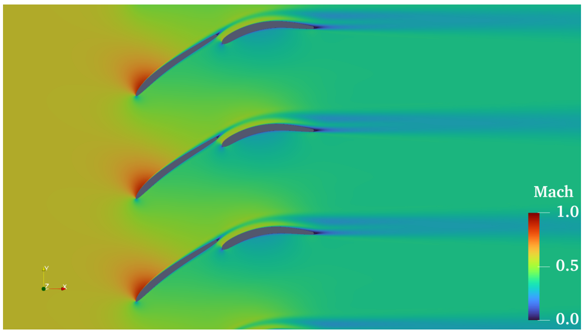

**(a)** $\alpha_1 = 50°$, $i = 0°$.

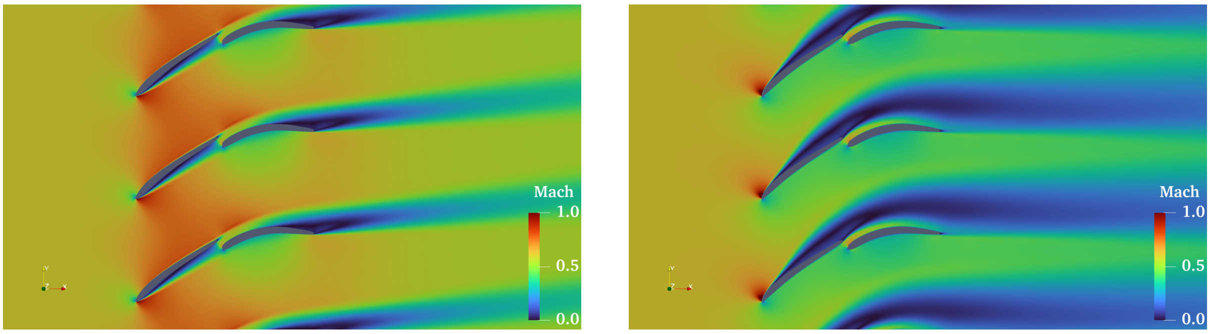

**(b)** $\alpha_1 = 36°$, $i = -14°$. **(c)** $\alpha_1 = 60°$, $i = 10°$.

**FIGURE 5.6:** Mach number comparison for inlet flow angle of 36, 50 and 60 degrees, with baseline configuration.

### Total Pressure

Figure 5.7 represents total pressure. For zero degree of incidence (50°), the total pressure is almost preserved anywhere in the flow, resulting in low losses in the wake region whereas the wake regions for the extreme angles are more widely and severely extended. For negative incidence angle (36°), the wake region is thinner than for a positive incidence angle but the total pressure gradients are more severe. In facts, a positive incidence angle leads to wider wakes with lower loss magnitude. However, ultimately, the width of the wake has a more significant impact on total losses. Moreover, the separation region on the first blade results in high total pressure losses. Finally, for $\alpha_1 = 36°$, front blade suction side region presents high total pressure losses, indicating flow separation. Thus, there seems to be two separations on each side of the tandem stage for negative incidence angle. Separation is represented in more details in Appendix (section A.1) for both low and high inlet flow angles, respectively in Figure A.2 and A.3.

### Turbulence quantities

The wake is the main source of losses and is characterized by high turbulence level. Turbulent quantities help to understand the main flow differences between the cases for the inlet flow angle considered so far. Firstly, Figure 5.8 shows the adimensional turbulent kinetic energy. The adimensional turbulent kinetic takes into account the free stream velocity, as it varies from one case to another. It is given by the following formula

$$k^\star = \frac{k}{v_\infty^2}. \tag{5.3}$$

It is clearly visible that turbulence is significantly lower for $\alpha_1 = 50°$ compared to the other cases. For positive incidence angle, the large recirculation region above the blades shows the high turbulence level in the separation region. It is also interesting to note that, for negative

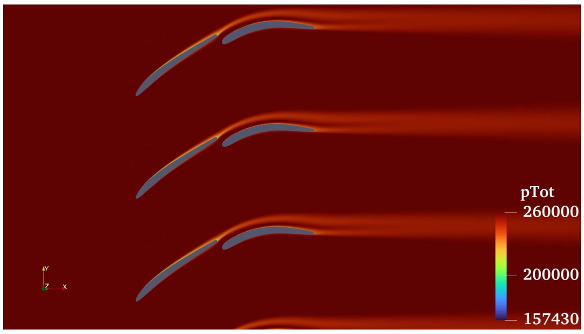

**(a)** $\alpha_1 = 50°$, $i = 0°$.

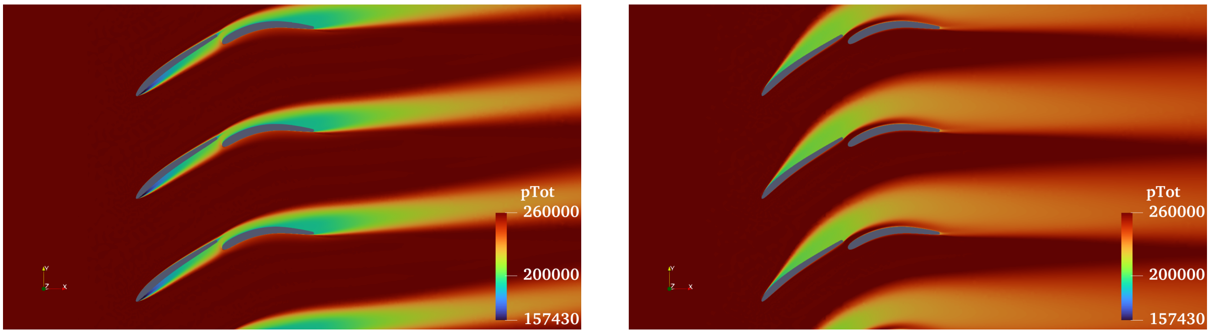

**(b)** $\alpha_1 = 36°$, $i = -14°$.

**(c)** $\alpha_1 = 60°$, $i = 10°$.

**Figure 5.7:** Total pressure comparison for inlet flow angle of 36, 50 and 60 degrees, with baseline configuration.

incidence angle, where the turbulence energy is high on the first blade pressure side, in the first separation region, it is relatively low in the second separation region. This indicates laminar boundary layer separation for the second separation on the blade.

Moreover, at negative incidence, the wake of the first blade encounters the leading edge of the rear blade, creating a peak of turbulent kinetic energy in front of it. However, taking turbulence equations into account, this particular turbulence peak result needs to be nuanced. Indeed, near a stagnation point, as it is the case just in front of the second blade, $k$ and $\nu_T$ tends to grow to excessive values using SST model. Indeed, using linear model of Boussinesq, the turbulent kinetic energy production term $\mathcal{P}$ is defined by

$$\mathcal{P} = 2\nu_T |S|^2, \tag{5.4}$$

with S, the rate of strain $S_{ij} = (\partial_i U_j + \partial_j U_i)/2$ and $\nu_T = C_\mu \overline{u'_i u'_j} T$, the eddy viscosity. This gives rise to excessive levels of production in this region [28][46][29]. Hence, the production exact formulation is

$$\mathcal{P} = -\overline{u'_i u'_j} S_{ij}. \tag{5.5}$$

In front of an obstacle, given the uniform straining flow $U = -Ax$ and $V = Ay$, production becomes $\mathcal{P} = \left(u'^2 - v'^2\right) A$. Using the linear model of Boussinesq gives

$$\mathcal{P} = 4\nu_T A^2 \tag{5.6}$$

in the flow. Therefore, an increase in $A$ will always increases $\mathcal{P}$ with this formula. However, taking the exact formula, if initially $u'^2 < v'^2$, the production should be decreased by straining. Thus, this anomaly of the stagnation point could be explained by this misrepresentation of the anisotropy of normal stresses. What is more, although the turbulent viscosity formula is qualitatively correct, there appears to be a quantitative estimation flaw. Indeed, at large strain

rates, production should grow linearly with $S$ rather than quadratically. A final explanation for this anomaly could be that the rate of energy dissipation no longer keeps up with the rate of production.
However, several improvements to the model have been suggested. Kato and Launder [47] proposed replacing the production term with

$$\mathcal{P} = 2\nu_T |S||\Omega| \tag{5.7}$$

to get around the problem of excessive production. However, this model has a number of disadvantages. It is also possible to replace the production term by $2\nu_T|\Omega|^2$ but this will also introduce drawbacks. Finally, it is also possible to impose a limit on the turbulent viscosity of "realizability" of the form

$$\nu_T = \min\left[C_\mu \frac{k^2}{\varepsilon}, \alpha \frac{k}{S}\right], \tag{5.8}$$

with $\alpha \leq 1/\sqrt{6}$. In SU2, it is possible to modify SST options in order to use one of the two first modifications (`SST_OPTIONS`: `KATO-LAUNDER` or `VORTICITY`). Results of these modifications, still at $\alpha_1 = 36°$, are shown in Appendix A.1 in Figure A.4. As expected, the turbulent kinetic energy peak vanishes using these production modifications and therefore, the initial result might be not fully physical and should not be taken into account in this flow analysis. To be noticed, the inlet turbulent kinetic intensity can be chosen in SU2. For this work, the default value has been used *i.e.* $I = 5\%$. However, the turbulent kinetic energy level rapidly decreases after the domain inlet to zero towards the blade leading edge. This turbulent decay is discussed in Appendix A.3.

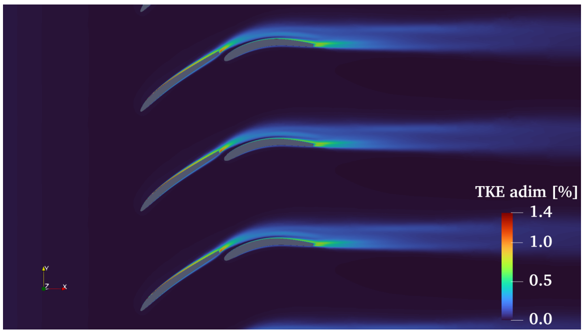

**(a)** $\alpha_1 = 50°$, $i = 0°$.

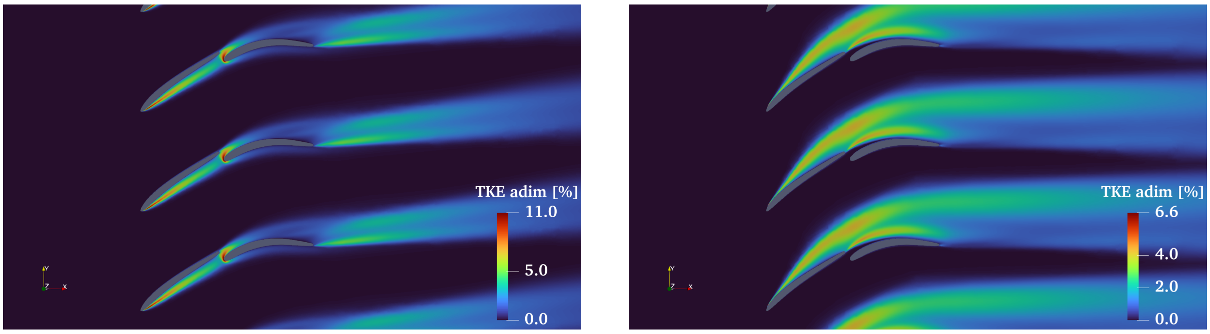

**(b)** $\alpha_1 = 36°$, $i = -14°$. **(c)** $\alpha_1 = 60°$, $i = 10°$.

**FIGURE 5.8:** Turbulence kinetic energy $k$ comparison for inlet flow angle of 36, 50 and 60 degrees, with baseline configuration.

Then, the ratio between turbulent viscosity and laminar viscosity is represented in Figure 5.9. The ratio represents the relative importance of turbulence in the flow compared to the laminar (viscous) effects and therefore gives an idea of the dominant phenomenon in the flow. This also gives a representation of the high diffusion regions in the fluid. Keeping in mind that the simulations use first order upwind scheme, it is interesting to see that the diffusion is much higher at positive incidence and in particular in the center region of the wake of the first blade. The diffusion is negligible for zero incidence configuration and relatively important for negative incidence angle. Finally, the turbulence dissipation rate is represented in Figure 5.10. This highlights the regions of high dissipation of turbulent kinetic energy. It also represents the transfer of energy from large scale to smaller ones, and to thermal energy at the end. The regions of high dissipation corresponds more or less to the regions of high turbulent kinetic energy (Figure 5.8), so that production approximately keeps up with dissipation.

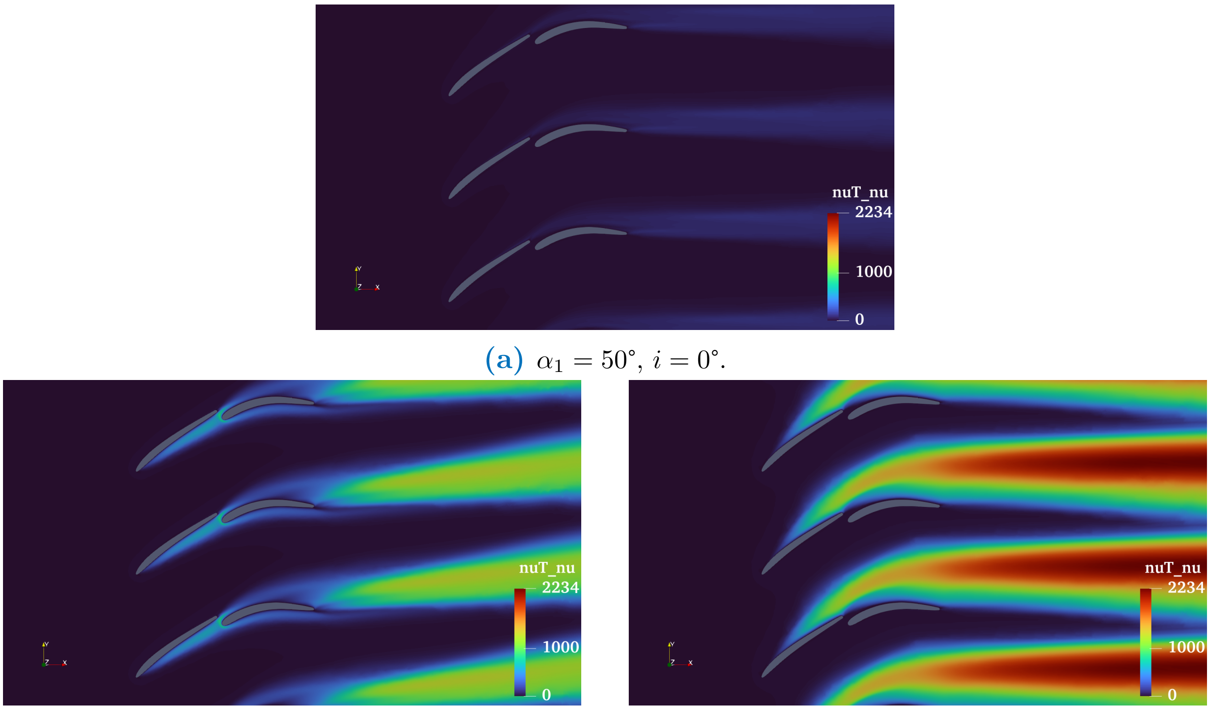

**(a)** $\alpha_1 = 50°$, $i = 0°$.

**(b)** $\alpha_1 = 36°$, $i = -14°$.

**(c)** $\alpha_1 = 60°$, $i = 10°$.

**Figure 5.9:** Turbulent viscosity over laminar viscosity $\nu_T/\nu$ comparison for inlet flow angle of 36, 50 and 60 degrees, with baseline configuration.

### 5.1.5 Blade analysis: Isentropic Mach Number and Skin Friction

Blade analysis gives insights into the loading sharing between the two blades as well as the phenomena occurring in the direct vicinity of the blades with comparison with the reference incidence case. Figure 5.11a represents the isentropic Mach number (see equation (2.8)). The "design-optimal" curve shape is here obtained for zero degree incidence angle. Indeed, the flow is almost parallel to the camber line at the leading edge. The pressure and velocity distribution is smooth and continuous and the main cause of flow deviation is caused by the blade camber. This curve indicates a large blade loading near the front blade leading edge, decreasing towards the trailing edge. At negative incidence angle however, the blue curve indicates that the nominal curve shape is almost inverted. The flow needs to accelerate around the leading edge onto the pressure side and therefore, the Mach distribution swaps and diffusion on the pressure side is highly increased. The blade loading on the pressure side increases in the first part of the blade and then stays constant. On the second blade, $M_{\text{is}}$ is much more higher than for the two other cases but the global shape is almost the same, except for a small plateau towards the trailing edge, which could be a sign of separation. For positive incidence, although the second blade curve

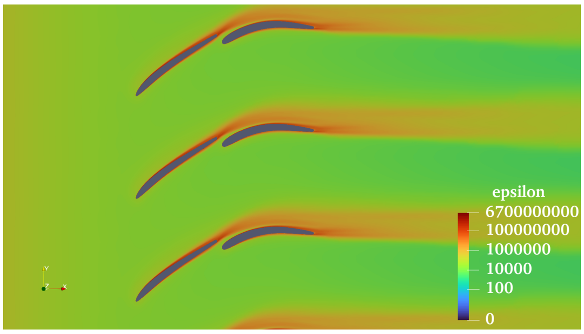

**(a)** $\alpha_1 = 50°$, $i = 0°$.

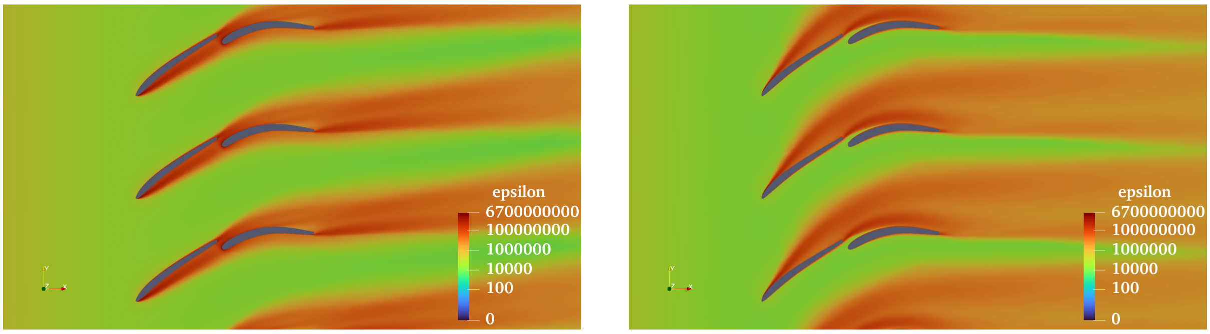

**(b)** $\alpha_1 = 36°$, $i = -14°$.

**(c)** $\alpha_1 = 60°$, $i = 10°$.

**FIGURE 5.10:** Turbulence dissipation rate $\varepsilon$ comparison for inlet flow angle of 36, 50 and 60 degrees, with baseline configuration.

$M_{\text{is}}$ globally seems similar to the "design-optimal" or nominal one, the first curve on suction side begins very high as the flow needs to accelerate around the leading edge but then rapidly decreases to the mainstream values and then flattens instead of continuing to decline. This first acceleration leads to high local diffusion and the peak region is sometimes known as *leading edge spike* and this high diffusion may lead to boundary layer transition and even separation.

Secondly, the skin friction coefficient (see equation (3.26)) is plotted all along the blades for the three different inlet flow angles. Here again, the orange curve is the reference one corresponding to a "good" flow behavior around the blades. The extreme values observed right at the trailing and leading edge of both blades are the results of singular values occurring in very high curvature regions and are not representative of the real flow physic. However, the skin coefficient curves allow to confirm what was already well guessed before: the flow separation. The parts of the figure circled in red correspond to negative skin friction and thus, to flow separation and recirculation. These regions indeed correspond to the ones on the figures here above of the Mach number and total pressure where separation and low-flow regions were spotted. This also shows that the second separation at negative incidence angle is rather mild in comparison with the first one. The first separation, in dashed line, start negative but becomes positive towards the trailing edge, indicating a reattachment of the boundary layer. The green curve on the first blade (positive incidence angle) for the suction side rapidly changes sign and becomes negative over almost its entire length, suggesting a very early separation. Again, these regions refer to high diffusion and rapid growth of the boundary layer resulting in separation.

### 5.1.6 Wake analysis

The total pressure losses generated by the compressor stage are studied by analyzing the tandem's wake. As shown in Figure 5.12, the wake is relatively weak at moderate incidence angles. It consists of a peak in which the respective wakes of the two blades can be guessed from the

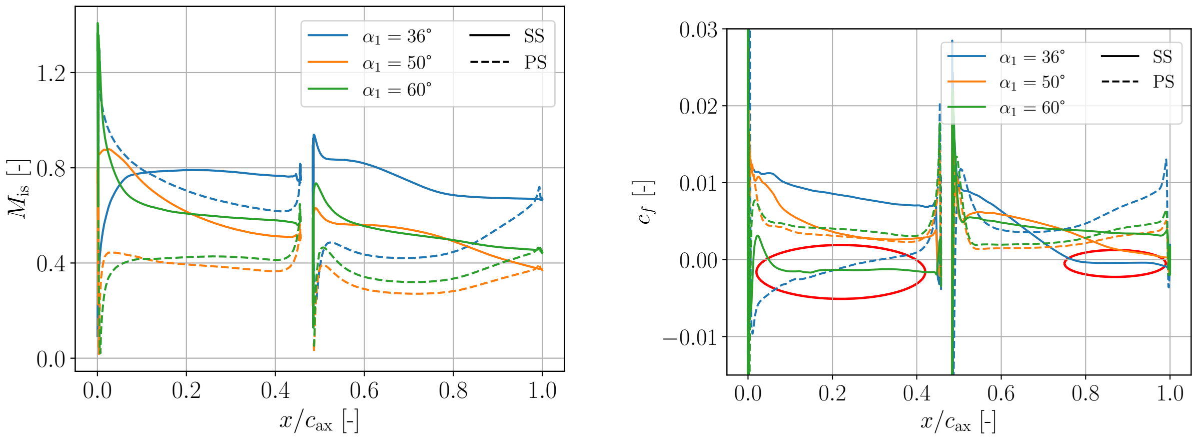

**(a)** Isentropic Mach number around the blades: comparison for inlet flow angle of 36, 50 and 60 degrees, with baseline configuration.

**(b)** Skin friction coefficient around the blades: comparison for inlet flow angle of 36, 50 and 60 degrees, with baseline configuration.

**FIGURE 5.11:** Initial blade analysis comparison.

small bumps. However, as we move away from the reference incidence, the wake becomes wider and losses are higher. At $\alpha_1 = 36°$, the wake remains relatively thin, but the losses within are approximately four time bigger. Conversely, at positive incidence, the wake is much wider, although losses are lower than at negative incidence, spreading over most of the pitch and leaving little room for undisturbed flow to pass through. All in all, losses are higher at high flow angle by integrating over the pitch. It is also interesting to note that the loss maximum tends to shift upwards as incidence increases, indicating once again that the tandem is unable to turn the flow sufficiently to straighten it out.

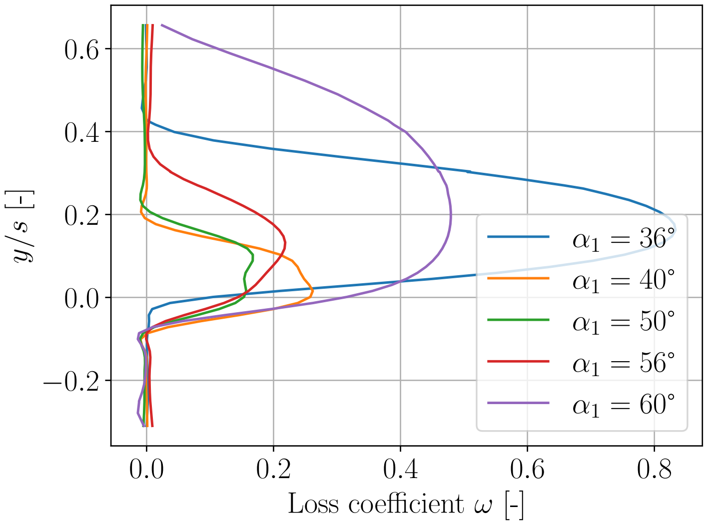

**FIGURE 5.12:** Losses in the wake with baseline configuration.

## 5.2 Front blade rotation around trailing edge

Now that it has been shown that the initial configuration was not optimal for inlet flow angle variations, this and the next sections develop the OGV tandem geometry modifications made to improve compressor stage performance under a range of flow angles. To this end, for each strategy considered, several simulations were carried out for each given inlet flow angle with different geometries to determine which would be the best to minimize losses and increase the pressure ratio. To fully understand the reasons why one geometry is optimal and another is not, a more detailed flow analysis will be carried out each time for a low and a high flow angle. Finally, we will also try to determine the limits of the strategy under consideration and the reasons for these limits.

The first modification taken into account to improve the performance of the compressor stage is to rotate the first blade around a point situated near the trailing edge. Indeed, this kind of geometry modification would almost not change the gap distance between the two blades, avoiding bad phenomena in this region. Moreover, the modification angle range is rather wide since the rotation is not blocked on his way by the other blade. The rotation point is represented in Figure 5.13a and corresponds approximately to the trailing edge curvature center, while a general representation of the front blade rotation is represented in Figure 5.13b. The rear blade remains unchanged.The mesh is adapted to any new configuration.

**(a)** Front blade trailing edge rotation center. **(b)** Front blade rotation around trailing edge.

**FIGURE 5.13:** Front blade rotation schematic.

For every off-design incidence angle, several front blade rotation angles will be investigated, swapping positive and negative blade rotation with respect to the blade position which corresponds to a minimal relative incidence angle (in absolute value *i.e.* $|i| \approx 0$). The rotation angles, or stagger angles, will be referenced to the initial front blade configuration, which will therefore correspond to a zero degree front blade rotation angle, so that the relative rotation angle is given by

$$\chi_{\text{rel}} = \chi'_{FB} - \chi_{FB} \tag{5.9}$$

based on the notation used in Figure 2.11. The inlet flow angle range tested is a little bit wider, from 26 to 64 degrees, than the one used for the initial condition since, as will be seen later, the extreme inlet flow angles behave better once an appropriate front blade rotation is used. In other words, the rotation of the front blade extends the operating range of the tandem. The results of these simulations are shown for some of the flow angles in Figure 5.14. For each case, the tandem configuration shown in the left panel corresponds to the red dot on the loss curve. Recall that this angle corresponds approximately to the angle that minimize the absolute value of the incidence angle. Most of the time, however, this angle is not the one that minimizes the losses. Indeed, it seems that a FB rotation angle a little bit more important diminishes the loss for almost all cases. For some cases, like 30 or 60 degrees, the curves is different because it appeared while making the simulations that these extreme angles necessitated further computations with more FB rotation angles tested for example, or higher FB angles. Moreover, while

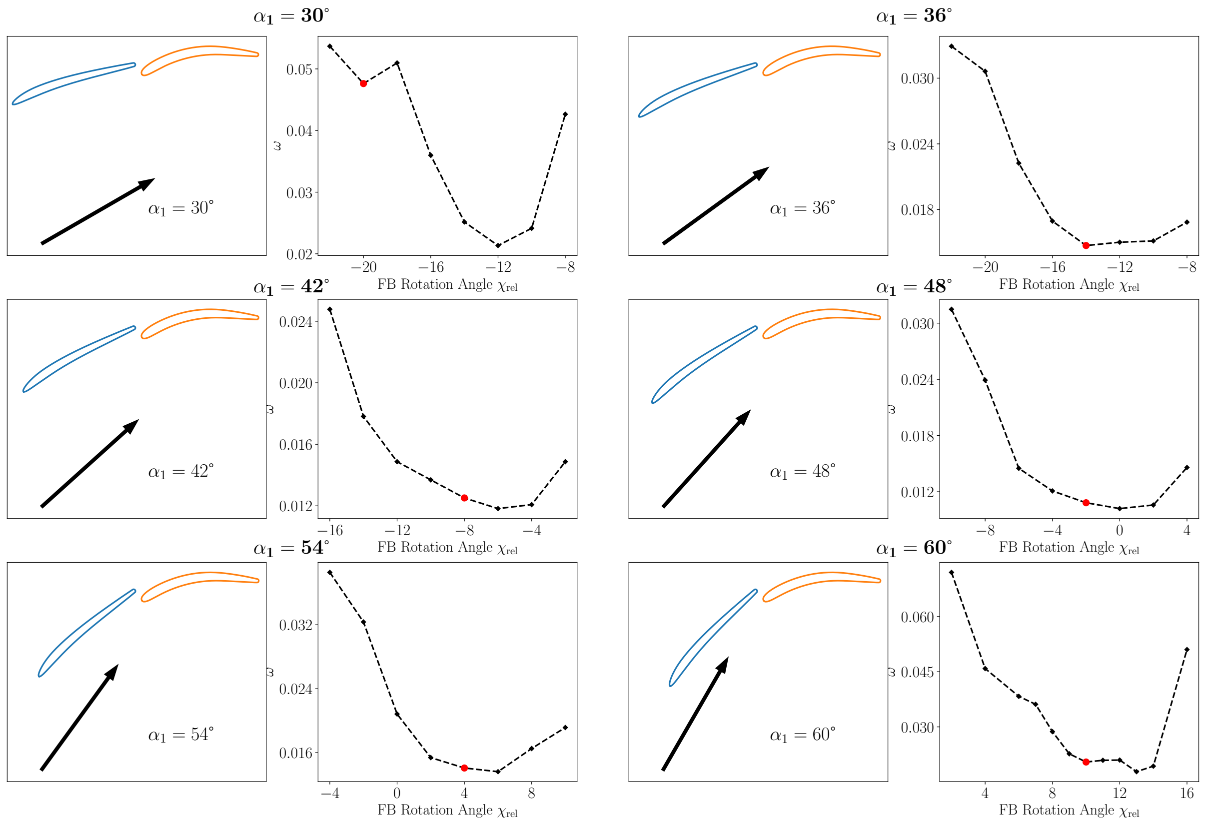

**Figure 5.14:** TE rotation: results of losses with front blade rotation angles for different inlet flow angles.

the loss curve shape is rather smooth for moderate flow angles, its appearance is more irregular for extreme incidence angles, which points to more complex phenomena.

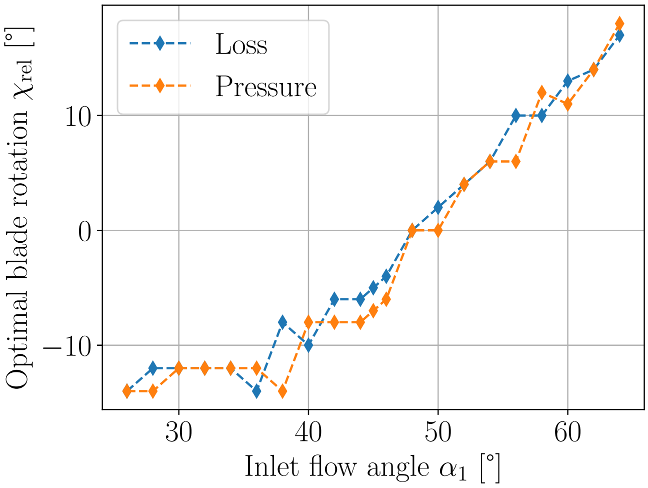

**Figure 5.15:** Optimal trailing edge rotation angle.

Finally, Figure 5.15 shows the optimal angle of rotation of the front blade. It can be seen that, although the curve is not exactly linear, the optimal rotation more or less follows the inlet flow angle, both in terms of losses and pressure ratio. There is also an interesting plateau around $\chi_{\mathrm{rel}} = -12^\circ$ for flow angles of 28 to 36 degrees.

### 5.2.1 Global performances: baseline VS optimized

The results obtained with the front blade rotation show a large improvement of the performances of the compressor stage all over the incidence range. The losses are represented in Figure 5.16a and the pressure ratio in Figure 5.16b. These results only include the minimum loss and maximal pressure ratio obtained with the kind of curves showed here above in Figure 5.14. The losses are well above the initial ones, especially at extreme inlet flow angles, enabling the incidence operating range to be extended. Secondly, the pressure ratio is now almost linear with respect to the inlet flow angle. The TE rotation adjusting strategy allows the incidence operating range to extent to 34.2°, from 27.8° to 62.0°, with a reference inlet flow angle of 44.9°. Hence, an appropriate front blade rotation system around the trailing edge allows to gain 19.5° of incidence range with a lower minimal loss level.

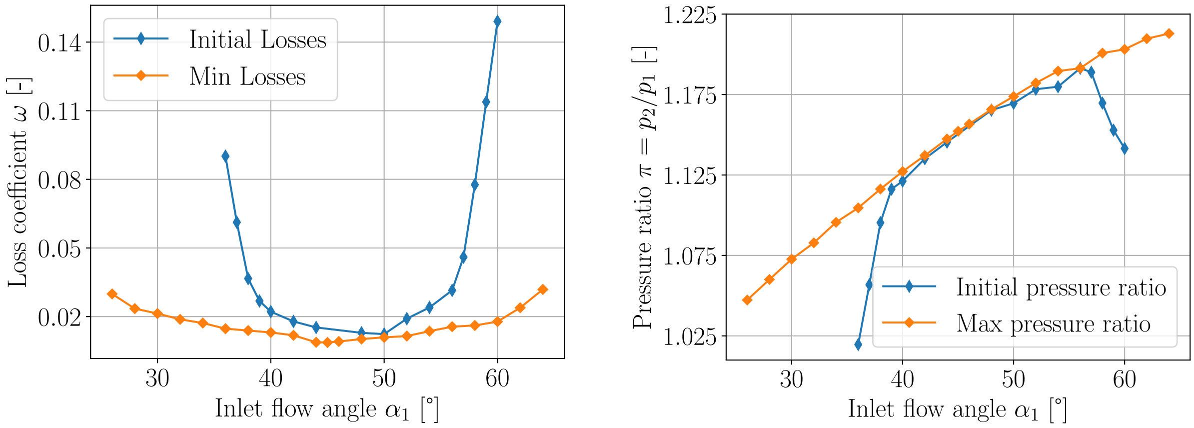

**(a)** Loss coefficient comparison. **(b)** Pressure ration comparison.

**FIGURE 5.16:** TE rotation: comparison between baseline and modified configuration performances.

Table 5.2 shows the performance parameters of the low and high inlet flow angles of the optimized geometries with comparison to the baseline one. As stated before, the loss and pressure coefficients are much better and the diffusion factor also increases, reaching 0.8 for high inlet flow angle. The load split indicates more loading on the second blade for $\alpha_1 = 36°$ and the opposite for $\alpha_1 = 60°$. Nevertheless, the load is relatively well distributed on the two blades. Finally, drag is considerably decreased for both cases. To be noticed, the lift coefficient does not vary much for 60° inlet flow angle with comparison to the nominal one.

**TABLE 5.2:** TE rotation performances parameters.

| Inlet flow angle | $\omega$[%] | $\pi$ | DF | LS | $C_L$ | $C_D$ |
|---|---|---|---|---|---|---|
| Initial 36 | 9.01 | 1.02 | 0.24 | / | 0.18 | 0.06 |
| Optimized 36 | 1.47 | 1.10 | 0.40 | 0.45 | 0.41 | 0.01 |
| Initial 60 | 14.91 | 1.14 | 0.69 | 0.48 | 0.93 | 0.15 |
| Optimized 60 | 2.09 | 1.20 | 0.80 | 0.58 | 0.96 | 0.02 |

### 5.2.2 Flow visualization

In this section, comparison will be made between initial extreme angles flow using unmodified geometry and optimal geometry configurations. As explained before, since the baseline configuration does not allow to go on flow angles outside the range 36° to 60°, the comparison will be made on the angle 36 and 60 degrees. Smalls sections will discussed later on incidence angles out of this range.

### Evolution of the flow along a streamline

The pressure and the flow angle evolutions of both low and high inlet flow angles are represented in Figure 5.17 and 5.18. Firstly, for low angle, it appears that the initial pressure drop in the front blade first half is now almost completely gone, except a small drop in front of the first blade. Instead of that, the pressure increases until the trailing edge, even though this increase flattens near the trailing edge. The rear blade, on the other hand, shows a small decreases of the pressure directly in the leading edge vicinity. However, the second pressure drop initially observed, which takes place halfway down the blade, disappears and the pressure ratio is able to reach 1.1. On the second figure, the flow angle now decreases monotonously over the entire tandem, reaching a value close to zero in the end.

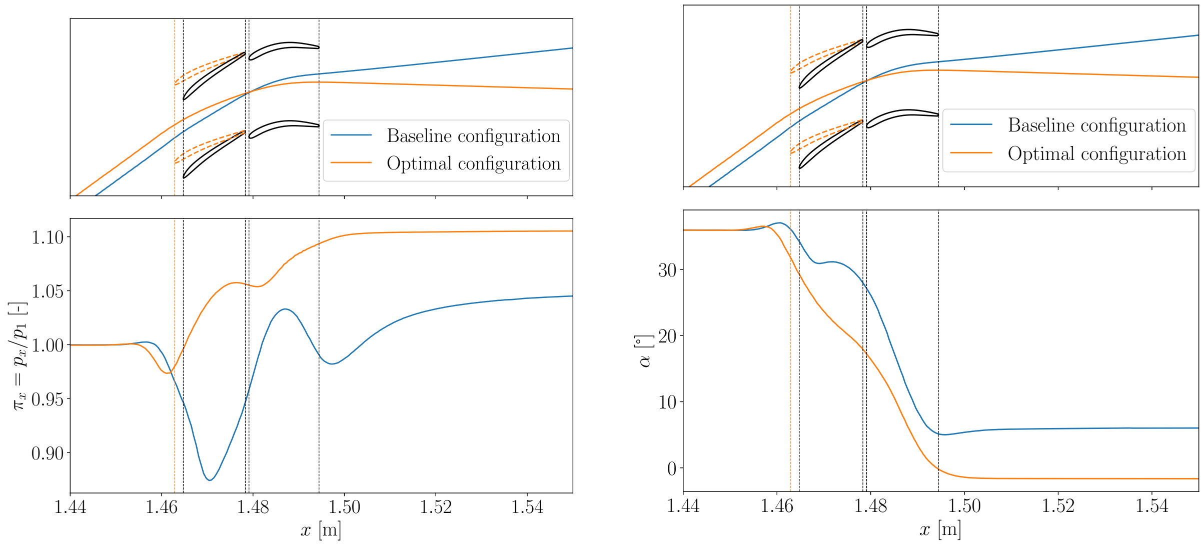

(a) Normalized pressure evolution.

(b) Flow angle evolution.

**Figure 5.17:** TE rotation: evolution of flow quantities along streamlines at 36° incidence angle.

For high flow angles, both pressure and flow angle evolution behaviors keep the same general aspect with comparison to the baseline case. However, the pressure rise is much higher and the little fluctuations in front of the first blade are somehow damped. To be noticed that the pressure rise due to the first blade is much higher that the one due to the second blade, confirmed by the load split result seen above (LS = 0.58). Moreover, the second blade almost plays no role on the pressure increase since the pressure evolution reaches maximum around the second blade half and then flattens out, even decreasing slightly. The flow angle evolution does not show interesting difference with the baseline case, except that the outlet flow angle is slightly more important.

### Mach number

Mach number representations will be discussed here; they are represented in Figure 5.19. Pay attention that here, the figures color scale are adapted to the individual case as it represents best the flow for "good performance" values. Hence, since the modified configuration generally behaves better, the associated flow values are more uniform, without harsh values and therefore,

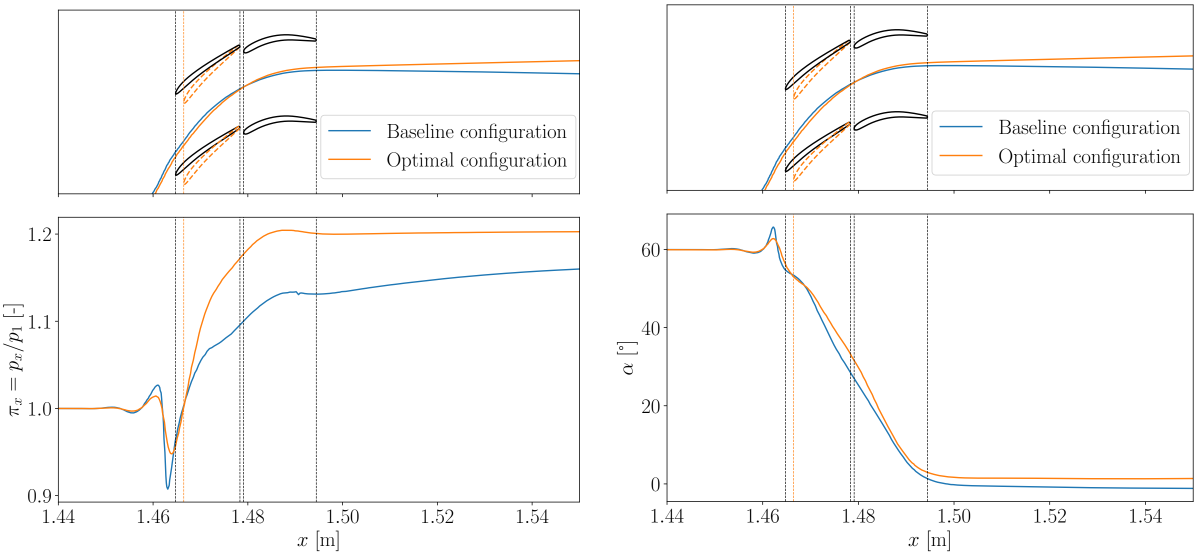

**(a)** Normalized pressure evolution. **(b)** Flow angle evolution.

**Figure 5.18:** TE rotation: evolution of flow quantities along streamlines at 60° incidence angle.

using the same scale for nominal and optimized configurations would reduce understanding and clarity.

Firstly, the large wake regions formed downstream of the blades reduce considerably, replaced by thinner and less severe wakes. Indeed, the flow does not seem to detach and create large recirculation region as was the case for baseline configuration. Moreover, a significant difference of Mach number is visible between upstream and downstream regions, indicating a large deceleration of the flow through the tandem stage.

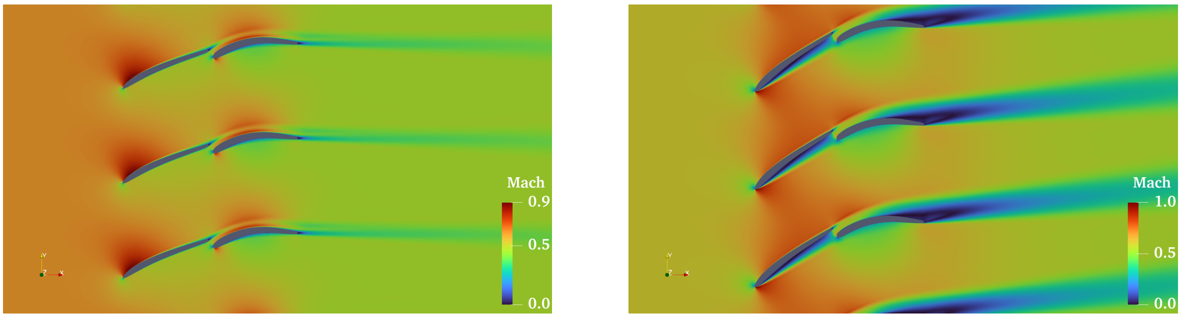

**(a)** Optimized 36°. **(b)** Baseline 36°.

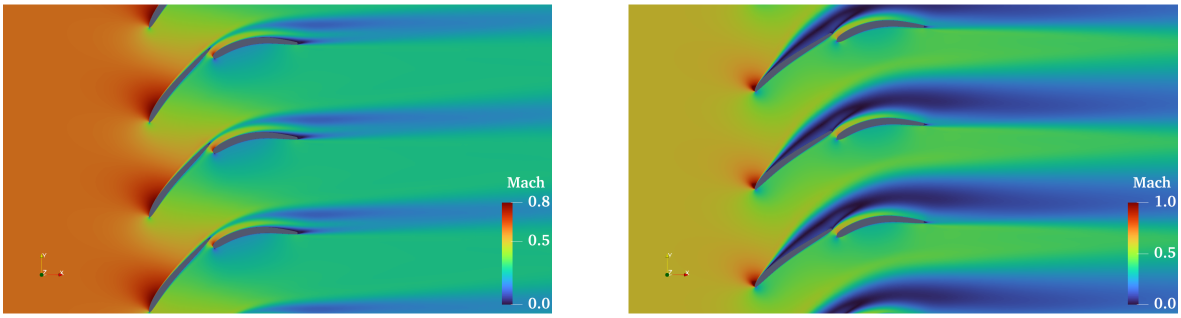

**(c)** Optimized 60°. **(d)** Baseline 60°.

**Figure 5.19:** TE rotation: Mach number comparison for low and high incidence angle between optimized and baseline configuration.

### Total pressure

Figure 5.20 shows the comparison of total pressure between baseline and optimized configurations. Here again, the modified geometries generate less total pressure losses, only suffering of a mild decrease in the wake but this decrease is nothing compared to the initial ones.

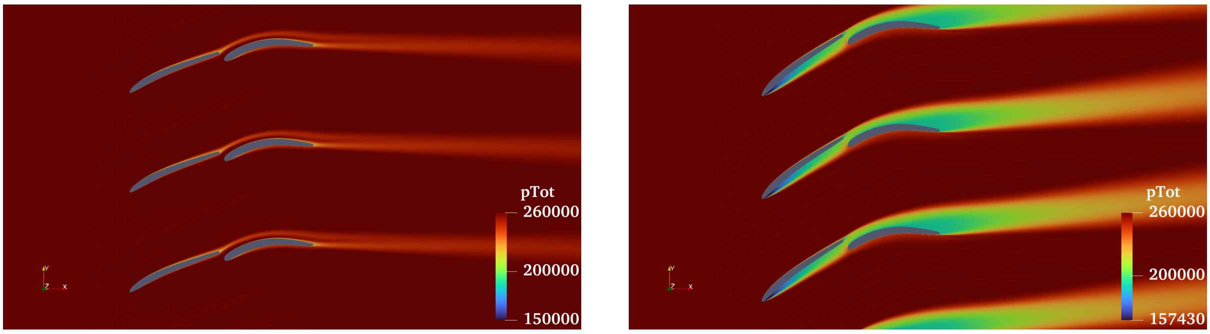

**(a)** Optimized 36°. **(b)** Baseline 36°.

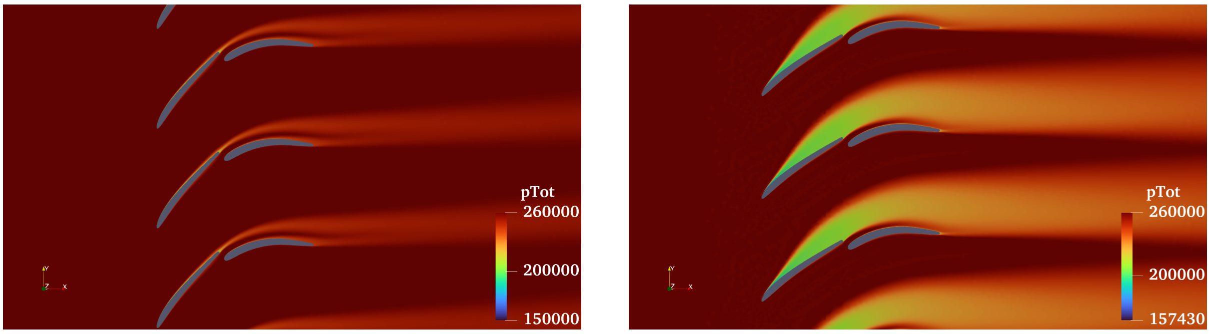

**(c)** Optimized 60°. **(d)** Baseline 60°.

**FIGURE 5.20:** TE rotation: total pressure comparison for low and high inlet flow angles between optimized and baseline configuration.

### Turbulence quantities

The turbulent kinetic energy is represented in Figure 5.21. Keeping in mind that the color scale must be taken individually, the turbulent kinetic energy is almost reduced by a factor 10 in the critical region for both low and high flow angles. However, a small turbulent region develops on the suction side of the rear blade at low flow angle. At high flow angle, the wake width is largely decreased and the boundary layer on the first blade seems to grow but remains attached to the blade. Finally, the ratio between the turbulent and the laminar viscosity is represented in Figure 5.22. At low flow angles, the wake of the second blade exhibits more pronounced turbulent phenomena compared to viscous effects, so that the second blade experiences more diffusion (LS = 0.45). Conversely, at high flow angles, the wake of the first blade demonstrates a greater dominance of turbulent phenomena over viscous effects and more diffusion (LS = 0.58).

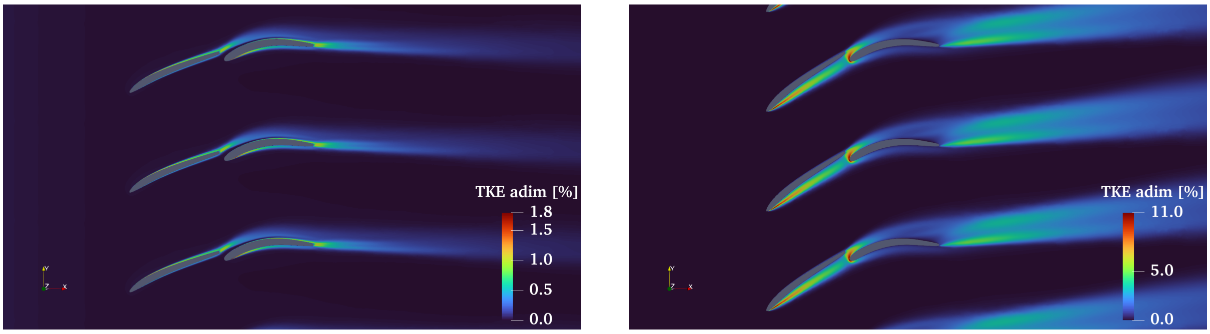

(a) Optimized 36°. (b) Baseline 36°.

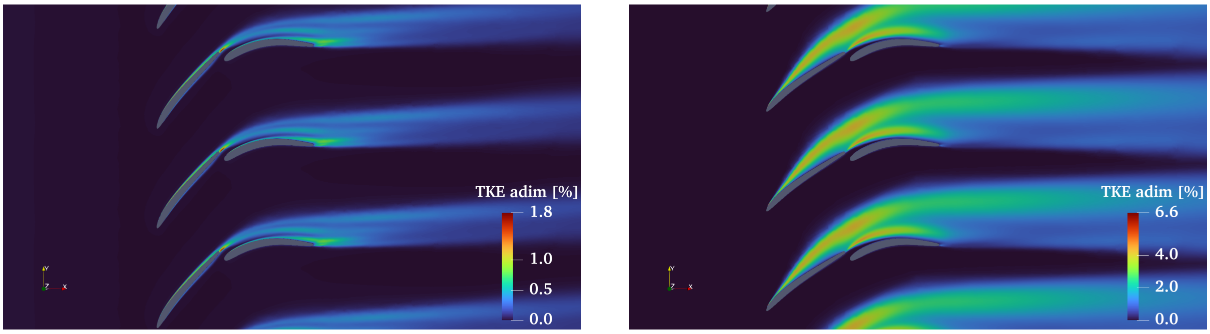

(c) Optimized 60°. (d) Baseline 60°.

**Figure 5.21:** TE rotation: turbulent kinetic energy comparison for low and high inlet flow angle between optimized and baseline configuration.

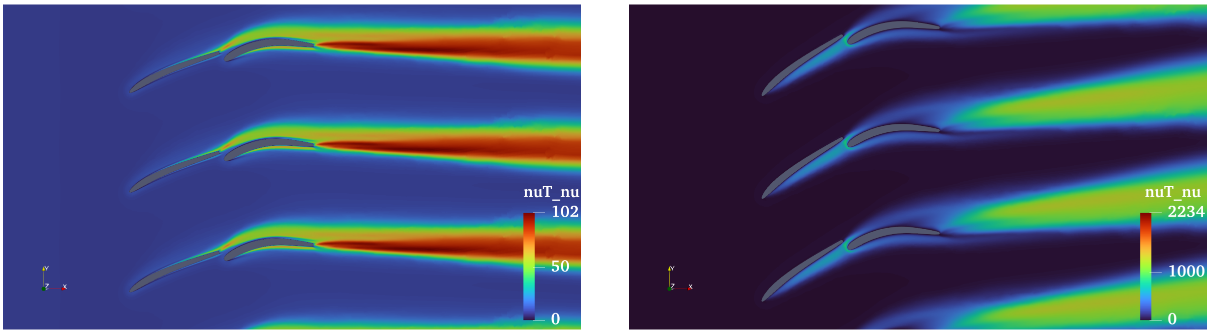

(a) Optimized 36°. (b) Baseline 36°.

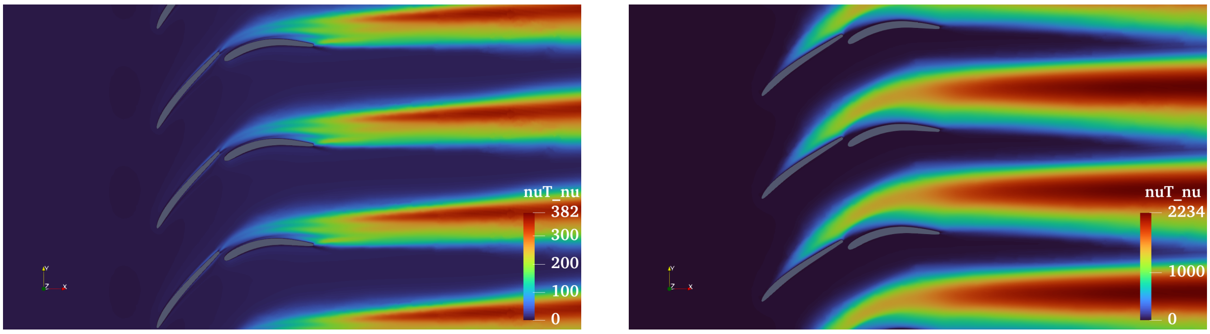

(c) Optimized 60°. (d) Baseline 60°.

**Figure 5.22:** TE rotation: turbulent viscosity over laminar viscosity comparison for low and high inlet flow angle between optimized and baseline configuration.

### Blade analysis

Figure 5.23 represents the blade analysis of low flow angle optimized configuration. With the modified configuration, the $M_{\text{is}}$ (eq. (2.8)) curves on the first blade, in Figure 5.23a, take a more design kind of shape, undergoing important loading near the leading edge, and decreasing smoothly towards the trailing edge. The second blade, on the other hand, presents a different behavior. The isentropic Mach number on the suction side starts to increase, being much lower than for the baseline configuration, then reaches a maximum and finally decreases. This could be explained because the incoming flow from the first blade is coming almost horizontally, and stumbles on the suction side of the second blade because of its curvature. This slows down the flow, which afterwards re-accelerates. This blade loading mismatching is then not beneficial and the latter should be better distributed over the two blades. The skin friction curves, in Figure 5.23b, show that the negative skin friction values, corresponding to separation region, are now gone, except at the very beginning of the second blade, to be linked with the small turbulent region on the pressure side discussed here above. This result is explained as the very low flow angle of the incoming flow can not follow the blade surface, its curvature being too severe. For the high inlet flow angle, isentropic Mach number and skin coefficient around the blades are represented in Figure 5.24. Firstly, for the isentropic Mach number, the plateau that was previously observed on the front blade second half disappeared, and the Mach number smoothly decreases, indicating a high loading on the suction side of the first part of the blade. The second blade $M_{\mathrm{is}}$ curve is similar to the one for the baseline case, albeit slightly lower. The skin friction curve on the first blade is entirely positive, showing a clear improvement with respect to the initial case. Indeed, the flow now remains attached to the blades throughout the tandem stage.

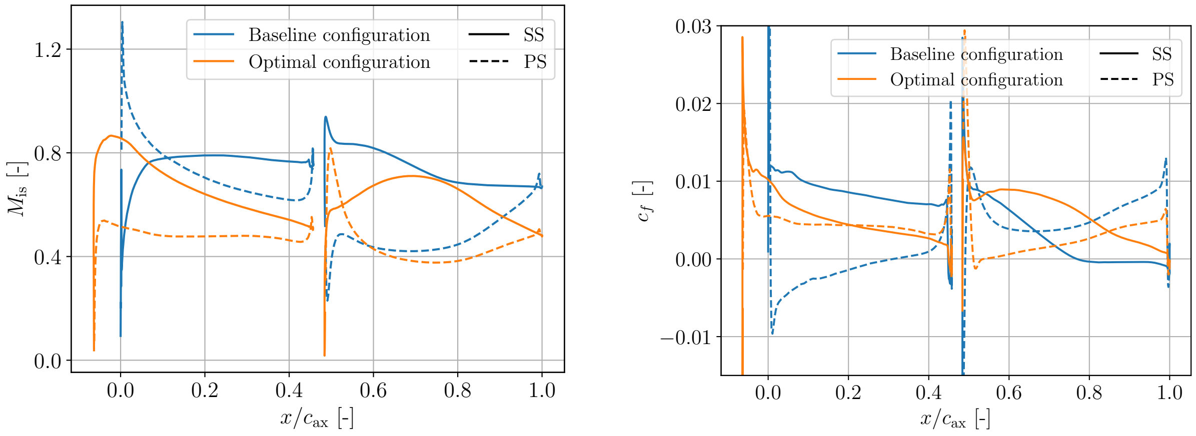

**(a)** Isentropic Mach number comparison.

**(b)** Skin friction coefficient comparison.

**Figure 5.23:** TE rotation: blade analysis comparison between baseline and optimized configuration at 36° inlet flow angle.

### 5.2.3 Wake analysis

In this section, the loss coefficient in the wake is analyzed and shown in Figure 5.25 along the pitch. In Figure 5.25a, for low flow angle, losses in the wake are considerably reduced. Moreover, the wake location is now directly downstream of the second blade whereas it was a little higher in the fluid for the initial configuration. For high flow angle wake, represented in Figure 5.25b, the losses are also greatly reduced but the peak of loss remains at the same position. However, above this peak, the losses drop immediately, indicating a much thinner wake.

### 5.2.4 Very low flow angles

Now that the range of good performances has been analyzed, a special study is carried out on extreme inlet flow angles to try and understand why the strategy is not applicable for angles

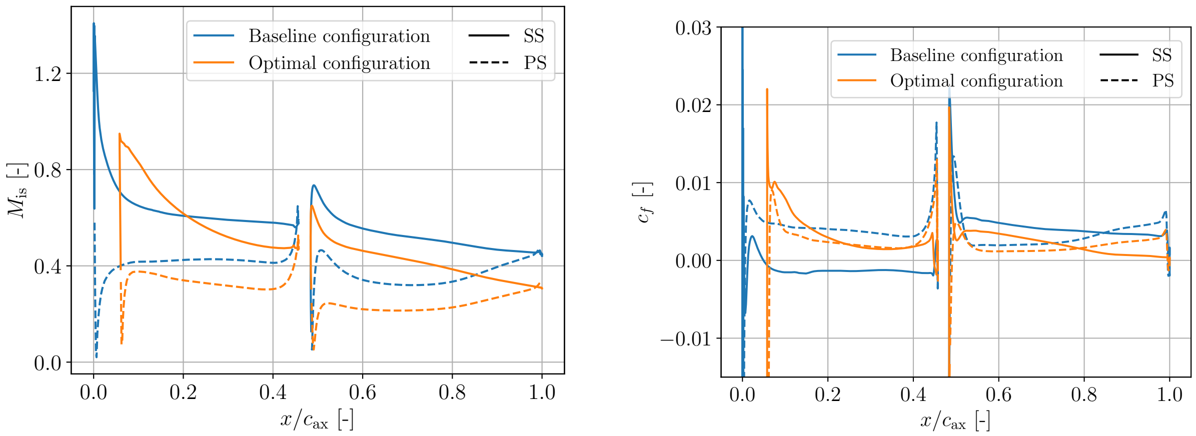

**(a)** Isentropic Mach number comparison. **(b)** Skin friction coefficient comparison.

**Figure 5.24:** TE rotation: blade analysis comparison between baseline and optimized configuration at 60° incidence angle.

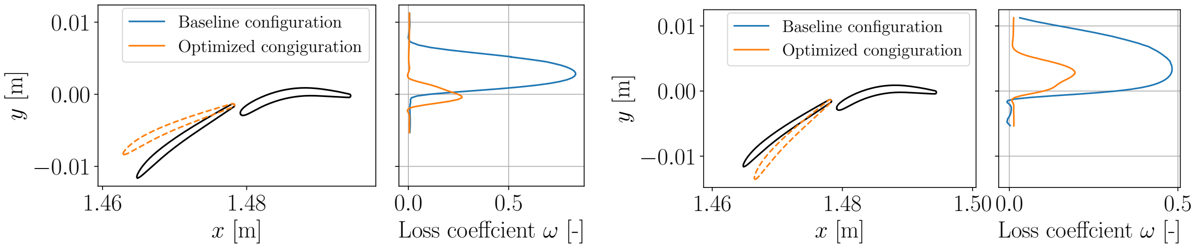

**(a)** Losses in the wake for low inlet flow angle, comparison between baseline and optimized configuration. **(b)** Losses in the wake for high inlet flow angle, comparison between baseline and optimized configuration.

**Figure 5.25:** TE rotation: Wake analysis and comparison for low and high flow angles.

as low/high as we would like. This section and the next will therefore attempt to understand what phenomena develop and in what way they are limiting. In this way, we may find possible solutions to further improve tandem performances and extend the incidence range.

Figure 5.26 represents the flow for a very low flow angle with a highly negative front blade rotation angle. These figures show why it not possible to go as far as wanted in the low flow angles. Indeed, the front blade rotation corresponding to these angles in order to make the flow direction tangent to the blade no longer ensures a sufficient incidence angle on the second blade. Therefore, the flow can no longer stick to the suction side of the rear blade. A large turbulent boundary layer develops on the pressure side of the second blade, generating total pressure losses, virtually increasing the second blade width and thus the drag generated. In the end, even if the flow on the first blade behaves well, the flow direction induced by this first blade is not adapted to the second blade curvature and detaches from the pressure side, which creates a increase of the losses.

### 5.2.5 Very high flow angles

High inlet flow angles necessitate high front blade rotation to ensure the flow to stick to the front blade suction side. However, as represented in Figure 5.27, such high front blade rotation are no longer adapted to the second static blade. The flow angle is still so high at the end of the first blade that it can not attach to the second blade, creating the high turbulent patterns observed.

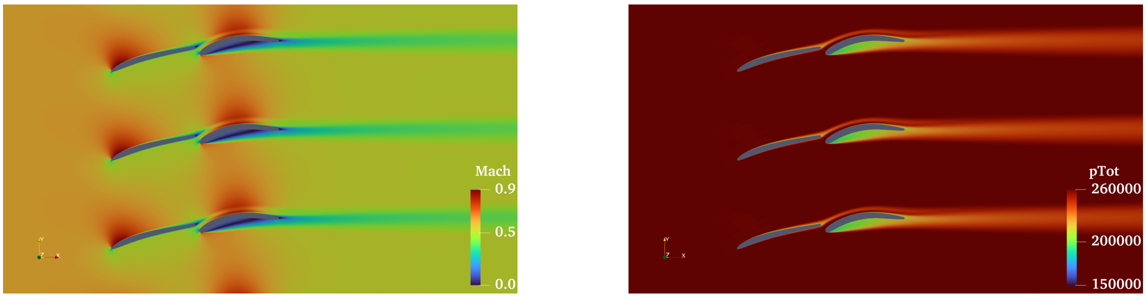

(a) Mach number. (b) Total pressure.

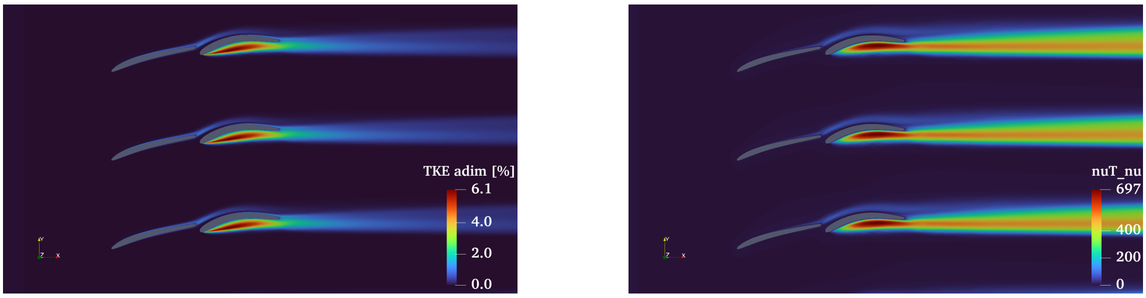

(c) Turbulent kinetic energy. (d) Turbulent viscosity over laminar viscosity.

**Figure 5.26:** TE rotation: flow representation at very low inlet flow angle (30°) and high negative front blade rotation.

In addition to creating large losses in total pressure, these turbulence patterns oscillate in time, making the solution unsteady, which complicates the analysis of the results. Indeed, for a better understanding of this result, an unsteady RANS analysis would be required, which is beyond the scope of this work. Fortunately, this type of solution was only encountered for a 20° rotation of the front blade, which represents the most extreme case tested, with very high losses and therefore far from the optimum configuration sought.

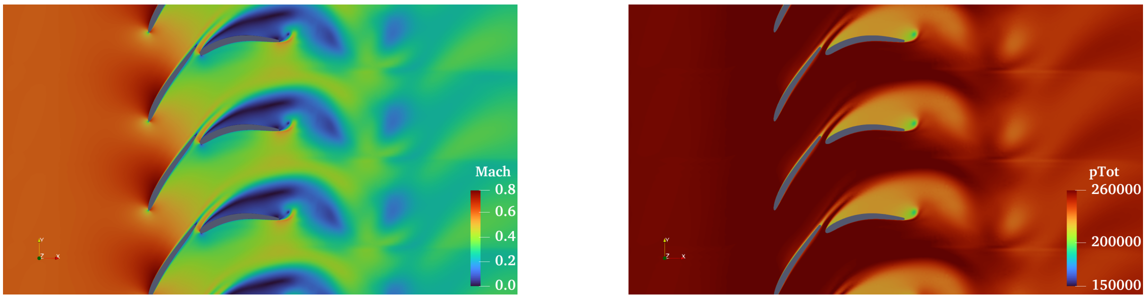

(a) Mach number. (b) Total pressure.

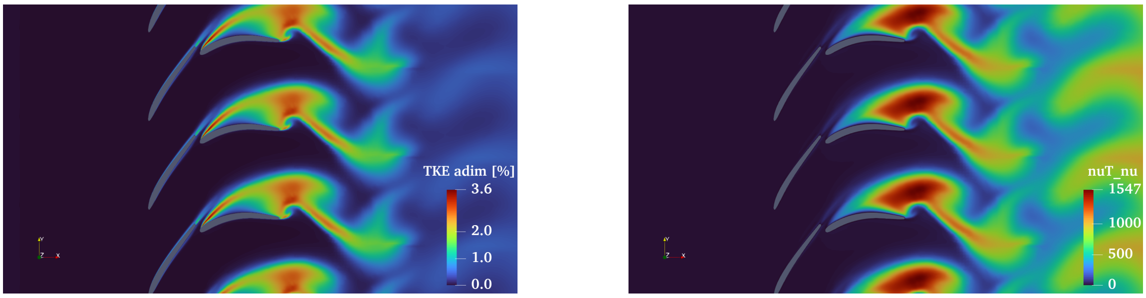

(c) Turbulent kinetic energy. (d) Turbulent viscosity over laminar viscosity.

**Figure 5.27:** TE rotation: flow representation at very high inlet flow angle (64°) and high positive front blade rotation.

## 5.3 Rotation around the mean chord midpoint

Although the performances of the trailing edge rotation strategy are very good, this rotation point presents a serious drawback from a technological point of view. Indeed, the manufacture of this kind of adjusting scheme would be very difficult as the rotation axis should be attached to the blade in a location that could be tricky, the rotation point being located at a very narrow location of the blade. Moreover, the adjusting system would have to apply a important torque to maintain the blade still against the forces applied by the fluid[1] on the blade as the rotation point is off-centered. Therefore, different strategies are investigated to increase the OGV performances while keeping adjusting system feasible. This section focuses on the tandem front blade rotation around the midpoint of its mean chord. In fact, this point offers *a priori* a good compromise between aerodynamic performances and design feasibility. However, unlike the first strategy, the gap does not remain constant.

The midpoint of the mean chord is computed from the mean chord coordinates as follows. Firstly, the cumulative mean chord length is computed along itself by adding the distance between the consecutive points

$$\tilde{c}_{i+1} = c_i + \sqrt{(x_{i+1} - x_i)^2 + (y_{i+1} - y_i)^2}, \tag{5.10}$$

with $\tilde{c}_0 = 0$. Finding the value of the mean chord halfway by $\tilde{c}_n/2$, the indices of $\tilde{c}_i$ corresponding to the values surrounding this mid distance are used to interpolate and find the rotation point. Let $i^*$ and $i^*+1$ be the indices of the points on either side of the mean half-chord length, so the coordinates of the center of rotation are given by

$$x_{rot} = x_{i^*} + \frac{x_{i^*+1} - x_{i^*}}{\tilde{c}_{i^*+1} - \tilde{c}_{i^*}}(\tilde{c}_n/2 - \tilde{c}_{i^*}), \tag{5.11}$$

$$y_{rot} = y_{i^*} + \frac{y_{i^*+1} - y_{i^*}}{\tilde{c}_{i^*+1} - \tilde{c}_{i^*}}(\tilde{c}_n/2 - \tilde{c}_{i^*}). \tag{5.12}$$

The use of this rotation point introduces meshing problems. Rotating the first blade around its mid chord point leads to degenerate configurations with the gap extremely small. The analysis of these positions poses serious issues with the grid generation process and its overall quality. Indeed, as shown in Figure A.7a, the initial mesh, albeit adapting to the blade rotation, do not provide an acceptable meshing refinement in the gap. In fact, for rotation angles around -10 degrees, the blade edges become really close and the boundary layer mesh regions overlap, creating very bad quality mesh. To overcome this problem, a special gap treatment is made exclusively in the gap region, improving the mesh refinement, as shown in Figure A.7b. Nevertheless, it is important to keep in mind that some complex phenomena may happen in this thin region. Moreover, very negative rotation angles lead to bad tandem general shape as the angle between the leading edge of the second blade and the trailing edge of the front blade increases, making the flow coming from the front blade with a negative angle to "crush" on the second blade, leading to separation on the pressure side of the second blade. A schematic representation of the blade rotation is shown in Figure 5.28. At rotation angles around -10 degrees, the tandem blades align and the overall stage becomes similar to a single blade stage.

### 5.3.1 Global performances : baseline VS modified geometry

Figure 5.29a and 5.29b represent global performances of the mean chord midpoint rotation. The incidence angle range is now 30.7° and the reference inlet flow angle is 42.5°. It appears that

---

[1] Based on baseline nominal configuration lift and drag coefficients and mean flow values,

$$L \approx 2 \times 10^4 \text{ N}, \qquad D \approx 3 \times 10^2 \text{ N}.$$

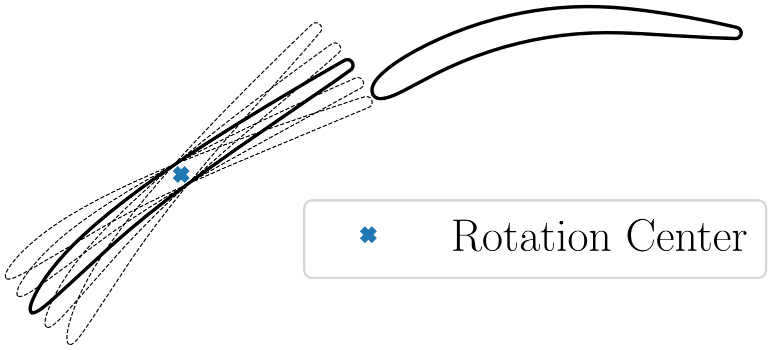

**Figure 5.28:** Front blade rotation around chord mid-point.

this adjusting strategy is very beneficial for both loss reduction and pressure ration increase. Figure 5.30 shows the optimal rotation angles for each inlet flow angle, from the point of view of losses and the pressure ratios. Although the general behavior shows an increase of the blade rotation with the flow angle for both loss and pressure optimization, it can be seen that this evolution is not linear, and some regions even show an unexpected attitude, with the optimum angle decreasing as incidence increases. The pressure and loss curves qualitatively mimic each other, proving that in most cases, loss reduction and pressure gain go hand in hand, albeit this is less the case at low flow angles. An interesting plateau is also observed around 45°: it seems that a blade rotation of -2° is advantageous for both losses and pressure ratios. At low flow angles, once past the plateau at around $\chi_{\text{rel}} = -2°$, the optimum angle drops directly to around -12°. This is interesting, as this angle of rotation is a bit unusual. In this configuration, the two blades are aligned and form a single blade (except for the small gap between them). It therefore appears that, at low inlet flow angles, the advantage of a variable tandem blade diminishes in favor of a fixed single blade. For the sake of clarity, the investigation on low and high inlet flow angles will be separated in this section since very different phenomena seem to characterize them.

Table 5.3 presents the performances of the midpoint rotation strategy. Here again the performances are improved greatly for both low and high inlet flow angles. For $\alpha_1 = 36°$, it interesting to note that the load split is only of 0.26. This means that the first blade plays only a very limited role in the work done by the compressor stage. As a result, most of the flow deflection takes place on the second blade, thanks in particular to its curvature. We can also see that drag is reduced by a factor of 6. As we will see later, this is due to the fact that the entire configuration behaves like a single blade, creating a single zone of losses downstream. At high flow angles, on the other hand, the load split indicates that the first blade provides more work on the flow. However, the lift coefficient decreases slightly compared to the initial configuration. This is because, being parallel to the first blade, the flow produces less lift on it. The drag coefficient is also greatly reduced, by a factor of 5.

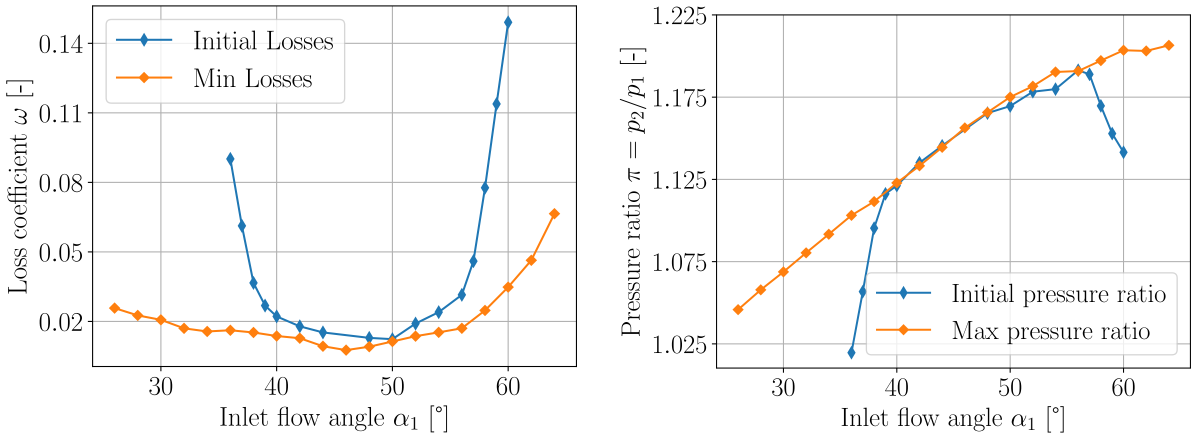

**(a)** Loss coefficient comparison.

**(b)** Pressure ratio comparison.

**FIGURE 5.29:** Mid rotation: performances comparison between baseline and optimized configuration.

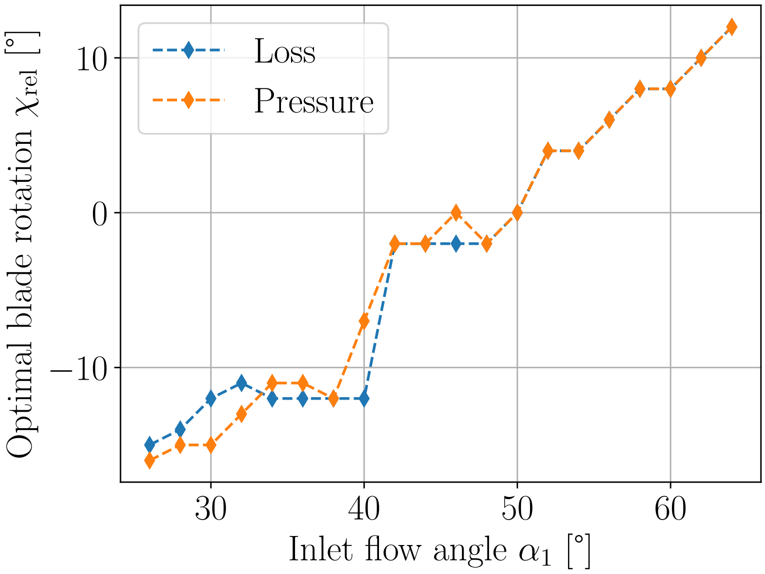

**FIGURE 5.30:** Optimal midpoint rotation angle.

**Table 5.3:** Mid rotation performances parameters.

| Inlet flow angle | $\omega[\%]$ | $\pi$ | DF | LS | $C_L$ | $C_D$ |
|---|---|---|---|---|---|---|
| Initial 36 | 9.01 | 1.02 | 0.24 | / | 0.18 | 0.06 |
| Optimized 36 | 1.61 | 1.10 | 0.39 | 0.26 | 0.33 | 0.01 |
| Initial 60 | 14.91 | 1.14 | 0.69 | 0.48 | 0.93 | 0.15 |
| Optimized 60 | 3.48 | 1.20 | 0.79 | 0.58 | 0.91 | 0.03 |

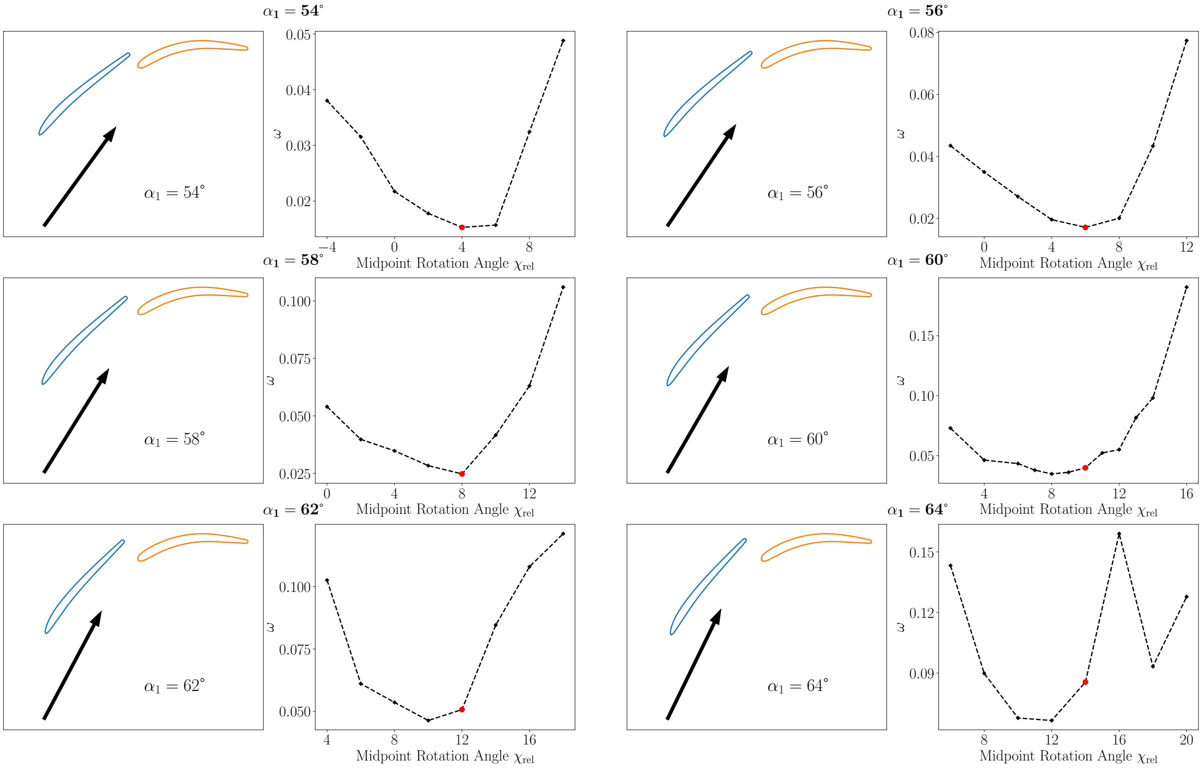

**Figure 5.31:** Mid rotation: results of losses with front blade rotation angles for different high inlet flow angles.

### 5.3.2 High flow angles

For high flow angles, which from an engineering point of view is the most valuable and interesting operating range part (high pressure ratio, low flow coefficient and close to surge), the simulation tests around the reference rotation, which still refers to the rotation which minimize the relative incidence angle $i$ absolute value, are represented in Figure 5.31. Again, the red dot in the left panel figures corresponds to the reference angle. It is interesting to note that the optimal angle are often close to the reference ones, except at very high flow angles. Indeed, it seems that the gap become too large and this does not provide good performances anymore. Moreover, for $\alpha_1 = 64°$, the losses drop after 16° degrees of rotation, which does not make sense. Indeed, in this region, the solution becomes unsteady and a different analysis would be necessary. For this reason, the highest position investigated is 64°.

Pressure and flow angles evolutions along streamlines are respectively represented in Figure 5.32a and 5.32b. Even though the flow angle evolution is relatively similar for both cases albeit slightly higher at the outlet for the modified configuration, the pressure ratio is significantly improved on the first blade for the adjusted case. Indeed, the second part of the first blade now corresponds to an important pressure rise where the flow initially separated from the blade. However, at the

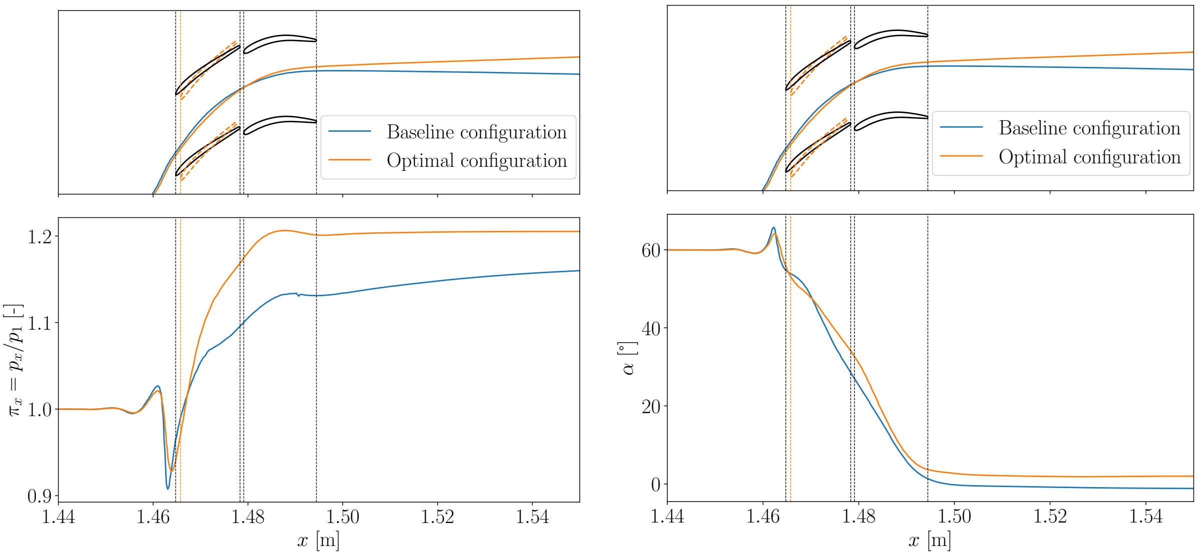

**(a)** Pressure evolution. **(b)** Flow angle evolution.

**Figure 5.32:** Mid rotation: evolution of flow quantities along a streamline at high inlet flow angles.

end of the second blade, the pressure decreases a little bit.

### Flow visualization

As the analysis approach is similar to the previous adjustment strategy, only the Mach number and turbulent kinetic energy are represented here in Figure 5.33a and 5.33b to be compared to Figure 5.6 and 5.8, the rest being included in Appendix A.1 in Figure A.8. The flow does not seem to detach anymore from the first blade surface and the wake region is significantly thinner and less harsh. However, near the second blade trailing edge, a low Mach zone with high turbulent kinetic energy is observed. It seems that the incoming flow can not stick to the end of the rear blade and separates, which may explain the slight outlet angle difference observed in Figure 5.32b as well as the mild pressure drop at the end of the second blade observed in Figure 5.32a.

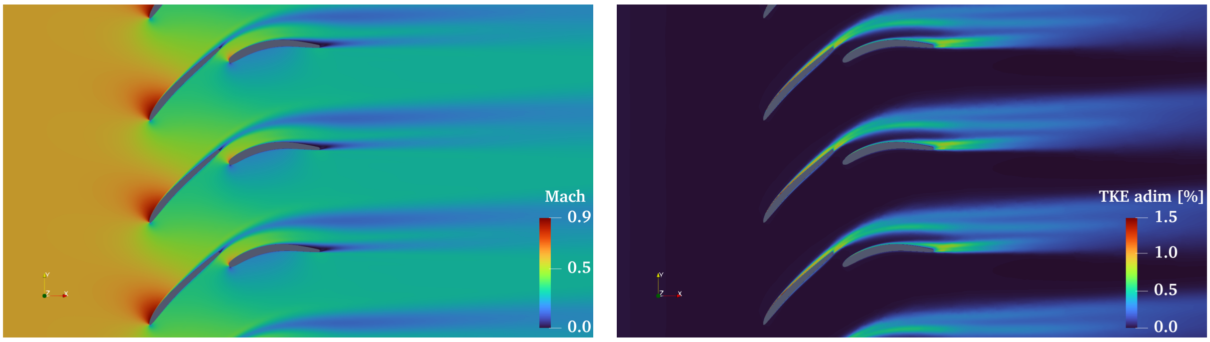

**(a)** Mach number **(b)** Turbulent kinetic energy $k$.

**Figure 5.33:** Mid rotation: flow visualization at high inlet flow angle.

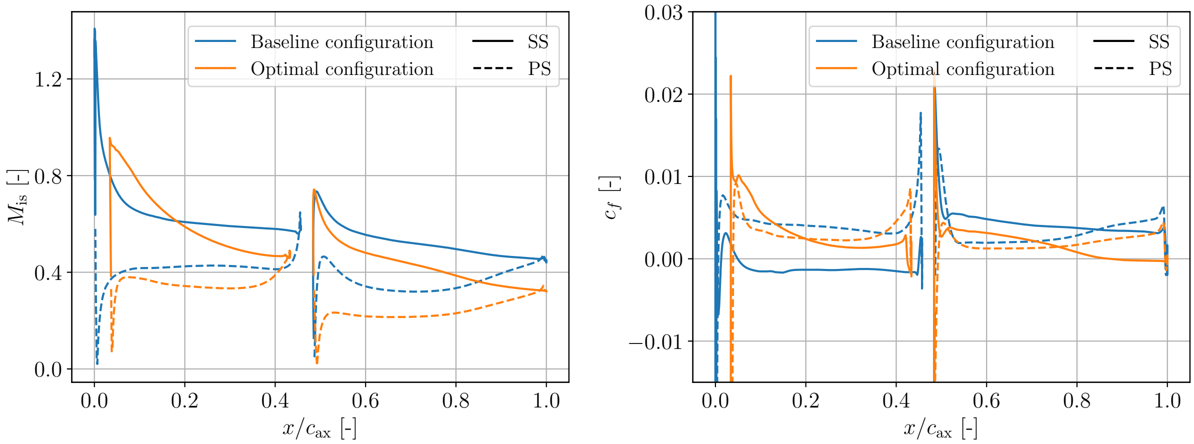

**(a)** Isentropic mach number. **(b)** Skin friction coefficient.

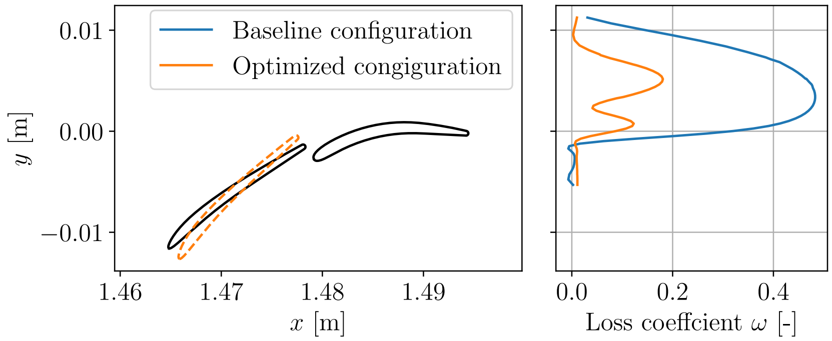

**(c)** Wake analysis.

**FIGURE 5.34:** Mid rotation: high inlet flow angle blade and wake analysis.

### Blade analysis and wake

The blade loading, represented in Figure 5.34a, shows larger blade load on the front blade first part, approaching $M_{\mathrm{is}} = 1$ at the very beginning. while the second blade is less loaded. This explains the high pressure rise observed in Figure 5.32a and confirms that the second blade does not affect the pressure rise that much. The skin friction coefficient indicates that the flow no longer separate from the front blade. On the second blade, however, it is bordering on zero towards the trailing edge, even being slightly negative. This skin friction change of sign indicates separation, which confirms what was just guessed from the flow visualizations. Finally, the wake analysis reveals that the initial wide wakes divides now into two different smaller wakes, whose sum is far less than the initial one. Moreover, the first blade wake is more important than the second one. Indeed, as the second blade applies less deviation on flow (LS = 0.58), it is logical that the associated losses are lower.

## 5.3.3 Low inlet flow angles

At low inlet flow angles, optimal blade angle makes the tandem configuration look like a unique and continuous blade. However, as the front blade angle vary around $\chi_{\mathrm{rel}} = -10°$, some phenomena modify the overall performances and will be discussed in this section. Several low flow angles simulations results are represented in Figure 5.35. At first sight, results may seem spurious and inaccurate due to discontinuities in the overall shape of the curves. Indeed, unlike the high flow angles curves which behave relatively smoothly, with typical parabolic shape around the optimal angle, the curves are sawtooth-shaped, and there does not seem to be a configuration that automatically leads to optimal results *a priori*. However, a closer look reveals similarities

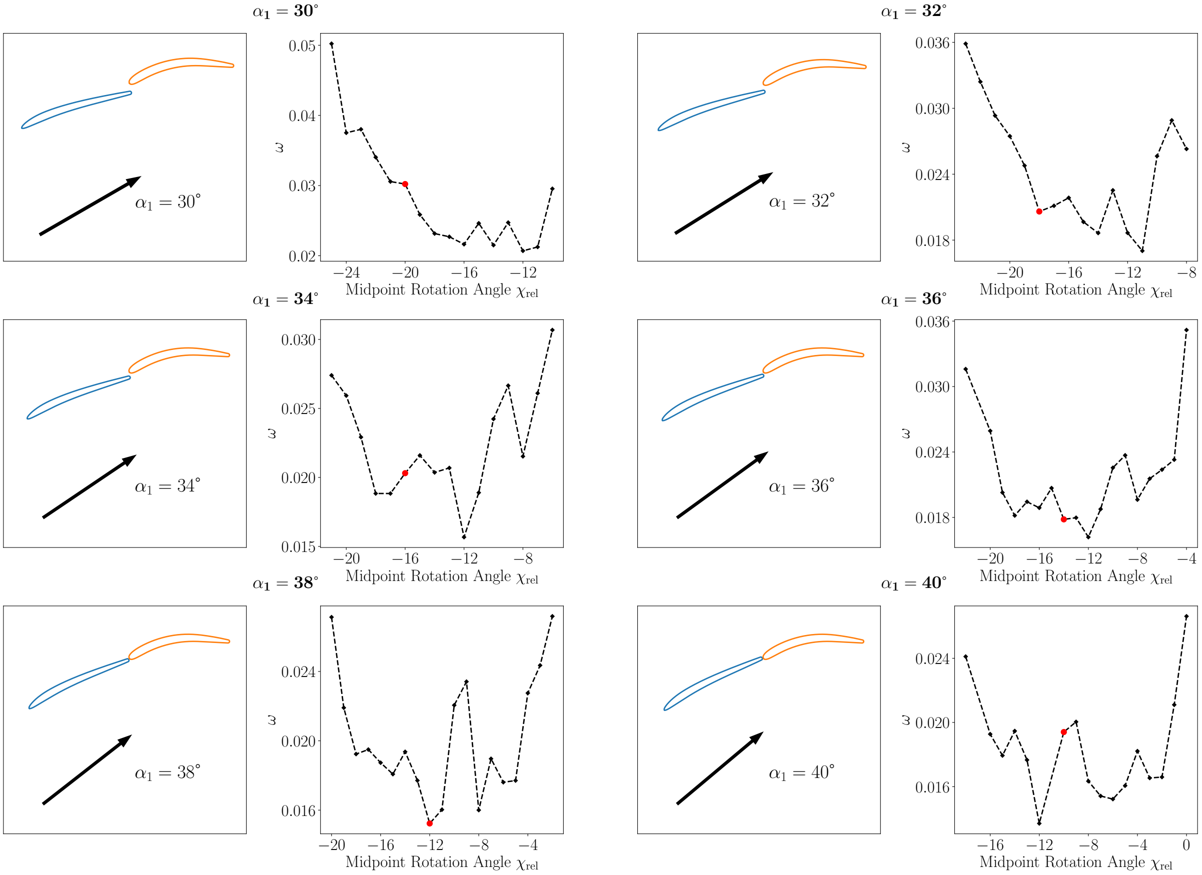

**Figure 5.35:** Mid rotation: results of losses with front blade rotation angles for different low inlet flow angles.

between some of the results. For example, a peak in losses is observed between $\chi_{\text{rel}} = -12°$ and -8° for flow angles from 32 to 40°. Generally speaking, the oscillations observed at certain angles of rotation are repeated at all flow angles, showing a convergence of results, synonymous with real phenomena in the flow. Despite these particular results, Figure 5.29a, 5.29b and 5.30 still show relatively smooth performances behavior. Therefore, it seems that midpoint rotation adjustment works correctly for low flow angles but necessitates more attention in the stagger angle choice since a tiny angle difference may lead to a doubling of losses, as can be seen for example at $\alpha_1 = 38°$ between the optimal blade rotation of -8° and a rotation of -9°. At very low flow angle, the reference angle does not seem ideal and some less negatively rotated configurations provide better results. The first blade being too horizontal, the flow can no longer stick to the pressure side of the second blade, which explains why higher stagger angles are more beneficial. In Figure 5.36a, it can be seen that the pressure no more drops at the front blade leading edge but near the blade gap, the pressure stops rising, where it was highly increasing in the baseline configuration. This means that, even if the first blade is better adapted to the flow angle, the gap region is not optimized, and was actually better for the baseline configuration. Finally, as the separation has been eliminated on the second blade, the pressure increases again, resulting in a higher outlet pressure, while the outlet flow angle is close to zero (see Figure 5.36b).

### Flow visualization

As the analysis approach is similar to the previous adjustment strategy, only the Mach number and turbulent kinetic energy are represented here in Figure 5.37a and 5.37b to be compared to Figure 5.6 and 5.8, the rest being included in Appendix A.1 in Figure A.9. It appears that

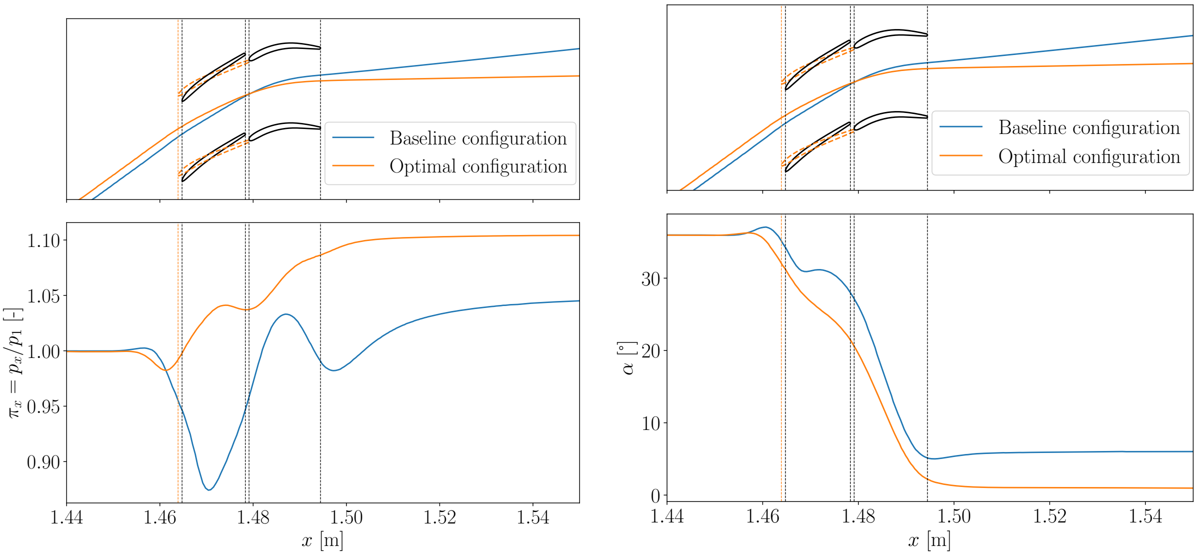

**(a)** Pressure evolution. **(b)** Flow angle evolution.

**FIGURE 5.36:** Mid rotation: evolution of flow quantities along a streamline at low inlet flow angle.

the second blade pressure side suffers from separation. Indeed, as guessed before, the flow coming from the first blade can not follow the second blade curvature. The overall tandem blade behaving as one single long blade, the general curvature should be better distributed to increase the load split and bring it closer to 0.5 (currently, LS = 0.26).

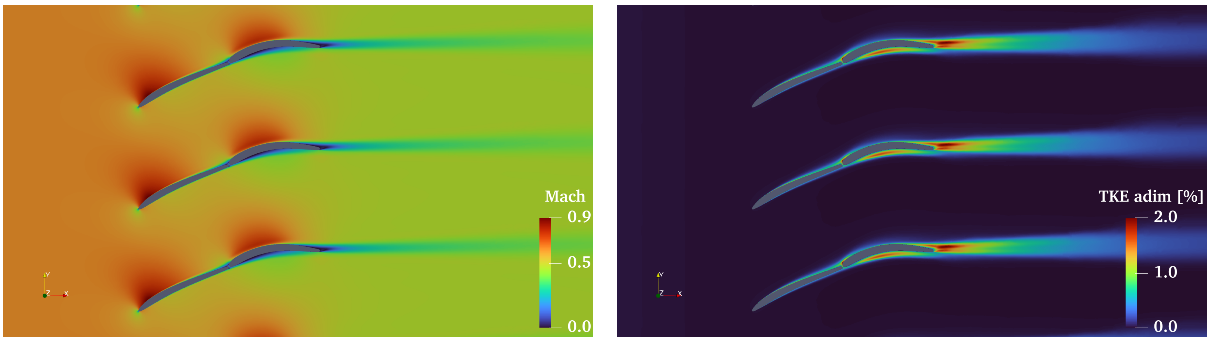

**(a)** Mach number **(b)** Turbulent kinetic energy $k$.

**FIGURE 5.37:** Mid rotation: flow visualization at low incidence.

### Blade analysis and wake

As explained before, the blade curvature being more important for the second blade, the flow can not follow this steep change of direction and detaches. As can be seen in Figure 5.38a, the first blade is less loaded towards the end while the second is highly loaded, and this unbalance is problematic. Figure 5.38b confirms the separation on the suction side of the rear blade but also towards the trailing edge on the suction side. Finally, the losses in the wake (see Figure 5.38c) are much lower as expected but also concentrated in one place as the two peaks are no longer separately visible, which make sens because the tandem behaves as one single long blade.

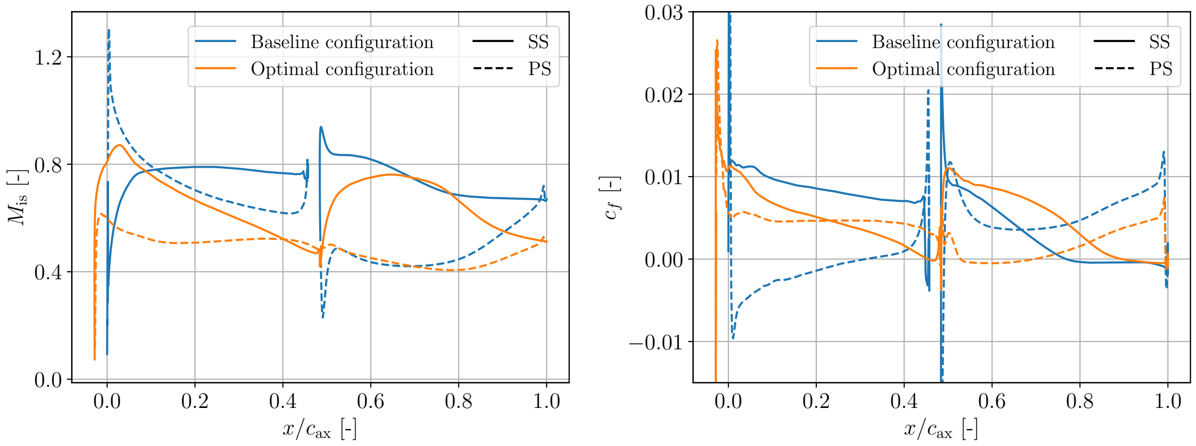

(a) Isentropic mach number. (b) Skin friction coefficient.

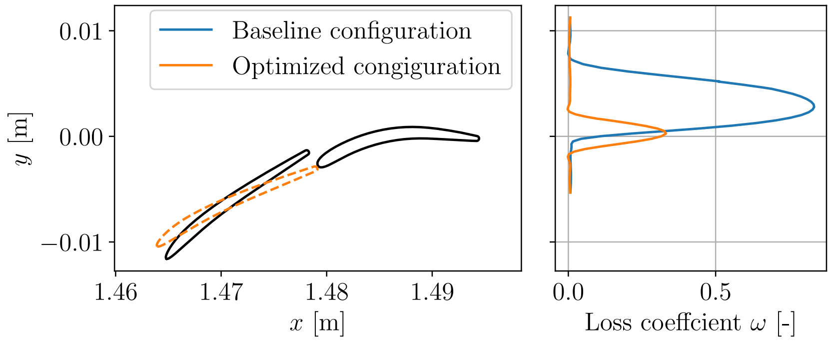

(c) Wake analysis.

**Figure 5.38:** Mid rotation: low inlet flow angle blade and wake analysis.

## 5.4 Front blade rotation around an external point

A third front blade adjusting strategy is investigated, using an external point as rotation center. The center of rotation has been positioned to create an equilateral triangle with the extremities of the front blade. This point is certainly not optimal, but it is a good starting point for optimizing strategies of the center of rotation, since it is relatively obvious and easy to find. The rotation point is represented in Figure 5.39. This center of rotation has the disadvantage of preventing almost all negative rotations. Indeed, negative rotation angles approaches the first and second blades, and eventually they will touch each other. For this reason, only high inlet flow angles will be investigated as low flow angle performances are only improved using negative rotation angles (from previous results). However, rotation angles up to $\chi_{\text{rel}} - 6°$ were used and similarly to the previous adjusting strategy, the blade gap becoming thinner, the mesh has been adapted (see Appendix 3.2, Figure A.7).

### 5.4.1 Global performances: Baseline VS optimized

The external adjusting rotation enables to reduce losses and increases the incidence angle range up to 17.0°, which is not a large increase compared to the initial range (14.7°) since the low part of the loss curve remains the same. The new reference inlet flow angle is 48.1°. The optimal rotation angle is represented in Figure 5.41.

The simulation results are represented in Figure 5.42. The red dots on the left panels still represent the theoretical configuration that minimizes the relative incidence angle $i$ absolute

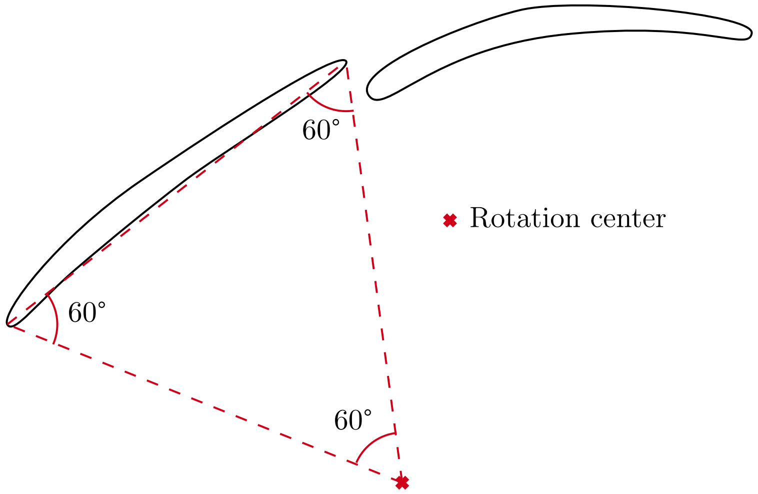

**FIGURE 5.39:** External rotation center schematic.

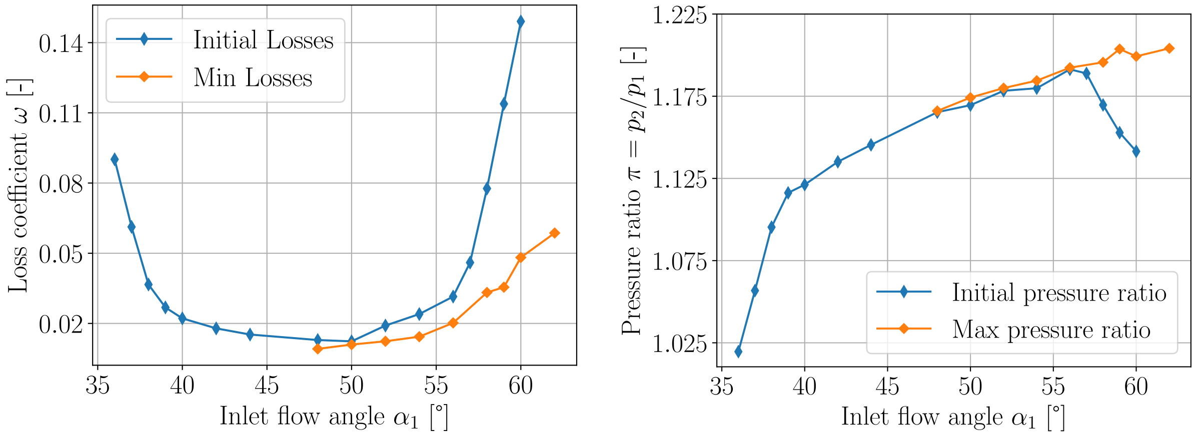

**(a)** Loss coefficient comparison.

**(b)** Pressure ratio comparison.

**FIGURE 5.40:** External rotation: performances comparison between baseline and optimized configuration.

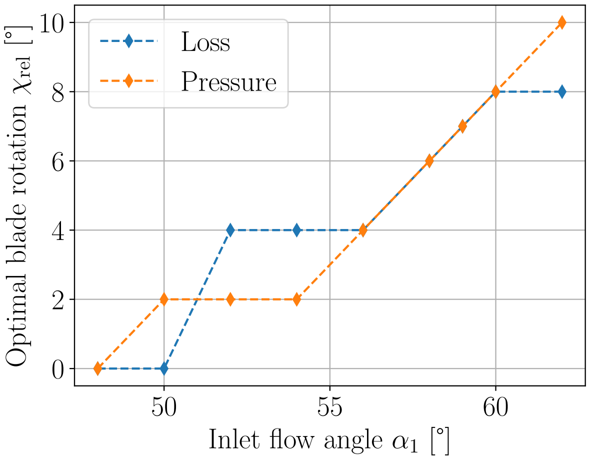

**FIGURE 5.41:** Optimal external rotation angles.

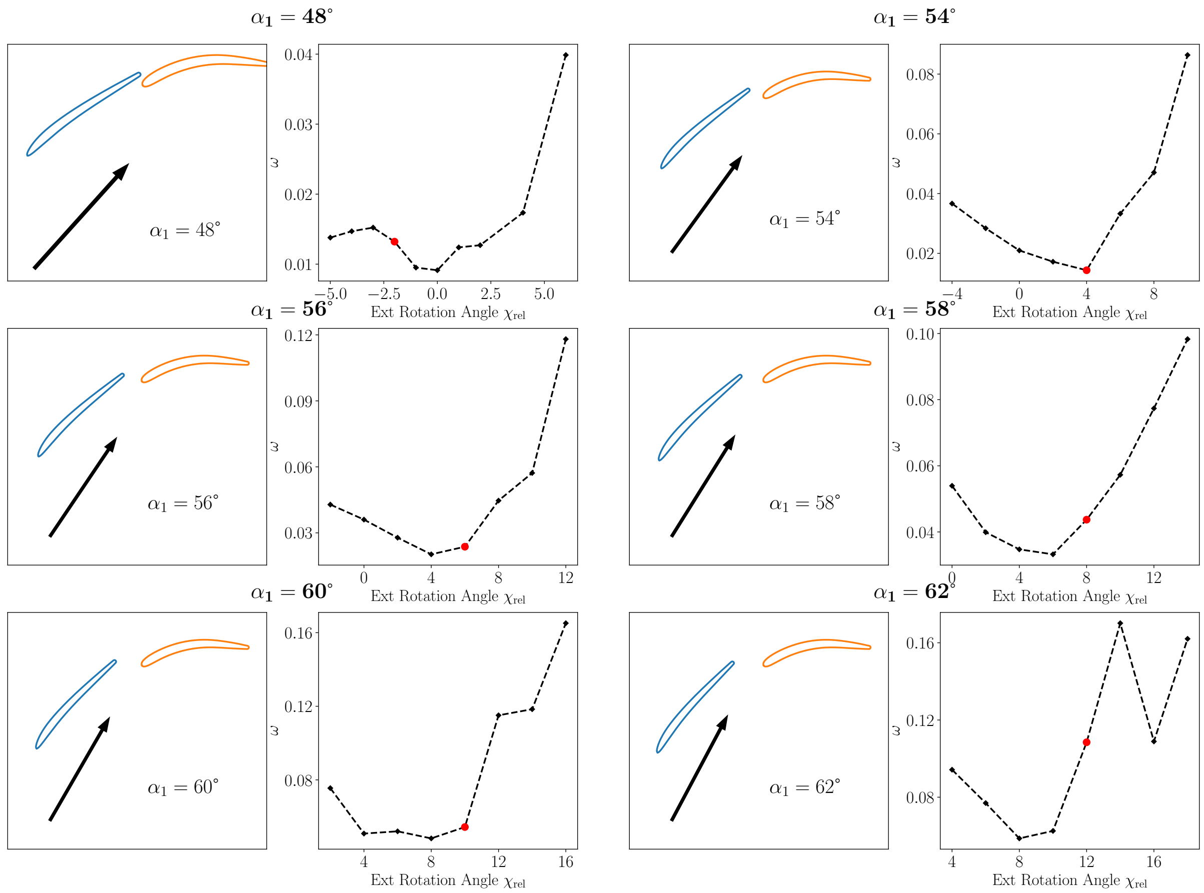

**FIGURE 5.42:** External rotation: results of losses with front blade rotation angles for different inlet flow angles.

value. Here, it seems that the case where the relative angle is minimized are more or less the optimal ones or close to the optimal. However, the simulations were made up to an inlet flow angle of 62° because higher angles induce unsteady solutions and large loss increases as can be seen for the extreme rotation angle at 62°.

Pressure and flow angle are represented along streamlines in Figure 5.43a and 5.43b. Firstly, the pressure rise is much more important on the first blade, especially on the first part. On the second blade however, the pressure reaches a maximum and then decreases a little. It is also interesting to note the initial pressure drop right before the first blade is almost the same. The flow angle evolution figure shows oscillations downstream of the blades, which could be due to unsteadiness and vortices in the wake. Moreover, the mean outlet flow angle is not zero: its value oscillates around 5°. Therefore, this adjusting configuration is not optimal and should be improved.

Table 5.4 shows the performance parameters for the external rotation strategy for $\alpha_1 = 60°$. To be noticed, the lift coefficient is significantly decreased. However, the load split is almost equal to 0.5, so the two blades approximately work the same amount on the flow.

### 5.4.2 Flow visualization

Flow visualization of Mach number and turbulent kinetic energy are represented in Figure 5.44a and 5.44b. Other flow representations are shown in Appendix A.1 in Figure A.10. As can be seen, the flow separates from the second blade and there are some highly turbulent oscillations

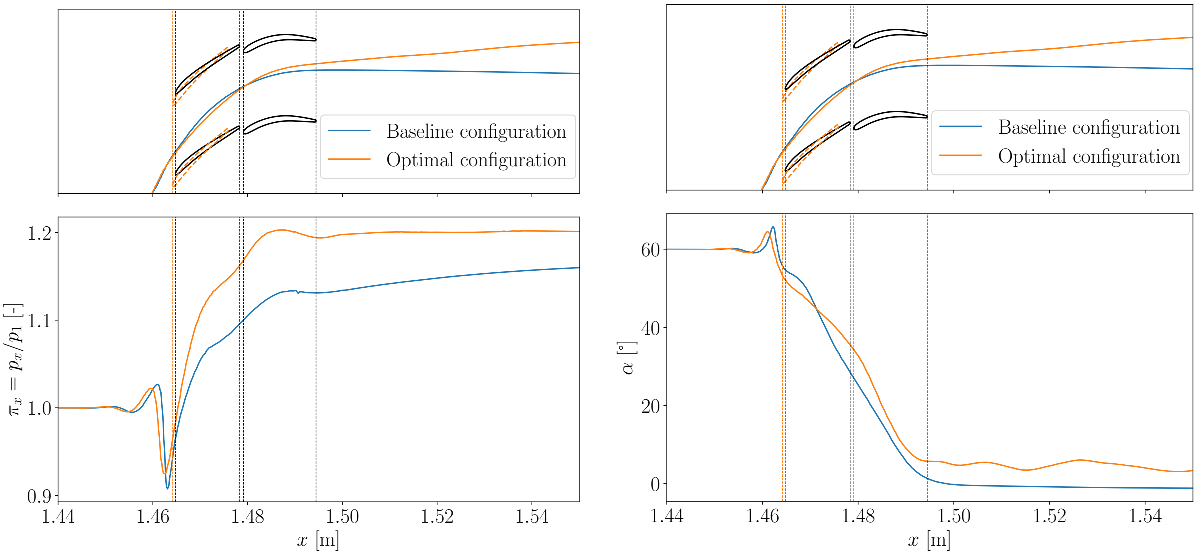

(a) Pressure evolution.

(b) Flow angle evolution.

**Figure 5.43:** External rotation: evolution of flow quantities along a streamline at high incidence.

**Table 5.4:** External rotation performance parameters.

| Inlet flow angle | $\omega$[%] | $\pi$ | DF | LS | $C_L$ | $C_D$ |
|---|---|---|---|---|---|---|
| Initial 60 | 14.91 | 1.14 | 0.69 | 0.48 | 0.93 | 0.15 |
| Optimized 60 | 4.52 | 1.20 | 0.78 | 0.53 | 0.80 | 0.04 |

in the rear blade wake. The two blade's wakes are separated and while the first one is relatively light, the second one is more severe. This phenomenon was not observed for previous adjusting strategies suggesting that, at high flow angles, the latter are preferable. However, although the results corresponding to this configuration seem consistent from the performance point of view, they need to be treated carefully since these unsteadiness lead to unsteady results which could be very different from each other depending on the solution iteration. For this reason, the external rotation strategy results at high flow angles are difficult to analyze trustfully.

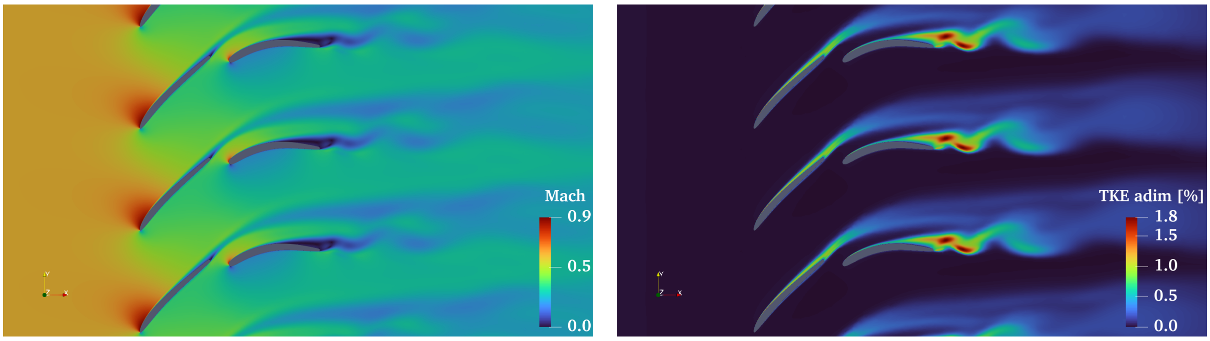

(a) Mach number.

(b) Turbulent kinetic energy $k$.

**Figure 5.44:** External rotation: flow visualization at high incidence.

### 5.4.3 Blade and wake analysis

Isentropic Mach number and skin friction coefficient around the blades are represented in Figure 5.45a and 5.45b. Isentropic mach on the first blade smoothly decreases towards the trailing edge but on the second blade, it starts to decrease and stabilizes towards the end, which is the flow separation observed previously and confirmed by the skin friction coefficient in this region. The wake is split into two part and the one due to the first blade seems harsher even though the second blade's wake contains more turbulent kinetic energy. Here again, this interpretation should be taken carefully as the properties could change rapidly.

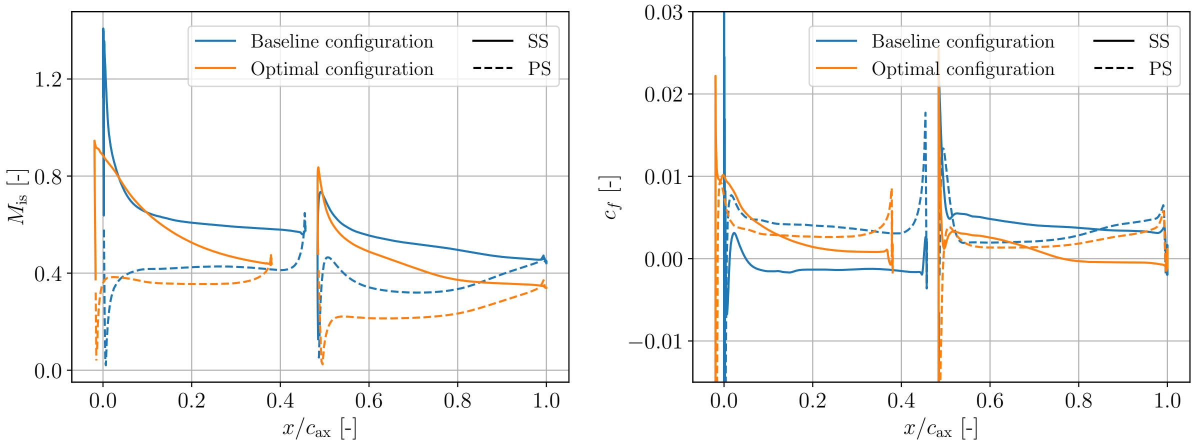

(a) Isentropic mach number.

(b) Skin friction coefficient.

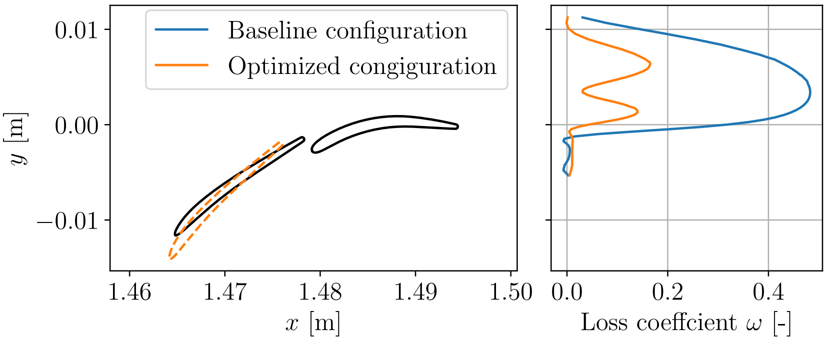

(c) Wake analysis.

**FIGURE 5.45:** External rotation: high flow angle blade and wake analysis.

## 5.5 Overall comparison

The different strategies seen previously showed several ways to combine tandem blades with a variable front blade in order to improve the stage performances. Hence, each adjusting strategy enables to increase the incidence operating range. However, a comparison between those strategies must be done to dress the pros and cons of each one of them. Hence, this section compares each strategy's optimal results. Firstly, the optimal losses are represented all together in Figure 5.46a with respect to the inlet flow angles. At low flow angles, loss performances are more or less equivalent for TE and midpoint rotation. Midpoint rotation provides rather better results at very low flow angles, while TE rotation is a little better between 35 and 45°. However, from the pressure ratio point of view, in Figure 5.46b, TE rotation is the best at low inlet flow angles. From 45°, both losses and pressure ratio of the three strategies are similar up to around 55°. Up to that point, TE and midpoint rotation are almost equivalent. However,

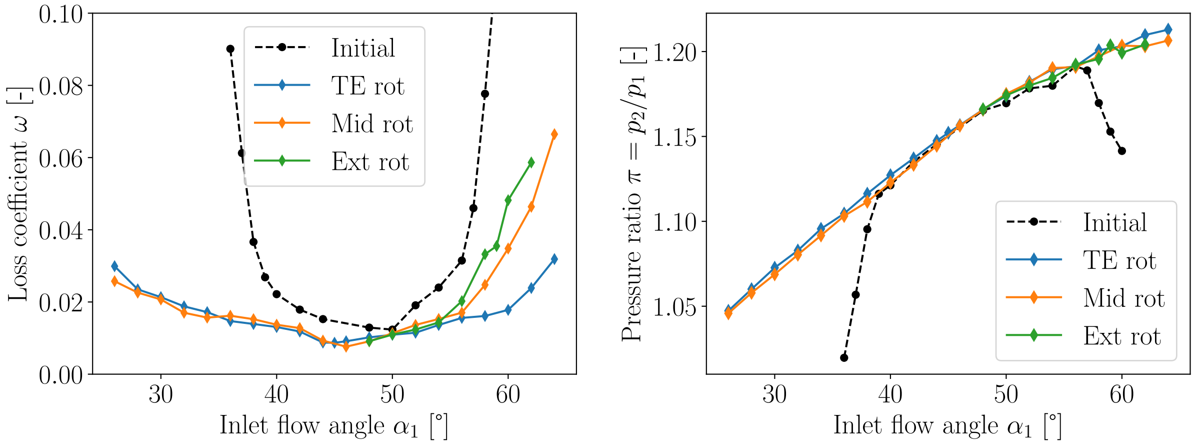

**(a)** Overall loss comparison. **(b)** Overall pressure ratio comparison.

**FIGURE 5.46:** Overall performance comparison.

at high flow angles, TE rotation offers much lower losses while midpoint and external rotation behave similarly, with still better performances for midpoint adjusting strategy. Moreover, still at high flow angles, the pressure ratio is roughly the same regardless of the strategy used. Thus, only high flow angle wake losses will be compared. Figure 5.47 shows the losses in the wakes comparison with respect to inlet flow angles. It appears that, whereas the wakes are divided into two parts for midpoint or external point rotation, the wakes of the TE rotation coming from the two blades merge into a single wake whose total magnitude is lower than the sum of the magnitudes of the wakes of the other two cases. Therefore, since the relative incidence $i$ of the three cases are more or less the same, the remaining difference is the blades relative positioning and it seems that a thinner gap generates less losses than a large one. Indeed, front blade TE rotation is the only strategy that avoid flow separation on the second blade (see Figure 5.24b, 5.34b and 5.45b).

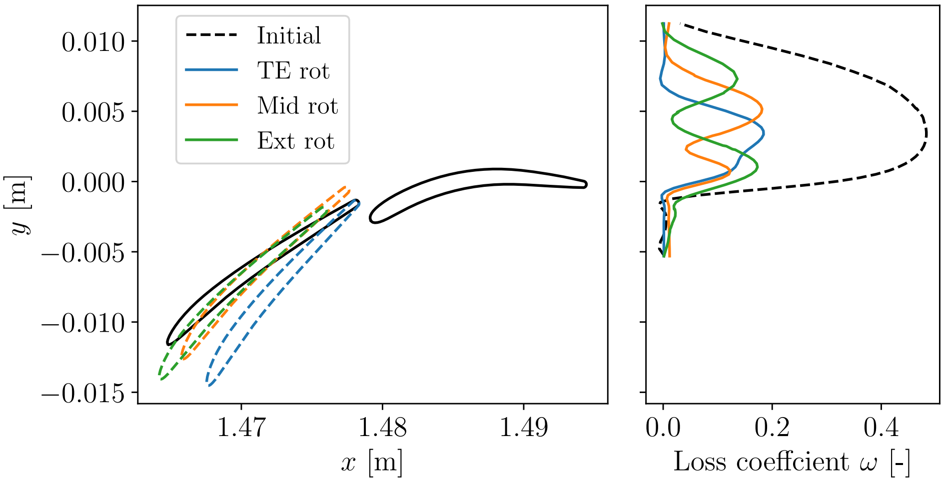

**FIGURE 5.47:** Overall wake comparison.

Table 5.5 shows the main performance parameters of the original configuration as well as those of modified configurations. TE rotation strategy offers the widest range of incidence with minimal losses. Pressure ratios are the same whatever the adjustment strategy considered, the differences being too small to be noticeable (order of $10^{-3}$). Finally, it appears that the TE rotation strategy is the best, considering the performance parameters as a whole (lift and drag coefficient, losses, diffusion factor, *etc.*). We can also see that, at high inlet flow angles, when the diffusion factor is very high, the optimal geometries behave like real tandem blades, whereas, at low flow angles and low diffusion factor, the optimal geometries are closer to a single long blade. As explained above, although the TE strategy works well, the value of a variable blade tandem is lower. This suggests, as stated by Hertel [21], that the tandem configuration is only really beneficial at high flow angles (low flow coefficient) or high diffusion factors, and this result extends to variable tandem blades.

**Table 5.5:** Overall performance comparison.

| | **Baseline** | **TE rotation** | **Mid rotation** | **Ext rotation** |
|---|---|---|---|---|
| Incidence range [°] | 14.7 | 34.2 | 30.7 | 17.4 |
| Ref. angle [°] | 46.8 | 44.9 | 42.5 | 48.3 |
| $\omega_{36}$ [%] | 9.01 | 1.47 | 1.61 | / |
| $\pi_{36}$ [-] | 1.02 | 1.10 | 1.10 | / |
| $\mathrm{DF}_{36}$ [-] | 0.24 | 0.40 | 0.39 | / |
| $\mathrm{LS}_{36}$ [-] | / | 0.45 | 0.26 | / |
| $C_{\mathrm{L},36}$ [-] | 0.18 | 0.41 | 0.33 | / |
| $C_{\mathrm{D},36}$ [-] | 0.06 | 0.01 | 0.01 | / |
| $\omega_{60}$ [%] | 14.9 | 2.09 | 3.48 | 4.52 |
| $\pi_{60}$ [-] | 1.14 | 1.20 | 1.20 | 1.20 |
| $\mathrm{DF}_{60}$ [-] | 0.69 | 0.80 | 0.79 | 0.78 |
| $\mathrm{LS}_{60}$ [-] | 0.48 | 0.58 | 0.58 | 0.53 |
| $C_{\mathrm{L},60}$ [-] | 0.93 | 0.96 | 0.91 | 0.80 |
| $C_{\mathrm{D},60}$ [-] | 0.15 | 0.02 | 0.03 | 0.04 |

# Chapter 6

# Conclusion

With a view to improve compressor performances in the current context of minimizing kerosene consumption in aircraft engines, the aim of this work was to find strategies for improving the performances of an OGV (Outlet Guide Vane), the last stator stage of an axial low pressure compressor. In particular, variations in compressor operating conditions could alter the angle of the inlet flow to the compressor stage, modifying the flow coefficient. This leads to a drop in performances, as the flow and the OGV blades are often no longer parallel, and the flow is likely to separate, causing losses of varying magnitude downstream of the stage. To this end, two different existing ideas, namely the tandem configuration and VSVs (Variable Stator Vanes), were investigated. The general idea was to combine these two technologies into a single adjusting strategy. Two guidelines were used to improve overall performances: increasing the pressure ratio while decreasing the outlet flow angle (*i.e.* increase the work coefficient), and minimizing losses in the flow wake. The technologies were studied with the aid of numerical simulations, using the RANS model on the CDF SU2 open-source software. This enabled a large number of different geometries to be studied, and a series of parameters to be varied with a view to obtain the best possible geometries.

Firstly, the basic tandem configuration without variable front blade was studied to understand its limitations and see what improvement it already provided when used alone. The initial tandem configuration gave good performances at medium flow angles, particularly around 47°. However, losses and pressure ratio deteriorated rapidly as the flow angle moved away from this reference angle, mainly due to high flow separation regions along the blades, which produced a severe wake region downstream. In addition, the downstream flow angle was not zero. This situation is not optimal, as part of the flow's transverse kinetic energy was not transferred to static pressure. For these reasons, the range of angles of incidence was quite small, only around 15°. Beyond this limit, losses doubled compared with the minimum loss.

In a second step, by combining the tandem blade concept with an other already existing concept in the industry, variable stator vanes (VSVs), a series of numerical simulations were carried out to determine the extent to which this could increase the range of incidence angles of the flow arriving at the compressor stage. Three strategies for adjusting the angle of the tandem's front blade were studied separately, and then compared to each other. In all three cases, the tandem's front blade was rotated: once around the trailing edge, once around the midpoint of the mean chord and once around a point outside the blade. The results showed remarkable improvements for all three strategies, reducing wakes wideness and magnitude and avoiding separation in some cases. However, since the third strategy did not allow good matching rotations at low inlet flow angles, only high flow angle performances were simulated for this strategy. Nevertheless, it was shown that the incidence range, which was initially 14.7° with no change to the tandem geometry, expanded to 34.2°, 30.7° and 17.4° for the first, second and third strategy respectively.

Moreover, it enables to increase significantly the pressure ratios over the stage for every off-range incidences. However, the TE rotation performs slightly better, particularly at high flow angles. Since high inlet flow angles are the most interesting from an industrial application point of view as they results in higher pressure rises and approach surge conditions, the first strategy is selected as the best performer. However, given the difficulty of manufacturing a variable-geometry system whose axis would pass through the TE of the blade, a compromise could be found by using a strategy halfway between the first and second, *i.e.* whose point of rotation would be halfway between the TE and the midpoint of the mean chord even if further investigation should be done to measure properly the torque and force evolution along the span. Moreover, the results also suggest that the value of a tandem blade variable is much lower at low flow angles (high flow coefficients). In this case, simulations of rotation around the midpoint show results that are just as good, if not better, when the two blades are aligned and form a single blade set at a leading edge angle of 38°. In conclusion, variable tandem blades are highly efficient and open up the operating range significantly, especially for operating conditions that would lead to high flow angles.

## 6.1 Perspectives and future developments

It would be interesting to try to optimize the location of the trade-off rotation point, to see which would satisfy the performance criteria while allowing a feasible adjustment system. In addition to this, URANS simulations could be of interest in understanding extreme flow angles phenomena. Indeed, as the present work was limited to results simulated in RANS, the appearance of non-stationary phenomena in the solutions limited confidence in these results, which were therefore restricted to stationary cases. In addition to this, it would be interesting to investigate more precisely the limits of the incidence ranges found in the present report in LES (large eddy simulations) to verify their performances. In fact, when it comes to the appearance of complex phenomena in the flow, the RANS model has its limitations, and we have no guarantee that it correctly represents the physics of the flow. It would therefore be beneficial to use more accurate models (LES) in regions of the incidence range where losses start to increase significantly.

Secondly, although the results showed poorer performances for the third strategy, an optimization of rotation point selection could also be of interest. Indeed, in the present study, the choice of the external rotation point is based on the fact that it is one of the most obvious, but there is no particular aerodynamic or mechanical reason for this, and it is likely that a different rotation point could generate much better results. This optimization should be based on several parameters such as blade stagger angles, inlet flow angles, integrated losses, static pressure ratio and rotation blade center location.

Next, a variation of the blades' own geometry would be interesting. For example, a comparison of the same adjustment strategy for several front-blade geometries might be useful to determine whether it is possible to increase the incidence range a little further. A more curved front blade could indeed enable better compression ratios, but could also lead to more losses. On the other hand, a less curved second blade may be beneficial for low inlet flow angle to prevent flow separation on its suction side while allowing a better load split between the two blades. In addition to these points, it would also be interesting to study the influence of boundary conditions on performance. In the present case, the input Mach number was constant and fixed at 0.6 with a Reynolds number of $6.5 \times 10^5$. However, in real-life conditions, an axial compressor may be subject to variations in inlet flow speeds, for example during the start-up phase, and may also be forced to operate outside optimum conditions, at lower or higher speeds, so it would be useful to understand how performances vary with these changes.

Finally, it would be interesting to study the 3D effects occurring in the fluid when the OGV is considered as a whole blade, interacting with the engine shaft and casing. The results presented in this report are assumed to be correct only in a region of the blade far from the tips, and it is impossible to extend them to the entire blade.

# Appendix A

# Appendix

## A.1 Baseline configuration

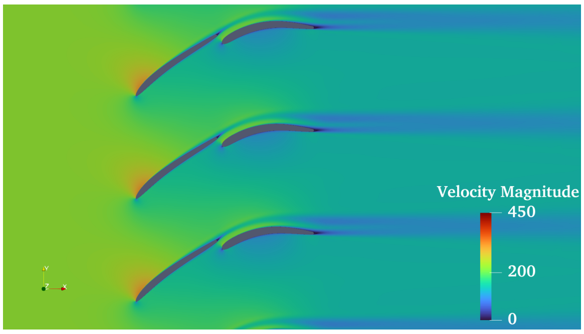

**(a)** $\alpha_1 = 50°$, $i = 0°$.

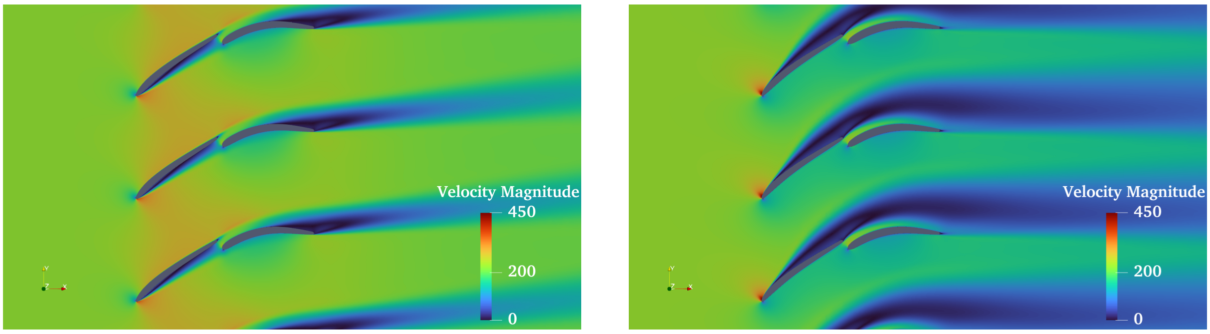

**(b)** $\alpha_1 = 36°$, $i = -14°$.

**(c)** $\alpha = 60°$, $i = 10°$.

**Figure A.1:** Velocity comparison for inlet flow angle of 36, 50 and 60 degrees, with baseline configuration.

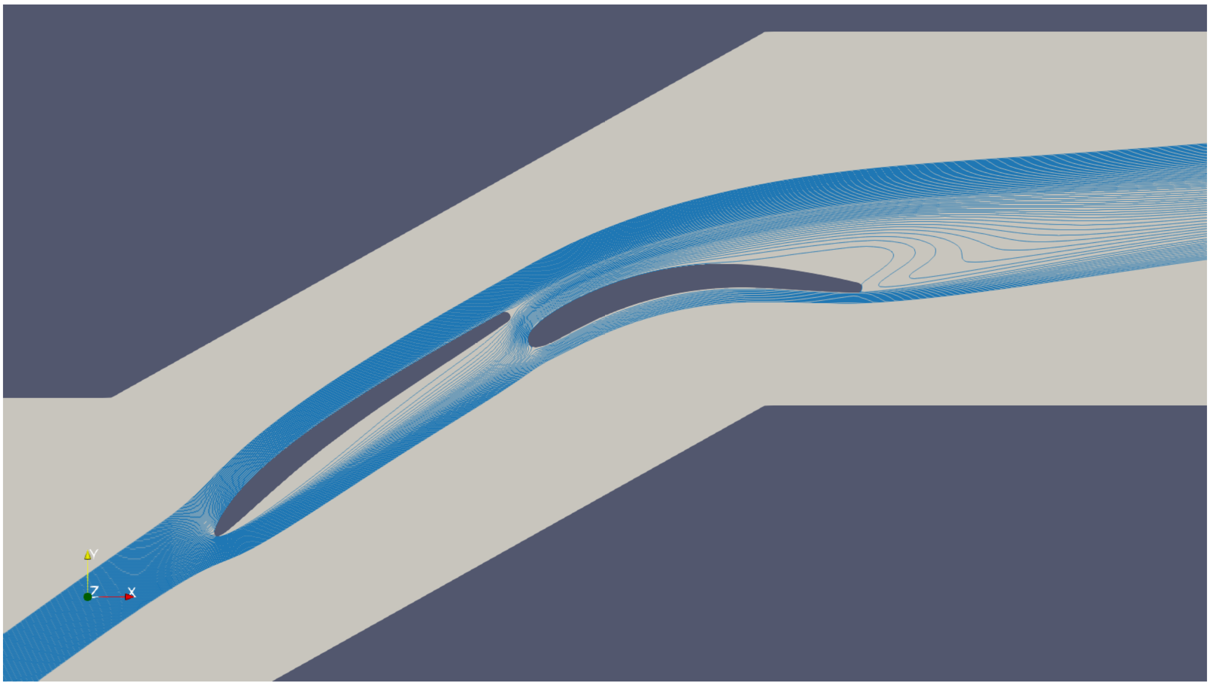

**FIGURE A.2:** Flow separation, for initial configuration for $\alpha_1 = 36°$.

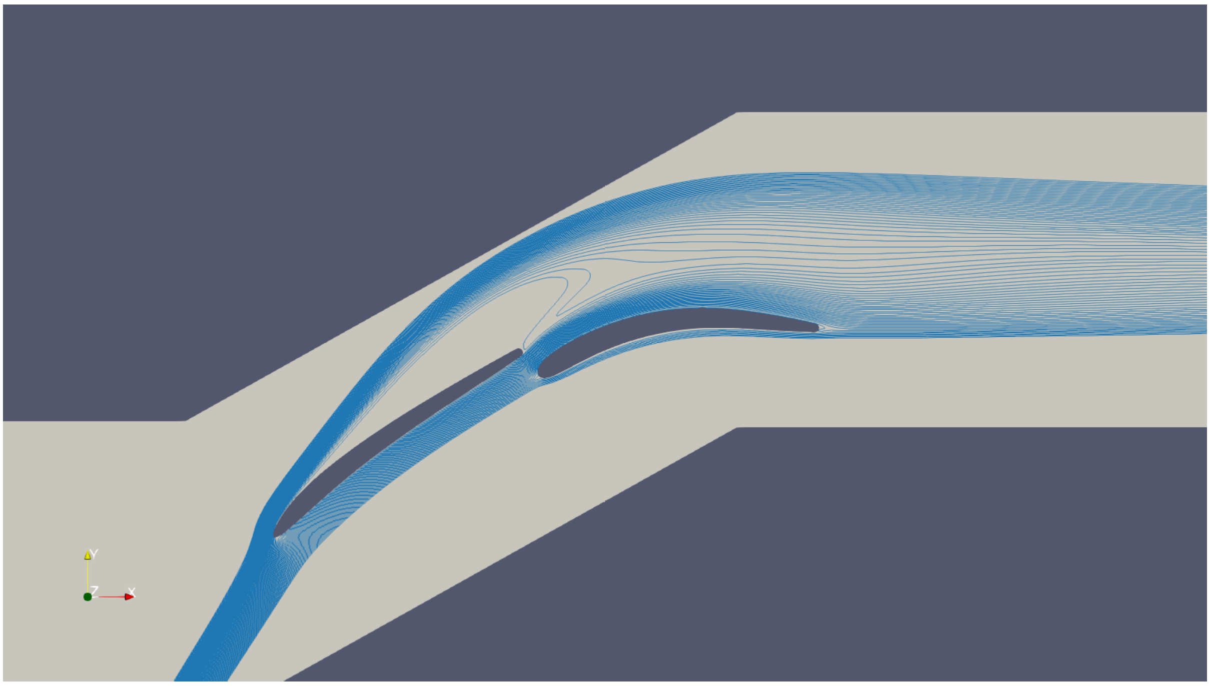

**FIGURE A.3:** Flow separation, for initial configuration for $\alpha_1 = 60°$.

## A.2 Turbulence model modifications

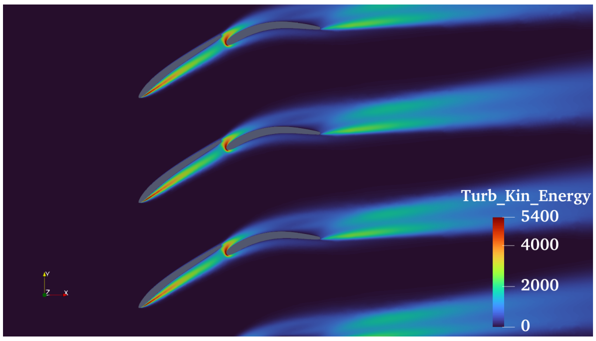

**(a)** Initial case: $\mathcal{P} = 2\nu_T|S|^2$.

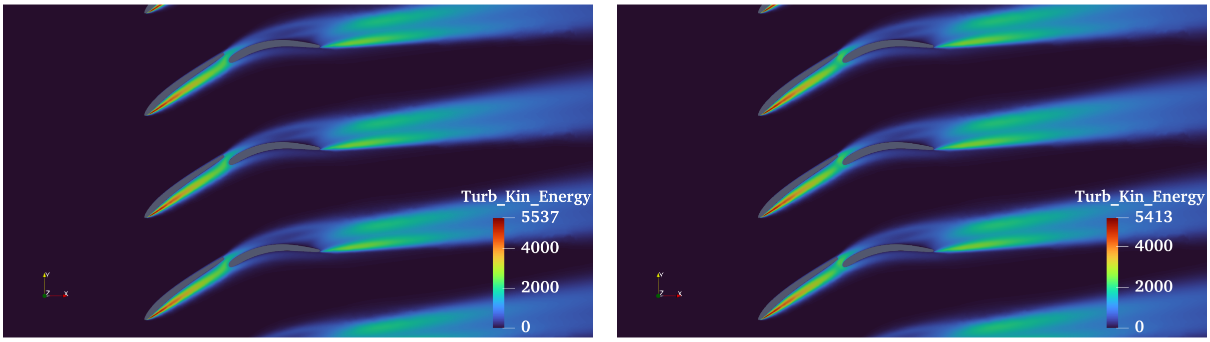

**(b)** $\mathcal{P} = 2\nu_T|\Omega|^2$.

**(c)** $\mathcal{P} = 2\nu_T|S||\Omega|$.

**FIGURE A.4:** SST production modifications.

## A.3 Turbulence decay

This section studies the decay of turbulent energy at the entrance to the domain. For simulations using SU2, the intensity level of the turbulent kinetic energy

$$I = \sqrt{\frac{2}{3}}\frac{\sqrt{k}}{u} \tag{A.1}$$

is fixed, and its default value, used for all simulations, is 5%. However, when we look at the evolution of this intensity over the flow, as shown in Figure A.6 and A.5, we see a rapid decrease in intensity down to a value well below that of the inlet at the blades. This can be explained by the fact that no turbulent kinetic energy is produced in this region, and only the destruction terms are active. In fact, production is approximated by

$$\mathcal{P} = 2\nu_T|S|^2, \tag{A.2}$$

with $S_{ij} = (\partial_i U_j + \partial_j U_i)$. However, in the region upstream of the blades, the $S$ term is zero, as there are no straining in the flow. In this way, only dissipation is active, and turbulent energy is quickly decreasing. In fact, following Spalart et al. [48], the equation for the evolution of $k$ takes the following form

$$k = k_{\text{in}}\left[1 + (C_{\varepsilon 2} - 1)\left(\frac{\varepsilon}{k}\right)_{\text{in}}\frac{x}{U}\right]^{\frac{-1}{C_{\varepsilon 2}-1}}, \tag{A.3}$$

with $C_{\varepsilon 2} = 1.92$. Hence, $k$ decreases to the power -1.1 with $x$. A solution has been developed by Spalart et al. [48], consisting in adding a sustaining term to prevent the $k$ (and the other turbulent quantities) to drop below a minimal value - *floor values*. This option is available in SU2 (`SST_OPTIONS=SUSTAINING`) but was not used in this work since this modification may introduce non-convergence. Moreover, this turbulent decay is not a dramatic issue in the scope of this work since the turbulent quantities at the blade leading edge were not specified. However, it could be an interesting future study to investigate the influence of the turbulent level on the performances of the tandem.

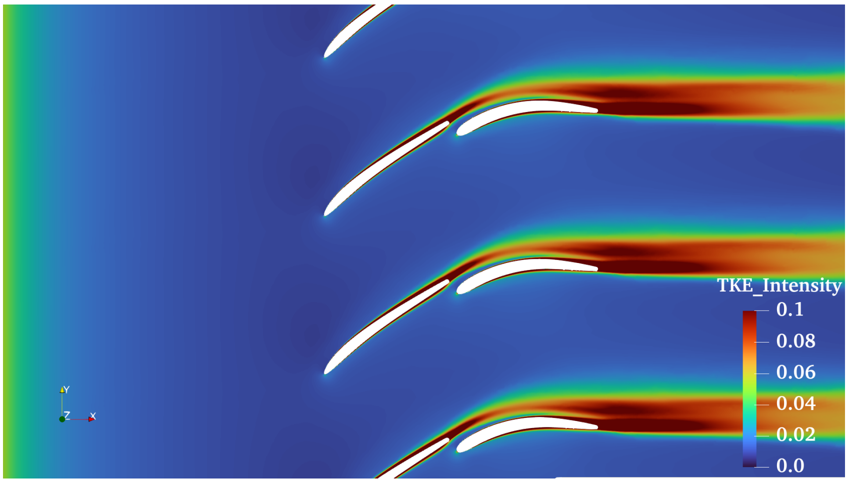

**FIGURE A.5:** TKE intensity over the domain.

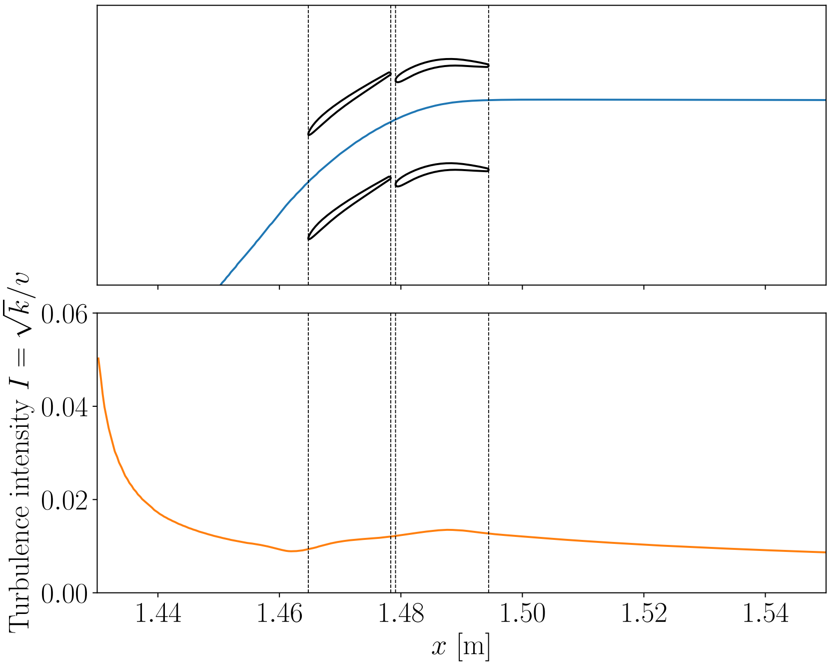

**FIGURE A.6:** TKE intensity decay along a streamline.

## A.4 Rotation around the chord mid-point

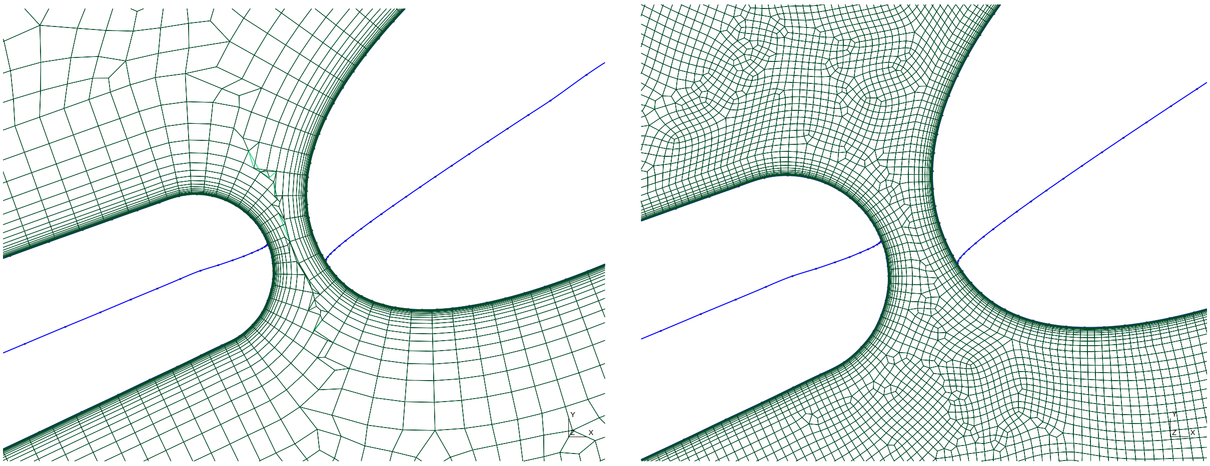

(a) Bad gap refinement mesh. (b) Best gap refinement mesh.

**Figure A.7:** Mid rotation gap refinement process.

### A.4.1 High incidence

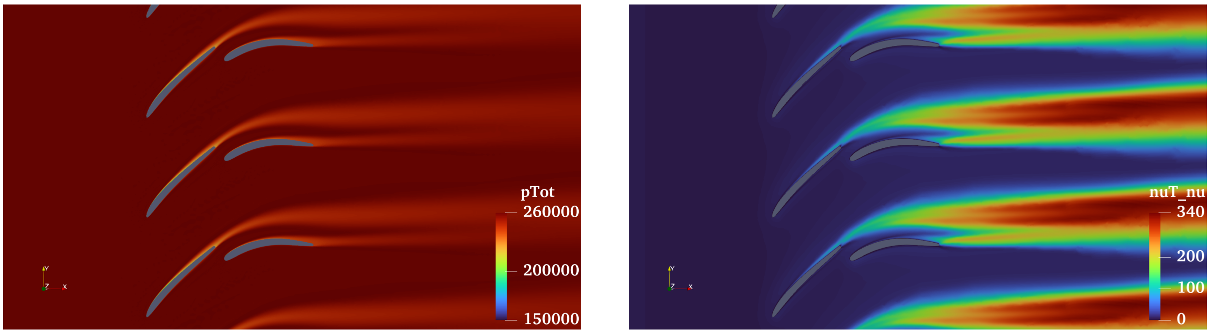

(a) Total pressure. (b) $\nu_T/\nu$.

**Figure A.8:** Midpoint rotation: Flow representation at high incidence angle (60°).

### A.4.2 Low incidence

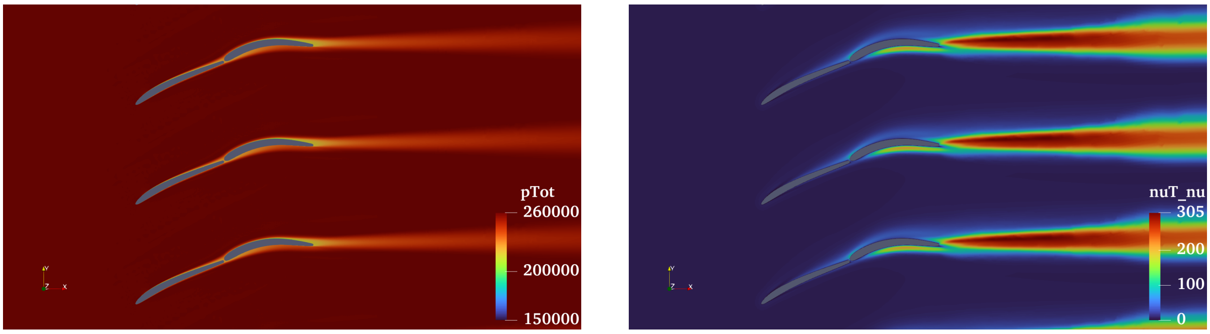

(a) Total pressure. (b) $\nu_T/\nu$.

**Figure A.9:** Midpoint rotation: Flow representation at low incidence angle (36°).

## A.5 External rotation

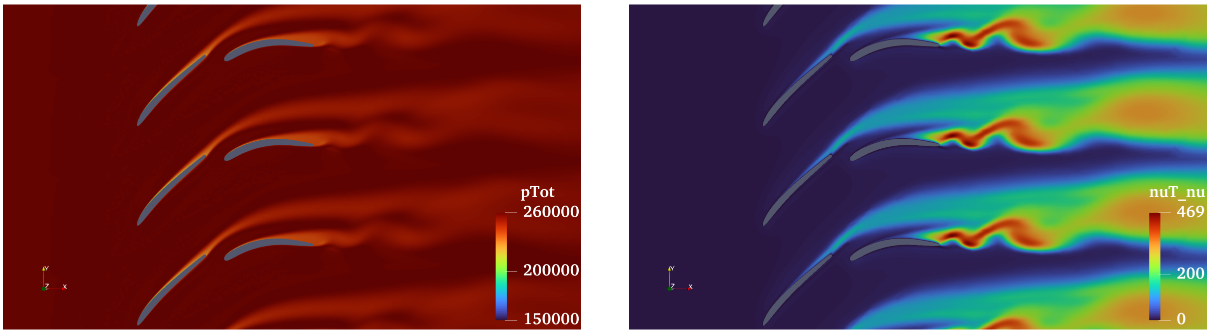

**(a)** Total pressure. **(b)** $\nu_T/\nu$.

**Figure A.10:** External rotation: Flow representation at high incidence angle (60°).

# Bibliography

[1] Carlos Pérez Arroyo et al. "Towards the Large-Eddy Simulation of a full engine: Integration of a 360 azimuthal degrees fan, compressor and combustion chamber. Part I: Methodology and initialisation". In: *Journal of the Global Power and Propulsion Society* (May 2021), pp. 1–16. DOI: 10.33737/jgpps/133115. (Visited on 06/02/2024).

[2] Multitel. *WINGS - Technology Innovation Partnership - Aeronautics*. Multitel. URL: https://www.multitel.eu/projects/wings/ (visited on 06/03/2024).

[3] Pratt & Whitney. *Home*. Pratt & Whitney, 2024. URL: https://www.prattwhitney.com/ (visited on 06/01/2024).

[4] Koen Hillewaert. *Aerospace Propulsion* [Course Lecture]. Univertité de Liège, May 2023.

[5] Chung-Hua Wu. *A General Theory of Three-dimensional Flow in Subsonic and Supersonic Turbomachines of Axial-, Radial-, and Mixed-flow Types*. NASA, 1952.

[6] S. Lieblein. *Diffusion factor for estimating losses and limiting blade loadings in axial-flow compressor blade elements*. NACA, June 1953.

[7] Lewis Research Center. *Aerodynamic Design of Axial-flow Compressors*. NASA, 1965.

[8] N A Cumpsty. *Compressor Aerodynamics*. Longman Scientific and Technical, 1989.

[9] S L Dixon and C A Hall. *Fluid mechanics and thermodynamics of turbomachinery*. 7th ed. Butterworth-Heinemann, 2014.

[10] Jérôme Sans. *The Effect of Solidity on Compressor Performance and Stability*. von Karman Insitute for Fluid Dynamics, 2012.

[11] C Reid. "The Response of Axial Flow Compressors to Intake Flow Distortion". In: *Turbo Expo: Turbomachinery Technical Conference and Exposition* (Mar. 1969). DOI: 10.1115/69-gt-29. (Visited on 02/29/2024).

[12] N Sitaram and B. Lakshminarayana. "End wall flow characteristics and overall performance of an axial flow compressor stage". In: *NASA (National Aeronautics and Space Administration)* (Feb. 1983). (Visited on 05/26/2024).

[13] Yingjie Zhang et al. "Flow control of hub corner stall in a highly loaded axial compressor cascade". In: *International Journal of Heat and Fluid Flow* 78 (Aug. 2019), p. 108434. DOI: 10.1016/j.ijheatfluidflow.2019.108434. (Visited on 05/07/2024).

[14] Minsuk Choi et al. "Role of Hub-Corner-Separation on Rotating Stall in an Axial Compressor". In: *Transactions of the Japan Society for Aeronautical and Space Sciences* 51 (2008), pp. 93–100. DOI: 10.2322/tjsass.51.93. (Visited on 05/09/2024).

[15] M. Hewkin-Smith et al. "The Role of Tip Leakage Flow in Spike-Type Rotating Stall Inception". In: *Journal of Turbomachinery* 141 (Feb. 2019). DOI: 10.1115/1.4042250. (Visited on 05/09/2024).

[16] John D Denton. "Loss Mechanisms in Turbomachines". In: *Turbo Expo: Turbomachinery Technical Conference and Exposition* (May 1993). DOI: 10.1115/93-gt-435.

[17] Baojie Liu et al. “Using tandem blades to break loading limit of highly loaded axial compressors”. In: *Chinese Journal of Aeronautics* 35 (Apr. 2022), pp. 165–175. DOI: 10.1016/j.cja.2021.07.031. (Visited on 03/24/2024).

[18] Zonghao Yang et al. “Numerical Investigation of Inlet Boundary Layer in an Axial Compressor Tandem Cascade”. In: *Energies* 15 (Sept. 2022), pp. 6850–6850. DOI: 10.3390/en15186850. (Visited on 02/14/2024).

[19] U.K. Saha and B. Roy. “Experimental investigations on tandem compressor cascade performance at low speeds”. In: *Experimental Thermal and Fluid Science* 14 (Apr. 1997), pp. 263–276. DOI: 10.1016/s0894-1777(96)00125-2. (Visited on 03/25/2024).

[20] Christoph Schluer and Martin Böhle. *Numerical Investigation of the Secondary Flows and Losses in a High-Turning Tandem Compressor Cascade*. 2009. (Visited on 02/12/2024).

[21] Charlotte Hertel et al. “Investigations on Aerodynamic Loading Limits of Subsonic Compressor Tandem Cascades: End Wall Flow”. In: *Turbo Expo: Turbomachinery Technical Conference and Exposition* (June 2014). DOI: 10.1115/gt2014-26978. (Visited on 03/25/2024).

[22] J Sun and R L Elder. “Numerical optimization of a stator vane setting in multistage axial-flow compressors”. In: *Proceedings of the Institution of Mechanical Engineers. Part A, Journal of power and energy* 212 (June 1998), pp. 247–259. DOI: 10.1243/0957650981536772. (Visited on 04/13/2024).

[23] H Roh and Stephen Daley. “The online optimisation of stator vane settings in multi-stage axial compressors”. In: *International Journal of Advanced Mechatronic Systems* 1 (June 2009), pp. 266–266. DOI: 10.1504/ijamechs.2009.026332. (Visited on 04/28/2024).

[24] Jinguang Yang et al. “Stator re-stagger optimization in multistage axial compressor”. In: *Propulsion and Power Research* 10 (June 2021), pp. 107–117. DOI: 10.1016/j.jppr.2021.03.002. URL: https://www.sciencedirect.com/science/article/pii/S2212540X21000195 (visited on 04/17/2024).

[25] Fulei Chu and Zhaoye Qin. *Proceedings of the 11th IFToMM International Conference on Rotordynamics*. Vol. 2. Springer Nature, Sept. 2023, pp. 452–463.

[26] Christopher D. Jones, Robert C. Backhouse, and Adam J. Bishop. *Variable Stator Vane And Method Of Fabricating Variable Stator Vane*. Ed. by Rolls-Royce plc. Sept. 2020.

[27] Peter Alan Davidson. *Turbulence : an introduction for scientists and engineers*. Oxford University Press, 2015.

[28] P A Durbin and A Pettersson. *Statistical Theory and Modeling for Turbulent Flows*. John Wiley & Sons, June 2011.

[29] Vincent Terrapon. *Turbulent Flows* [Course lecture]. Université de Liège, 2023.

[30] David C Wilcox. *Turbulence Modeling for CFD*. 3rd ed. DCW Industries, Inc., 2006.

[31] F. R. Menter. “Two-equation eddy-viscosity turbulence models for engineering applications”. In: *AIAA Journal* 32 (Aug. 1994), pp. 1598–1605. DOI: 10.2514/3.12149.

[32] Hermann Schlichting and Klaus Gersten. *Boundary-Layer Theory*. Springer Berlin Heidelberg, 2017. DOI: 10.1007/978-3-662-52919-5.

[33] Vincent Terrapon. *Introduction to Boundary Layer Theory* [Course lecture]. Université de Liège, Feb. 2012.

[34] Cenaero. *Supercalculateur Lucia | Opérateur du supercalculateur Tier-1 de Wallonie*. tier1.cenaero.be, 2024. URL: https://tier1.cenaero.be/fr/LuciaInfrastructure (visited on 03/18/2024).

[35] AK6. *Lucia, the new infrastructure for HPC*. A6K, Nov. 2022. URL: https://www.a6k.be/whats-up/lucia-the-new-infrastructure-for-hpc (visited on 05/11/2024).

[36] CÉCI. *CECI.* www.ceci-hpc.be. URL: `https://www.ceci-hpc.be/` (visited on 05/11/2024).

[37] Schedmd. *Slurm Workload Manager - Overview.* slurm.schedmd.com. URL: `https://slurm.schedmd.com/overview.html`.

[38] SU2 | Multiphysics Simulation and Design Software. *SU2, Multiphysics Simulation and Design Software.* su2code.github.io, 2024. URL: `https://su2code.github.io/docs_v7/home/` (visited on 03/22/2024).

[39] Thomas D. Economon et al. "SU2: An Open-Source Suite for Multiphysics Simulation and Design". In: *AIAA Journal* 54 (Mar. 2016), pp. 828–846. DOI: `10.2514/1.j053813`. URL: `http://web.mit.edu/su2_v6.0/1.Ej053813.pdf`.

[40] Kitware Inc. *ParaView.* Paraview.org, 2018. URL: `https://www.paraview.org/`.

[41] Vincent Terrapon. *Computational fluid dynamics* [Course lecture]. Université de Liège, 2023.

[42] Antony Jameson. "Origins and Further Development of the Jameson–Schmidt–Turkel Scheme". In: *AIAA Journal* 55 (May 2017), pp. 1487–1510. DOI: `10.2514/1.j055493`. (Visited on 04/16/2024).

[43] Sup Galilée. *Equations non linéaires* [Course lecture]. 2018. (Visited on 04/12/2024).

[44] Christophe Geuzaine and Jean-François Remacle. "Gmsh: A 3-D finite element mesh generator with built-in pre- and post-processing facilities". In: *International Journal for Numerical Methods in Engineering* 79 (May 2009), pp. 1309–1331. DOI: `10.1002/nme.2579`.

[45] Ansys Inc. *TGrid 5.0 User's Guide.* Ansys Inc., Apr. 2008, pp. 15.1–15.18.

[46] Paul A Durbin. "On the k-3 stagnation point anomaly". In: *International Journal of Heat and Fluid Flow* 17 (Feb. 1996), pp. 89–90. DOI: `10.1016/0142-727x(95)00073-y`. (Visited on 04/26/2024).

[47] Kato M and Launder B E. *The modelling of turbulent flow around stationary and vibrating square cylinders.* Jan. 1993, pp. 1–10. (Visited on 05/27/2024).

[48] Philippe R Spalart and Christopher L Rumsey. "Effective Inflow Conditions for Turbulence Models in Aerodynamic Calculations". In: *AIAA Journal* 45 (Jan. 2007), pp. 2544–2553. DOI: `10.2514/1.29373`. (Visited on 04/21/2024).

[49] Alexander Heinrich and Dieter Peitsch. *3D Numerical and Experimental Investigation of High Turning Compressor Tandem Cascade.* 2016. (Visited on 02/10/2024).

[50] Charles Hirsch. *Numerical computation of internal and external flows. Volume 1, Fundamentals of computational fluid dynamics.* Second Edition. Vol. 1. Butterworth-Heinemann, 2007.

[51] Mohamed Mohsen, Farouk M Owis, and Ali A Hashim. "The impact of tandem rotor blades on the performance of transonic axial compressors". In: *Aerospace Science and Technology* 67 (Aug. 2017), pp. 237–248. DOI: `10.1016/j.ast.2017.04.019`. (Visited on 03/25/2024).

[52] Tim Schneider and Dragan Kožulović. "Flow Characteristics of Axial Compressor Tandem Cascades at Large Off-Design Incidence Angles". In: (June 2013). DOI: `10.1115/gt2013-94708`. (Visited on 03/25/2024).

[53] N L Sanger. "Analytical study of the effects of geometric changes on the flow characteristics of tandem- bladed compressor stators". In: *Nasa Technical Note* (Mar. 1971). (Visited on 03/25/2024).

[54] Zhaoyun Song and Bo Liu. "Optimization design for tandem cascades of compressors based on adaptive particle swarm optimization". In: *Engineering Applications of Computational Fluid Mechanics* 12 (Jan. 2018), pp. 535–552. DOI: `10.1080/19942060.2018.1474806`. (Visited on 03/29/2024).

[55] Xiaochen Mao et al. “Influence of Gap Shape on Flow Characteristics of Highly Loaded Compressor Tandem Cascades”. In: *Journal of engineering for gas turbines and power* (Mar. 2024), pp. 1–25. DOI: `10.1115/1.4065019`. (Visited on 03/29/2024).

[56] Yuan Tao, Xianjun Yu, and Baojie Liu. “A New Method for Rapid Optimization Design of a Subsonic Tandem Blade”. In: *Applied sciences* 10 (Dec. 2020), pp. 8802–8802. DOI: `10.3390/app10248802`. (Visited on 03/29/2024).

[57] Jonathan McGlumphy et al. “Numerical Investigation of Tandem Airfoils for Subsonic Axial-Flow Compressor Blades”. In: *Journal of Turbomachinery* 131 (Feb. 2009). DOI: `10.1115/1.2952366`. (Visited on 03/29/2024).

[58] J E Crouse and Mc Nally. *FORTRAN program for computing coordinates of circular arc single and tandem turbomachinery blade sections on a plane.* Nov. 1970. (Visited on 03/29/2024).

[59] John D Anderson. *Fundamentals of Aerodynamics.* 6th ed. McGraw Hill Education, 2017.

[60] Zhitao Wang et al. “The Off-Design Performance Simulation of Marine Gas Turbine Based on Optimum Scheduling of Variable Stator Vanes”. In: *Mathematical problems in engineering* 2017 (Jan. 2017), pp. 1–11. DOI: `10.1155/2017/2671251`. (Visited on 04/13/2024).